

Metabolic Fluxes in an Illuminated *Arabidopsis* Rosette

Marek Szecowka, Robert Heise, Takayuki Tohge, Adriano Nunes-Nesi, Daniel Vosloh, Jan Huege, Regina Feil, John Lunn, Zoran Nikoloski, Mark Stitt, Alisdair R. Fernie and Stéphanie Arrivault
Plant Cell 2013;25;694-714; originally published online February 26, 2013;
DOI 10.1105/tpc.112.106989

This information is current as of October 15, 2013

Supplemental Data	http://www.plantcell.org/content/suppl/2013/02/20/tpc.112.106989.DC1.html
References	This article cites 98 articles, 32 of which can be accessed free at: http://www.plantcell.org/content/25/2/694.full.html#ref-list-1
Permissions	https://www.copyright.com/ccc/openurl.do?sid=pd_hw1532298X&issn=1532298X&WT.mc_id=pd_hw1532298X
eTOCs	Sign up for eTOCs at: http://www.plantcell.org/cgi/alerts/ctmain
CiteTrack Alerts	Sign up for CiteTrack Alerts at: http://www.plantcell.org/cgi/alerts/ctmain
Subscription Information	Subscription Information for <i>The Plant Cell</i> and <i>Plant Physiology</i> is available at: http://www.aspb.org/publications/subscriptions.cfm

Metabolic Fluxes in an Illuminated *Arabidopsis* Rosette

Marek Szecowka,^{a,1} Robert Heise,^{b,1} Takayuki Tohge,^a Adriano Nunes-Nesi,^a Daniel Vosloh,^c Jan Huege,^{a,2} Regina Feil,^c John Lunn,^c Zoran Nikoloski,^b Mark Stitt,^c Alisdair R. Fernie,^{a,3} and Stéphanie Arrivault^c

^aCentral Metabolism Research Group, Max-Planck-Institute of Molecular Plant Physiology, 14476 Potsdam-Golm, Germany

^bSystems Biology and Mathematical Modeling Research Group, Max-Planck-Institute of Molecular Plant Physiology, 14476 Potsdam-Golm, Germany

^cMetabolic Systems Research Group, Max-Planck-Institute of Molecular Plant Physiology, 14476 Potsdam-Golm, Germany

Photosynthesis is the basis for life, and its optimization is a key biotechnological aim given the problems of population explosion and environmental deterioration. We describe a method to resolve intracellular fluxes in intact *Arabidopsis thaliana* rosettes based on time-dependent labeling patterns in the metabolome. Plants photosynthesizing under limiting irradiance and ambient CO₂ in a custom-built chamber were transferred into a ¹³CO₂-enriched environment. The isotope labeling patterns of 40 metabolites were obtained using liquid or gas chromatography coupled to mass spectrometry. Labeling kinetics revealed striking differences between metabolites. At a qualitative level, they matched expectations in terms of pathway topology and stoichiometry, but some unexpected features point to the complexity of subcellular and cellular compartmentation. To achieve quantitative insights, the data set was used for estimating fluxes in the framework of kinetic flux profiling. We benchmarked flux estimates to four classically determined flux signatures of photosynthesis and assessed the robustness of the estimates with respect to different features of the underlying metabolic model and the time-resolved data set.

INTRODUCTION

Photosynthetic CO₂ assimilation is central to life, and understanding its regulation and integration with end-product synthesis is a major challenge in plant biochemistry. Existing studies in plants mainly focused on defining metabolic pathways and their subcellular compartmentation and studying the regulation of component enzymes (Bauwe et al., 2010; Hibberd and Covshoff, 2010; Stitt et al., 2010). In the past decade, high-throughput methods have been applied to measure metabolites involved in photosynthetic C metabolism (Cruz et al., 2008; Timm et al., 2008; Arrivault et al., 2009; Suzuki et al., 2012), to study the relation between enzyme activities and steady state metabolite levels (Sulpice et al., 2010), to analyze gene expression (Biehl et al., 2005), to relate transcript levels to in vitro activities of the encoded enzymes (Gibon et al., 2004), and to estimate rates of turnover of individual enzymes (Piques et al., 2009). An emerging picture is that in vitro activities of enzymes only partly reflect the levels of transcripts, that many enzymes exhibit slow turnover rates, and that there is little relation between in vitro activities of enzymes and the levels of individual metabolites in photosynthetic C metabolism.

The most biologically important description of metabolism is the set of metabolic fluxes that it generates. This represents the integrated output of the molecular machinery and biochemical characteristics studied by other high-throughput technologies. It is also a key determinant of cellular physiology and growth (Blank and Sauer, 2004). The goal of this study is to use stable isotope labeling with ¹³CO₂ to estimate fluxes in the well-characterized photosynthetic metabolism in a land plant leaf. This is a challenging task given the complex topology and subcellular compartmentation of the pathways and the wide range of fluxes and turnover times of the metabolites that are involved in them.

Ribulose-1,5-bisphosphate carboxylase/oxygenase (Rubisco) catalyzes the initial carboxylation reaction, in which CO₂ is added to the 5C carbon acceptor ribulose-1,5-bisphosphate (RuBP) to form two molecules of 3-phosphoglycerate (3PGA). Most of the 3PGA is used to regenerate RuBP in the Calvin-Benson cycle (CBC). This involves the reduction of PGA to triose-phosphates, a process that consumes the vast majority of the NADPH and ATP generated in the light reactions, followed by a series of condensation, cleaving, and phosphatase and phosphorylation reactions that rearrange 3C triose-phosphate skeletons into the 5C carbon acceptor RuBP. The net C gain (in the ideal case, one-sixth of fixed C) is used to synthesize end products: mainly Suc and starch. Some C is converted to organic acids and amino acids. This requires the assimilation of additional CO₂ in the anaplerotic reaction catalyzed by phosphoenolpyruvate carboxylase (PEPC).

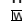
Rubisco catalyzes a side reaction in which RuBP reacts with O₂ to form one molecule of 3PGA and one molecule of 2-phosphoglycolate. Under current atmospheric conditions, in organisms without a C concentrating mechanism, this side reaction occurs at 25% of the rate of the reaction with CO₂.

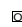
¹ These authors contributed equally to this work.

² Current address: Leibniz Institute of Plant Genetics and Crop Plant Research, Corrensstrasse 3, 06466 Gatersleben, Germany.

³ Address correspondence to fernie@mpimp-golm.mpg.de.

The author responsible for distribution of materials integral to the findings presented in this article in accordance with the policy described in the Instructions for Authors (www.plantcell.org) is: Alisdair R. Fernie (fernie@mpimp-golm.mpg.de).

 Online version contains Web-only data.

 Open Access articles can be viewed online without a subscription.
www.plantcell.org/cgi/doi/10.1105/tpc.112.106989

(Sharkey, 1988). 2-Phosphoglycollate is salvaged via a complex pathway termed photorespiration, in which it is converted via glycolate to glyoxylate, transaminated to Gly, decarboxylated to Ser, and converted back via hydroxypyruvate and glycerate to 3PGA. This process results in a 25 to 30% decrease in the net rate of C fixation and a 20% decrease in quantum yield (Foyer et al., 2009; Bauwe et al., 2010).

In eukaryotic algae and plants, a further major complication is introduced by subcellular compartmentation. Briefly, the CBC and starch synthesis occur in the chloroplast, while triose-phosphates are exported to the cytosol for conversion to Suc. Photorespiration occurs in the chloroplast, peroxisome, cytosol, and mitochondria. Organic acid and amino acid metabolism occurs in the plastid, cytosol, and mitochondria, and large amounts of these metabolites accumulate in the vacuole (for details, see Supplemental Methods 1 online).

Pioneering isotope labeling experiments with $^{14}\text{CO}_2$, which were performed almost 60 years ago (Calvin, 1956), played a key role in the discovery of the CBC (Benson, 2002). Since then, isolated studies have analyzed ^{14}C labeling kinetics at the subcellular level and used this information to estimate fluxes at selected reaction steps (Stitt et al., 1983). However, technical challenges meant that most ^{14}C labeling studies were restricted to analyses of the rate of carboxylation and the distribution of fixed C between end products. In the last 10 years, new analytical chemistry tools, like metabolomics, have increased our knowledge of metabolism (Nunes-Nesi et al., 2005; Arrivault et al., 2009; Stitt et al., 2010). The use of stable isotopes (Schaefer et al., 1980; MacLeod et al., 2001; Schwender et al., 2004a; Römisch-Margl et al., 2007), coupled with improvements in analytical methods, has opened new possibilities for metabolism research (DellaPenna and Last, 2008; Saito and Matsuda, 2010).

Successful applications of ^{13}C -labeling and gas chromatography-time-of-flight-mass spectrometry (GC-TOF-MS) have been reported for a range of species and tissues, including *Escherichia coli* (Yuan et al., 2006; Haverkorn van Rijsewijk et al., 2011), *Saccharomyces cerevisiae* (Birkemeyer et al., 2005), photoautotrophic cyanobacteria, *Synechocystis* sp (Huege et al., 2011; Young et al., 2011), *Arabidopsis thaliana* (Huege et al., 2007; Williams et al., 2010), soybean (*Glycine max*) embryos (Sriram et al., 2004), *Brassica napus* (Schwender et al., 2004b, 2006), and potato (*Solanum tuberosum*) tubers (Roessner-Tunali et al., 2004). However, to date, there are relatively few reports that use $^{13}\text{CO}_2$ to study metabolism in photosynthesizing plant tissue. Furthermore, these studies usually analyzed individual leaves that were harvested from the plant following incubation of part of the leaf with $^{13}\text{CO}_2$ and could be compromised by export of enriched compounds to other parts of the leaf or the remainder of the plant. Ito and Mitsumori (1992) measured ^{13}C incorporation into photorespiratory intermediates, several amino acids, and sugars in intact sunflower (*Helianthus annuus*) leaves, while Hasunuma et al. (2010) investigated labeling of CBC intermediates and sugar phosphates in tobacco (*Nicotiana tabacum*) leaf discs. Huege et al. (2007) demonstrated a method for the full labeling of *Arabidopsis* rosettes by growing plants from germination onwards in a sealed chamber in a $^{13}\text{CO}_2$ atmosphere and subsequently used GC-TOF-MS to study the decay

of ^{13}C in a set of metabolites. Eisenreich and Bacher (2007) suggested using $^{13}\text{CO}_2$ as a universal precursor for in vivo experiments in photosynthesizing plant tissues; however, these authors focused their research on NMR analysis of pathways of secondary metabolism.

The topology of photosynthetic C fixation pathways poses a particular challenge for flux studies. Most methods for analyzing ^{13}C enrichment patterns and estimating fluxes assume steady state metabolic states and steady state labeling states (reviewed in Ratcliffe and Shachar-Hill, 2006). Very little information about fluxes can be extracted from data obtained at isotopic steady state following the feeding of $^{13}\text{CO}_2$. On the other hand, qualitative analysis of non-steady state labeling kinetics with ^{13}C is extremely challenging due to the large number of isotopomers (Antoniewicz et al., 2007; Young et al., 2008). Such analyses are further complicated by the large range of turnover times of metabolite pools, which span between <1 s for many metabolites in the CBC to ~ 1 min for intermediates in Suc synthesis to several minutes for intermediates of photorespiration (Stitt et al., 1983; Arrivault et al., 2009; for details, see Supplemental Methods 2 online).

In this study, we used a custom-designed labeling chamber to carry out short-term $^{13}\text{CO}_2$ labeling of intact *Arabidopsis* rosettes under ambient steady state conditions. Several complementary analytical platforms were applied, including GC-TOF-MS and two recently developed liquid chromatography-tandem mass spectrometry (LC-MS/MS) platforms (Lunn et al., 2006; Arrivault et al., 2009), allowing quantitative determination and ^{13}C enrichment calculation of 40 metabolites from the CBC, Suc and starch synthesis, glycolysis, amino acid and organic acid metabolism, as well as trehalose-6-phosphate (Tre6P) metabolism. The main aims of this study were as follows: (1) to qualitatively test expectations about the labeling kinetics of metabolites in photosynthetic metabolism in a higher plant, (2) to use labeling kinetics to provide information about what proportion of the metabolite pool is likely to be involved in photosynthetic metabolism, and (3) to use this information to estimate a selected set of fluxes through photosynthetic end products, which can be compared with independent measurements to benchmark the data and model.

RESULTS

Construction of the ^{13}C Labeling System

Several aspects had to be reconciled in the design of a chamber to perform $^{13}\text{CO}_2$ labeling of whole *Arabidopsis* rosettes under physiological conditions (see Supplemental Figure 1 online): (1) The volume had to be as small as possible to minimize the time lag after introducing $^{13}\text{CO}_2$ but large enough to hold a 5-week-old *Arabidopsis* plant in a pot; (2) the chamber had to be built from transparent material that did not drastically alter light quality; and (3) the rosette has to be quenched in ambient light and without allowing entry of $^{12}\text{CO}_2$ due to the rapid turnover of CBC metabolites (see Introduction). We used commercially available 380-mL in vitro plant culture boxes (Magenta GA-7). While rapid quenching in large-leaved species is best performed by freeze clamping the leaf between two liquid N_2 precooled

metal blocks (Badger et al., 1984; Quick et al., 1991), this is not practical for *Arabidopsis* rosettes. Instead, the plants were grown with plastic foil under the rosette and quenched by flooding them with a large volume of liquid N₂ poured down a funnel inserted through a small inlet in the side of the box. This allowed quenching without shading the plants or opening the box.

***Arabidopsis* Rosette Labeling Experiment**

Five-week-old plants were rapidly transferred from growth chambers to the labeling chamber, which was continuously washed through the whole experiment by a stream of air (5 liters min⁻¹) prepared from cylinders containing pure N₂, O₂, and ¹³CO₂ that had been mixed in a gas blender (see Methods). Plants were harvested 5 and 10 s and 1, 3, 10, 20, and 60 min after the start of labeling. Shorter pulses were not possible due to the dead space of the chamber and the CO₂ inside the plant leaf. Due to the small size and rapid turnover of pools in the CBC, these treatments do not allow resolution of individual fluxes in the CBC (see below) but do facilitate estimation of overall flux in the CBC and the fluxes in photorespiration as well as starch and Suc synthesis.

Analysis of Isotopomers of 40 Metabolites

Samples were analyzed using three analytical platforms, namely, GC-TOF-MS, ion exchange LC-MS/MS, and reverse-phase LC-MS/MS. This allowed quantification of 40 metabolites from the CBC, starch and Suc biosynthesis, the photorespiratory pathway, amino acid metabolism, glycolysis, the tricarboxylic acid cycle (TCAC), and Tre6P metabolism. The mass distribution of all metabolites determined shifted to a higher mass-to-charge ratio with increasing labeling time, as illustrated for 3PGA, which is the first product of CO₂ fixation (see Supplemental Figure 2 online). Labeling kinetics were reproducible between three biological replicates (e.g., average ¹³C enrichment and SD were 65.8 and 4.9% for RuBP isotopomer, corresponding to the fully labeled molecule after 1 h of labeling and 40.8 and 3.5% for Ala). The total content of the measured metabolites did not change significantly between different labeling times (see Supplemental Table 1 online).

The Pattern of Labeling Can Be Separated by *k*-Means Clustering

To obtain an overview of the labeling kinetics, the average ¹³C enrichment profiles over the three biological replicates for all measured metabolites were subjected to *k*-means clustering based on Euclidian distance. To determine number of clusters, *k*, the crude rule of thumb by Mardia et al. (1979), was used, whereby

$$k \approx \sqrt{N/2} = 4.47$$

and *N* = 40 is the number of metabolites. This analysis resulted in four clusters with very different labeling patterns (Figure 1A). The abbreviations used in the following text are

defined in the legend of Figure 1. The first cluster, which was labeled the fastest, comprises all the CBC intermediates, together with ADP-Glc (ADPG) and 2-phosphoglyceric acid (2PGA). The second cluster consists of Glc-1-phosphate (G1P), Glc-6-phosphate (G6P), UDP-Glc (UDPG), and Suc-6-phosphate (Suc6P), which are intermediates in Suc synthesis, two photorespiratory intermediates (glycerate and Ser), maltose, pyruvate, and Ala. Gly is assigned to the third cluster, but this may be because a large proportion of the pool is not labeled at all (see below). The third and fourth clusters comprise slowly labeled metabolites (hexose sugars, organic acids, other amino acids, Tre6P, and trehalose).

Visualization of the clusters on a simplified scheme of photosynthetic metabolism revealed that metabolites in a given pathway usually show similar labeling kinetics (Figure 1B). Similar labeling kinetics for two metabolites implies that the metabolites are in, or are close to, isotopic equilibrium. All CBC intermediates are in close isotopic equilibrium with each other and with ADPG, which is an intermediate in the starch synthesis pathway, and 2PGA, which is located exclusively in the cytosol and is a precursor for organic acid synthesis. Similarly, G6P, G1P, UDPG, and Suc6P, which are predominantly located in the cytosol and are intermediates of Suc synthesis, cluster together, as do pyruvate and Ala, which is synthesized from pyruvate, and Tre6P and trehalose. It is reassuring that the known topology of the metabolic pathways can be broadly recapitulated by an analysis of the labeling kinetics. However, it should be noted that this analysis does not provide information about the magnitude of fluxes. Isotopic equilibrium can be established by a rapid interconversion of two metabolites, even if there is negligible net flux. Even if labeling kinetics do reflect net flux between two metabolites, the absolute value of the flux will depend on the pool sizes.

Pool Sizes and Compartmentation of Metabolites

The absolute levels of the metabolites are shown in Table 1. There is a large dynamic range, even for metabolites in the same pathway (e.g., 11.7 and 173 nmol g fresh weight [FW]⁻¹ for G1P and G6P, respectively), with the extremes being 0.55 (ADPG) and >1000 (Suc, Ser, Fru, and Glc) nmol g FW⁻¹.

Pool sizes in the vacuole, plastid, and cytosol were estimated using nonaqueous fractionation (Gerhardt et al., 1987). Nonaqueous fractionation does not generate pure organelle preparations, but instead, a set of fractions that are partially enriched in different subcellular compartments. The subcellular distribution of metabolites of interest is estimated by (multidimensional) regression against marker traits (usually enzyme activities) that are specific for a particular compartment. However, it is not possible to accurately determine the subcellular level in a compartment that contains only a small proportion of the total pool (Gerhardt et al., 1987). There were large differences between metabolites in their subcellular distributions (Table 1). Some metabolites, such as RuBP, sedoheptulose-1,7-bisphosphate (SBP), Fru-1,6-bisphosphate (FBP), ADPG, UDPG, malate, fumarate, and isocitrate were largely in a single compartment, while others like dihydroxyacetone phosphate (DHAP), 3PGA, hexose phosphates, hexoses, most amino acids, and organic

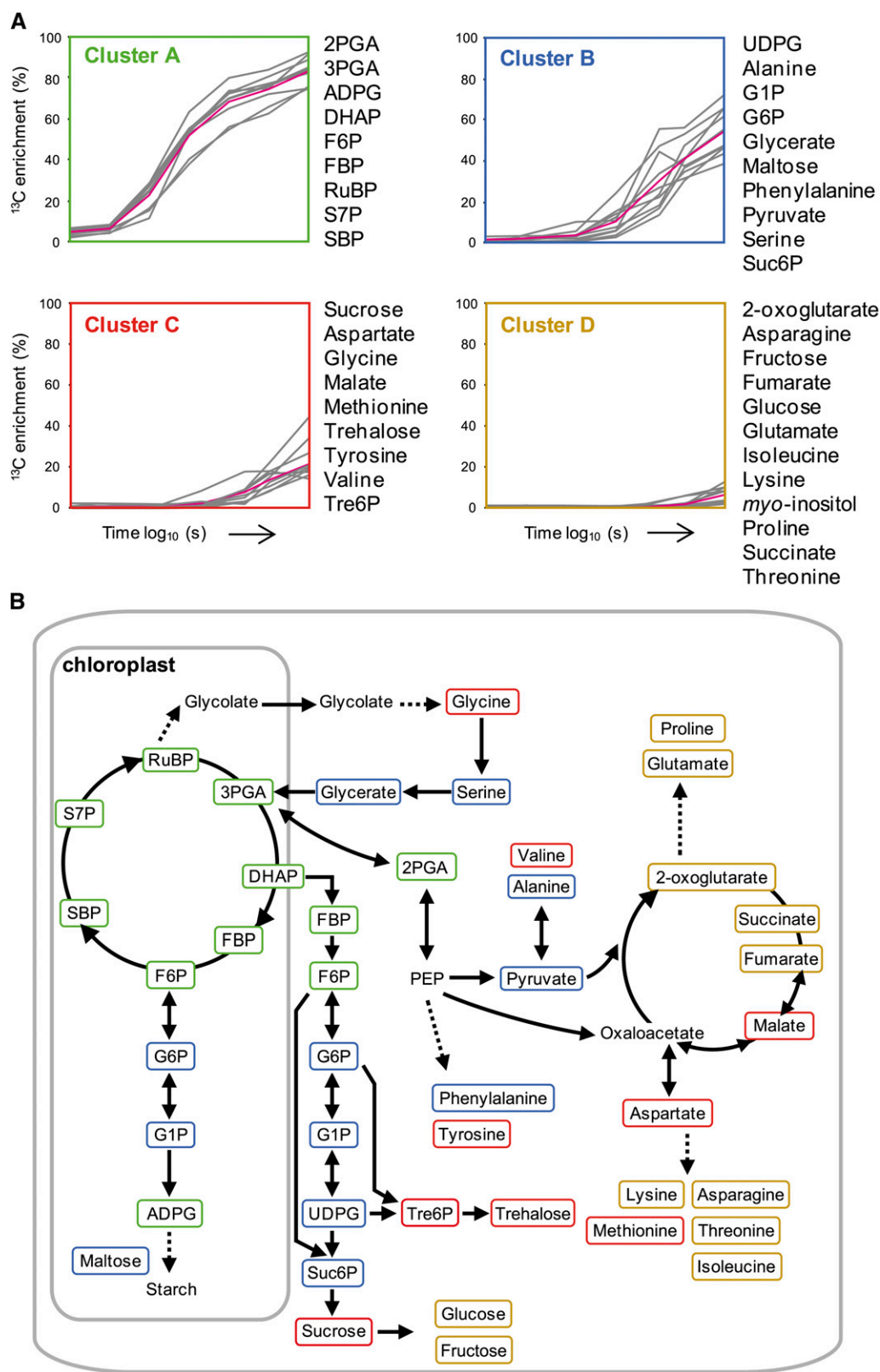


Figure 1. Overview of ^{13}C Labeling Kinetics from Primary C Metabolism.

acids were present in two or more compartments. This resembles results from earlier studies in spinach (*Spinacia oleracea*) (Gerhardt et al., 1987; Riens et al., 1991; Winter et al., 1994), maize (*Zea mays*) (Weiner and Heldt, 1992), barley (*Hordeum vulgare*) (Winter et al., 1993), and *Arabidopsis* (Krueger et al., 2011) leaves.

The Labeling Kinetics for CBC Intermediates and Glycolytic Intermediates Follow Similar Patterns

Figure 2A provides detailed information about the labeling kinetics of individual CBC intermediates. Label was incorporated at the earliest time points, leading to a rapid decrease in the proportion of the metabolite present as the ^{12}C isotopomer, a progressive increase and then decline of intermediate forms, and a steady increase in the ^{13}C isotopomer in which all C atoms are labeled. In Figures 2B and 2C, the average ^{13}C enrichment is plotted on a log scale to better illustrate the enrichment kinetics. Even at the earliest time points, all CBC intermediates displayed similar relative labeling (see Supplemental Figure 3A online for additional plots). When ^{13}C enrichment of CBC intermediates was plotted against ^{13}C enrichment of 3PGA, which is the first product of the CO_2 assimilation, very high values were obtained for the Pearson correlation coefficient (see Supplemental Figure 3B online). This parallel labeling is in accordance with the very short half-times estimated from pool size and pathway stoichiometry (Arrivault et al., 2009). One exception was FBP, which was labeled more slowly than DHAP, from which FBP is formed, and more slowly than metabolites located further downstream in the CBC, like SBP, sedoheptulose-7-phosphate (S7P), and RuBP. This indicates that a significant part of the FBP pool is not directly involved in the CBC.

Another unexpected finding was that CBC intermediates do not rapidly become fully labeled (Figure 2; see Supplemental Figure 3A online). After 10 min, the average ^{13}C enrichment was ~70% for RuBP, 3PGA, DHAP, and S7P, 65% for SBP, and 55% for FBP and F6P. Even after 60 min, the most highly labeled metabolite, S7P, was only enriched to 92%, while the other CBC intermediates showed labeling around 70% (see Supplemental Table 2 online). One explanation for this behavior might be internal recycling of ^{12}C isotope from unlabeled pools (see Discussion).

Labeling Kinetics for Intermediates in Starch and Suc Synthesis

Starch is synthesized from F6P via G6P, G1P, and ADPG in the chloroplast, while Suc is synthesized from triose-phosphates

that are exported to the cytosol and converted via FBP, F6P, G6P, G1P, UDPG, and Suc6P to Suc. The labeling kinetic of ADPG was only slightly slower than labeling kinetics for CBC metabolites (Figure 2; see Supplemental Figure 3A online). It should be noted that the ADPG pool is very small, with the result that ADPG will turn over rapidly even though flux through it is much smaller than in the CBC (see later). Slower labeling was observed for F6P, followed by G6P, G1P, UDPG, Suc6P, and even slower labeling for Suc (Figure 2 and see below). These results confirm that the intermediates in Suc synthesis have a much shorter turnover time than those in the CBC (Stitt et al., 1983). Some of the F6P, G6P, and G1P are located in the chloroplast (Stitt et al., 1983; Gerhardt et al., 1987). These plastid pools are expected to label rapidly; labeling kinetics of plastid F6P should resemble those of other CBC intermediates, while those of ADPG provide a minimum estimate for the labeling kinetics of plastid G6P and G1P pools. Therefore, the labeling kinetics of the cytosolic F6P, G6P, and G1P pools would be anticipated to be even slower than those of the total pools of these metabolites.

Surprisingly, there was a marked difference between the labeling kinetics of G1P and G6P (Figure 2A; see Supplemental Figure 3A and Supplemental Table 2 online). These two metabolites are interconverted via a reversible reaction catalyzed by phosphoglucomutase. The ^{12}C isotopomer decay of G1P was much slower than that of G6P. After 20 min, it almost reached a plateau in which over half of the pool still consisted of nonlabeled isotopomer. When the ^{13}C isotopomers are inspected, the intermediate isotopomers rise and fall, and the fully labeled form is dominant at 20 and 60 min of G1P (Figure 2A). This isotopomer labeling pattern indicates that there are two pools of G1P, of which one is subject to labeling and the other is effectively unlabeled. This labeling pattern is unlikely to be generated by an influx of unlabeled ^{12}C into G1P because this would lead to a slower but monophasic decrease of the ^{12}C isotopomer and the accumulation of incompletely labeled ^{13}C isotopomers. UDPG showed a similar, though not so marked, response. This contrasts with Suc6P, which after 20 to 60 min was almost as heavily labeled as the CBC intermediates and more heavily labeled than G6P, G1P, and UDPG, despite being located downstream of the latter metabolites in the pathway of Suc synthesis (Figure 2; see Supplemental Figure 3A, Supplemental Table 2, and Supplemental Data Set 1 online).

The incomplete labeling of G1P might potentially be due to another molecule that is not involved in photosynthetic metabolism but coelutes with G1P from the liquid chromatography and has the same mass and fragment ion as G1P. We checked the specificity of the G1P measurements by showing that two

Figure 1. (continued).

(A) *k*-means clustering. Gray lines show the ^{13}C enrichment (calculated as in Methods) of individual metabolites, and magenta lines show average ^{13}C enrichment of all metabolites in the cluster.

(B) Schematic representation of labeling kinetics. The scheme distinguishes the plastidic compartment but not the cytosol, peroxisomes, mitochondria, and vacuole. Metabolites are highlighted according to cluster following the color scheme in **(A)**. Solid and double-headed arrows represent irreversible and reversible reactions, respectively. Dashed arrows represent conversions involving several steps.

Table 1. Amount and Subcellular Distribution of Compounds in *Arabidopsis*

Compounds	Amount (nmol g FW ⁻¹)	Plastid (%)	Cytosol (%)	Vacuole (%)
3PGA ^a	200 ± 45	44	56	0
2PGA ^a	20 ± 4.5	0	100	0
ADPG ^a	0.55 ± 0.05	100	0	0
DHAP ^a	2.7 ± 0.6	23	77	0
F6P ^a	86.4 ± 14.6	34	66	0
FBP ^a	8.9 ± 2.3	70	30	0
G1P ^a	11.7 ± 2.4	8	92	0
G6P ^a	173 ± 51	17	83	0
RuBP ^a	46.7 ± 8.2	83	17	0
S7P ^a	28.0 ± 5.4	82	18	0
SBP ^a	9.6 ± 3.0	75	25	0
UDPG ^a	35.7 ± 5.7	0	100	0
R5P ^a	1.2 ± 0.2	49	51	0
X5P+Ru5P ^a	8.7 ± 2.6	100	0	0
Suc6P ^a	0.82 ± 0.36	0	100	0
PEP ^a	52.5 ± 9.9	6	94	0
Gly	543 ± 59	28	33	39
Glycerate	169 ± 65	31	47	22
Ser	4,265 ± 326	36	22	42
myo-inositol	922 ± 108	66	0	34
Suc	3,432 ± 167	19	31	50
Trehalose	20.8 ± 3.0	50	0	50
Glu	3,682 ± 1,042	30	42	28
Malate	1,820 ± 547	0	0	100
2-Oxoglutarate	63.1 ± 18.8	6	35	59
Pyruvate	99.2 ± 35.6	24	31	45
Val	139 ± 16	32	0	68
Ile	38.9 ± 4.5	33	0	67
Pro	641 ± 90	31	24	45
Thr	459 ± 58	42	0	58
Fumarate	1,154 ± 47	0	0	100
Asp	1,050 ± 346	19	46	35
Phe	53.1 ± 6.9	48	0	52
Asn	380 ± 25	30	17	53
Fru	1,458 ± 30	0	12	88
Glc	2,669 ± 475	12	23	65
Arg	164 ± 18	42	0	58
Tyr	9.8 ± 1.2	45	0	55
Citrate	1,916 ± 505	0	0	100
Shikimate	35.9 ± 7.6	37	22	41
Succinate	84.0 ± 48.2	4	17	79
Ala	228 ± 24	16	14	70
Gln	2,349 ± 177	11	0	89
Nitrate	224,000 ± 4,100	0	0	100
Aconitate	14.5 ± 5.5	0	0	100
Isocitrate	33.5 ± 3.6	0	0	100
Lys	n.d.	n.d.	n.d.	n.d.
Maltose	n.d.	n.d.	n.d.	n.d.
Met	9.9 ± 1.4	42	13	45

Data are from three independent nonaqueous gradients. 2PGA is assumed to be only in the cytosol and its amount to be 10% of the 3PGA amount. Subcellular distributions (%) were calculated using a three-compartment model (plastid, cytosol, and vacuole). For metabolites marked with an "a," a two-compartment model was used (plastid and cytosol). n.d., not determined.

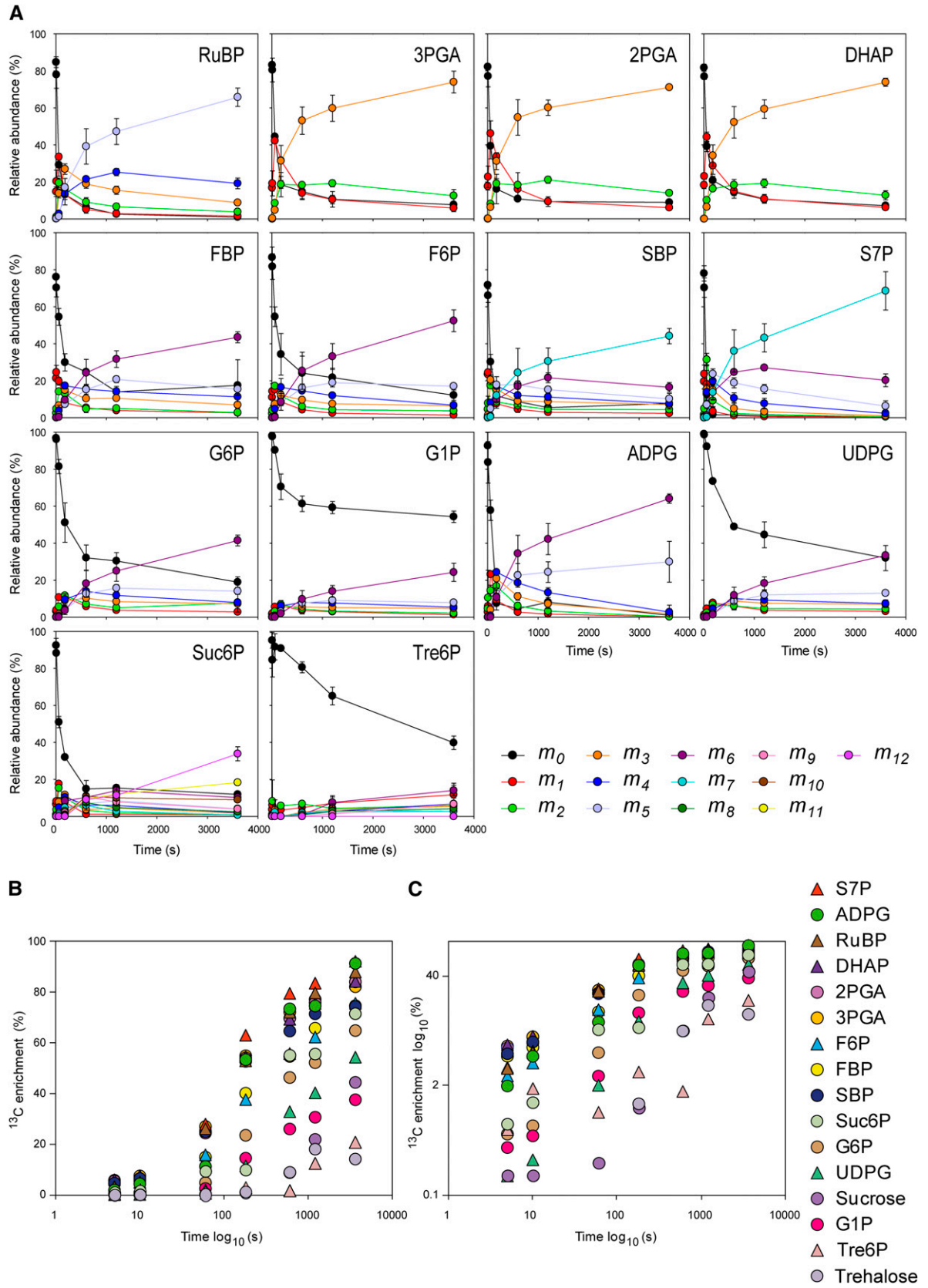


Figure 2. ^{13}C Labeling Kinetics of Metabolites from CBC, Starch, Suc, and Trehalose Biosynthesis Pathways.

different enzymatic reactions that use G1P completely remove the corresponding signal (see Supplemental Figure 4 online). This behavior could not be explained by differences in pool sizes, since the G1P pool is 14 times smaller than G6P (Table 1), or subcellular compartmentation, as G1P and G6P showed a similar distribution between the cytosol and chloroplasts when *Arabidopsis* tissue was fractionated on nonpolar density gradients (Table 1). We also checked if the deviant response of G1P was due to a large proportion being located in cells that did not perform photosynthesis. The petiole and major veins were dissected from leaf lamina and the cut material was analyzed by LC-MS/MS. The small difference observed in the distribution of G1P and G6P (55 and 44% in petiole and 45 and 56% in leaf lamina for G1P and G6P, respectively) could not explain the incomplete labeling kinetic of G1P.

Labeling Kinetics of Sugars

Suc was gradually labeled over the entire 60-min period, while Glc and Fru were only very slowly labeled (Figure 3A). This confirms results from earlier studies with $^{14}\text{CO}_2$ labeling (Jensen and Bassham, 1966; King et al., 1967; Stitt et al., 1980), which established that Suc is the major product of photosynthesis. Glc and Fru are formed by hydrolysis of Suc by invertase, which is evidently a slow process in *Arabidopsis*, at least under the experimental conditions used here.

Maltose showed faster labeling than Suc. While ^{13}C enrichment in Suc rose gradually through the entire time course (1, 9, 22, and 45% at 3, 10, 20, and 60 min), the equivalent values for maltose were 5, 44, 37, and 47% (Figure 3A; see Supplemental Table 2 online). The labeling kinetics of individual isotopomers indicates that about half the maltose pool is subject to labeling, while the other half is effectively unlabeled (see Supplemental Figure 5 and Supplemental Data Set 1 online). As the absolute pool size of Suc is much larger than that of maltose (Table 1), this does not alter the conclusion that Suc is the main product of photosynthesis. Nevertheless, it raises questions with respect to the source of the maltose.

Labeling Kinetics of Photorespiratory Intermediates

The three metabolites from photorespiration detected by our analysis (Gly, Ser, and glycerate) showed moderately rapid labeling (Figure 3B). ^{13}C enrichment of Gly displayed different kinetics compared with that in Ser and glycerate. After a short lag, Gly labels rapidly for 10 min, but the speed of labeling then abruptly slows down, whereas labeling of glycerate and Ser continues to increase. The ^{12}C isotopomer of Gly decreases to ~80% of the total Gly pool

in the first 10 min and remains at this value for the remainder of the experiment (Figure 4A). Furthermore, by 10 min, most of the ~20% decrease of the ^{12}C isotopomer can be accounted for by an increase of the isotopomer containing two ^{13}C atoms. As for G1P, this labeling pattern strongly indicates that there are two pools of Gly in the rosette, with one (~20% of the total pool) being involved in photorespiration, and another pool (~80% of the total) not participating in this process. A similar but less marked response was seen for Ser and glycerate (Figures 4B and 4C).

Labeling of Amino Acids and Organic Acids

Photosynthetic chloroplasts lack a complete glycolytic sequence (Stitt and Rees, 1980; Andriotis et al., 2010). Synthesis of organic acids and amino acids therefore starts with the conversion of 3PGA to 2PGA and phosphoenolpyruvate (PEP) in the cytosol. PEP is then further metabolized via pyruvate kinase (PK) and PEPc.

The labeling kinetics of 3PGA, which is present at equivalent levels in the chloroplast and cytosol (Table 1), and 2PGA, which is exclusively located in the cytosol (Stitt et al., 1980), are almost identical (see Supplemental Table 2 and Supplemental Data Set 1 online), suggesting a high exchange rate between the plastid and the cytosol (Stitt et al., 1983). PEP could not be analyzed due to the instability of this metabolite during extraction.

Pyruvate showed progressive labeling for the first 10 to 20 min but then slowed down such that only about half the total pool was labeled at all, but this part was mainly the isotopomer containing three ^{13}C . As already discussed, this response indicates the presence of two pools: one that is labeled with a half-time of 10 to 20 min and one that is still effectively unlabeled even after 60 min and is presumably not involved in the pathways that use newly fixed C. The rate of labeling in the first 10 to 20 min is slower than for 3PGA but still marked, especially if the enrichment is normalized by subtracting the proportion that remains as the ^{12}C isotopomer after 60 min.

Labeling of organic acids and amino acids varied with respect to the speed of labeling and the proportion labeled (Figure 3C; see Supplemental Figure 6 online). Organic acids involved in the TCAC, like isocitrate, 2-oxoglutarate, succinate, fumarate, and malate, were labeled relatively slowly, with only a small proportion being labeled at 60 min, as previously demonstrated (Tcherkez et al., 2005, 2009). As previously shown (Gauthier et al., 2010; Tcherkez et al., 2012a) the labeling of 2-oxoglutarate and Glu was also very slow. Many other metabolites downstream of PK and PEPc were also only weakly labeled, including malate, fumarate, and succinate (Figure 3C; see Supplemental Figure 6 online; see also Discussion). Some amino acids showed more rapid labeling. This included Ala and Asp, which are formed by transamination

Figure 2. (continued).

(A) Time course of mass distribution. The relative abundance of each isotopomer (m_n) for a given metabolite is represented; n is the number of ^{13}C atoms incorporated.

(B) and **(C)** ^{13}C enrichment. The x axis corresponds to the labeling time on a \log_{10} scale. In **(C)**, the y axis corresponds to ^{13}C enrichments on a \log_{10} scale.

Values (%) are average of three biological replicates \pm SD, with the exception of Suc6P and Tre6P at time 180 s ($n = 1$). For clarity, SDs are not shown in **(B)** and **(C)**.

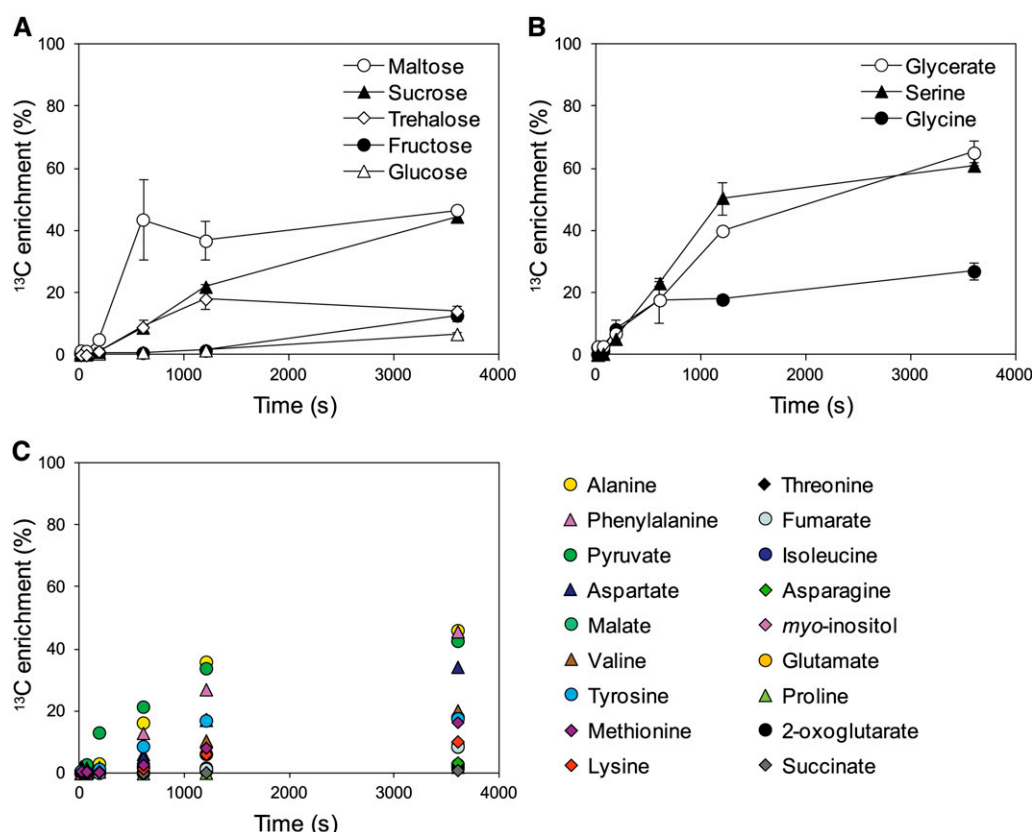


Figure 3. ^{13}C Enrichment of Sugars, Organic Acids, and Amino Acids.

Sugars (**A**), photorespiration cycle intermediates (**B**), and organic acids and amino acids (**C**). Values (%) are average of three biological replicates \pm sd.

reactions from pyruvate and oxaloacetate. Ile and Val, which are synthesized from pyruvate, also displayed quite rapid labeling of a subpool, representing $\sim 20\%$ of the total pool in the rosette. The relatively rapid labeling of aromatic amino acids is consistent with them being synthesized from E4P, which is an intermediate in the CBC, and PEP. Asn, Thr, Lys, and Met, which are derived from Asp, were labeled only slowly and partially.

Labeling of Tre6P, Trehalose, and Myo-Inositol

The ^{12}C isotopomer decay of Tre6P was slow and almost linear over the time course of the experiment (Figure 2A; see Supplemental Figure 3A online), and, after 60 min of labeling, the unlabeled form still represented the predominant Tre6P isotopomer ($\sim 40\%$). Tre6P showed mild ^{13}C enrichment, with up to 21% at 60 min (Figures 2B and 2C). Trehalose also showed only mild ^{13}C enrichment (i.e., up to 9, 18, and 14% at 10, 20, and 60 min, respectively) (Figures 2B and 2C; see Supplemental Table 2 online). As the trehalose pool is 370-fold smaller than the Suc pool and is much less weakly labeled, it is only a very minor product. Based on their enrichment, Tre6P and trehalose clustered in the same group (Figure 1).

Labeling of myo-inositol was very slow (see Supplemental Figure 6A online), with ^{13}C enrichment of $\sim 3\%$ after 60 min of labeling (see Supplemental Table 2 online).

Utilization of Experimental Data for Flux Estimation by Kinetic Flux Profiling

Methods available to model fluxes from labeling data are outlined in Supplemental Methods 2 online. To model fluxes from our data set, we chose to use kinetic flux profiling (KFP) (Yuan et al., 2006, 2008). While some of the existing approaches allow usage of different fragments and, thus, potentially more informative data sets, KFP facilitates the computation of individual reaction fluxes in complex networks from incomplete data sets. KFP uses a mass action-like differential equation model for the washout of the unlabeled fraction of metabolic pools (compare Methods and Supplemental Methods 3 online). In the original formulation, KFP was used to fit fluxes locally, using prior knowledge of the reactions that take place in the vicinity of a metabolite (see example 3 in Supplemental Methods 3 online). Here, we extend the applicability of KFP by providing a global fit to the labeling data. The global fit is performed via a simulated annealing, the results of which are then used in gradient descent, both with respect to a variance-weighted mean squared error function (see Supplemental Methods 4 online), and confidence intervals are estimated by standard procedure (see Supplemental Methods 5 online).

The metabolic model used in our calculations (Figure 5A; see Supplemental Methods 6 online) comprises the CBC, photorespiration, and starch, Suc, trehalose, and myo-inositol biosynthesis.

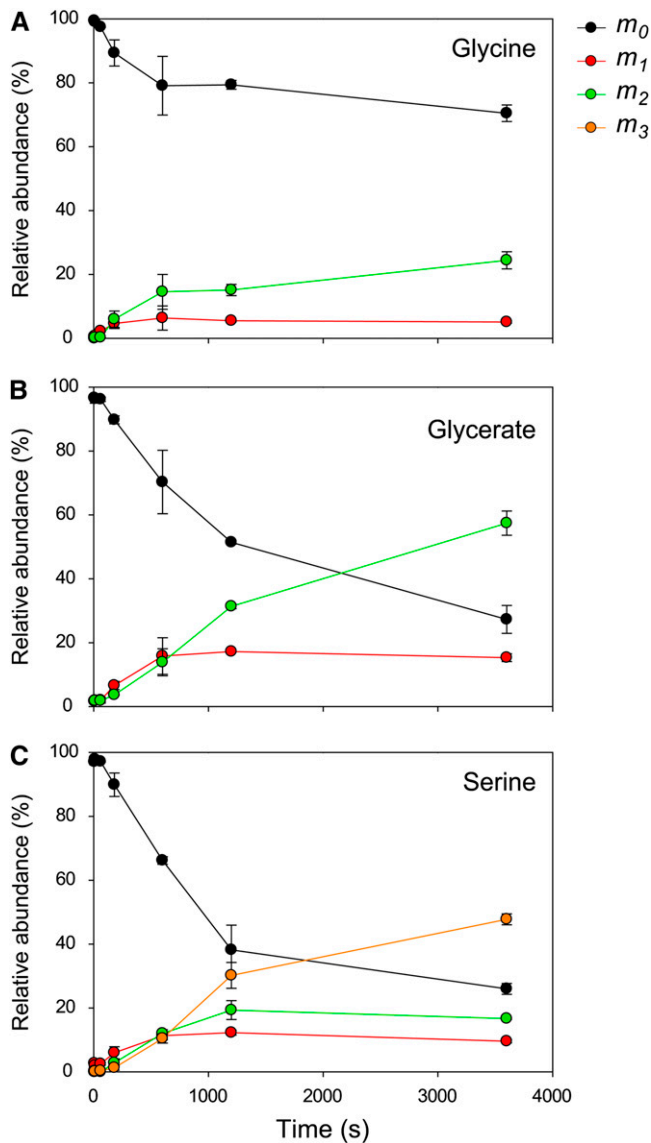


Figure 4. Time Course of Mass Distribution of Photorespiration Cycle Intermediates.

Gly (A), glycerate (B), and Ser (C). The relative abundance of each isotopomer (m_n) for a given metabolite is represented, and n corresponds to the number of ^{13}C atoms incorporated in the metabolite. Values (%) are average of three biological replicates \pm sd.

Fluxes from PEP to organic acids and amino acids were omitted because inherent features of the pathway topology prevent accurate estimation of flux from the $^{13}\text{CO}_2$ labeling kinetics in this part of metabolism (see Discussion). As we later show, the overall flux is low, and its omission does not introduce a large error into estimates of fluxes in the remainder of photosynthetic metabolism. CBC intermediates were assumed to be located exclusively in the plastid (Table 1) except for DHAP, 3PGA, F6P, and FBP. As the plastidic and cytosolic pools of 3PGA and DHAP are in rapid isotopic equilibrium (Stitt et al., 1983), they

were modeled as a single pool. Further evidence for this assumption is provided by the observation that 2PGA, which is exclusively in the cytosol, showed similar labeling kinetics to 3PGA and DHAP, which are distributed between the plastid and cytosol (Table 1, Figure 2A; see Supplemental Figure 3 online). Starch and Suc biosynthesis are known to be exclusively located in the plastid and cytosol, respectively (Stitt et al., 1980), with the plastidic and cytosolic pools showing different labeling kinetics (Stitt et al., 1983). Nonaqueous fractionation data were therefore used to explicitly measure the plastid and cytosolic pools of F6P, G6P, and G1P in our material (Table 1; see Supplemental Table 3 online) and to provide experimental evidence that Suc6P is almost exclusively located in the cytosol. Tre6P was assumed to be cytosolic. Compartmentation of the photorespiratory intermediates Gly, Ser, and glycerate was initially neglected (i.e., we assumed isotopic equilibrium between pools in different subcellular compartments). Reactions were classified as irreversible or in rapid isotopic equilibrium (Figure 5A; see Supplemental Methods 6 online) based on experimental knowledge about their *in vivo* reversibility (Stitt et al., 1980, 2010). To simplify the fitting procedure, RuBP labeling dynamics were used as a proxy for input to the system (see Methods) with the correction for the possibility of spawning unlabeled molecules (see Supplemental Methods 6 online) under the assumption of random label distribution in each mass isotopomer. We included Suc6P and Tre6P in the model but omitted Suc and trehalose because we could not obtain labeling information for their complete C backbone (see Supplemental Table 4 online). However, this does not affect the reliability of the model. Indeed, it means that these products are treated in the same manner as starch, for which ^{13}C enrichment data were not available.

The distribution of net fluxes in the entire network can be described as a non-negative linear combination of five flux modes (Figures 5B to 5F), which are themselves in metabolic steady state. Each mode comprises the CBC, including the C fixation by Rubisco and the pathway to one of the five out-fluxes of the system (loss of CO_2 in photorespiration and the biosynthesis of starch, Suc, trehalose, and *myo*-inositol). The CBC is included in all five flux modes because part of the fixed C is used for RuBP regeneration to maintain the steady state. The calculations require three assumptions: (1) the labeling data are obtained from a metabolic system that is in steady state (i.e., all concentrations of metabolites and fluxes are constant) (see Supplemental Table 2 online), (2) enzymes do not display isotope discrimination, and (3) the metabolic pools are well mixed (i.e., there is negligible channeling).

Application of the extended KFP method to the metabolic model provided estimates of intracellular fluxes that provide the best overall variance-weighted fit (Press et al., 2007) to the experimentally determined pool sizes and the labeling kinetics for depletion of the ^{12}C isotopomer (Figure 5; see Supplemental Table 3 and Supplemental Data Set 1 online). These reference flux estimates were benchmarked by comparing them with those expected during photosynthesis in a C_3 plant like *Arabidopsis*. Based on the substrate specificities of Rubisco, the rate of carboxylation should be fourfold higher than oxygenation (see Introduction and values in Sharkey, 1988). Also, Suc

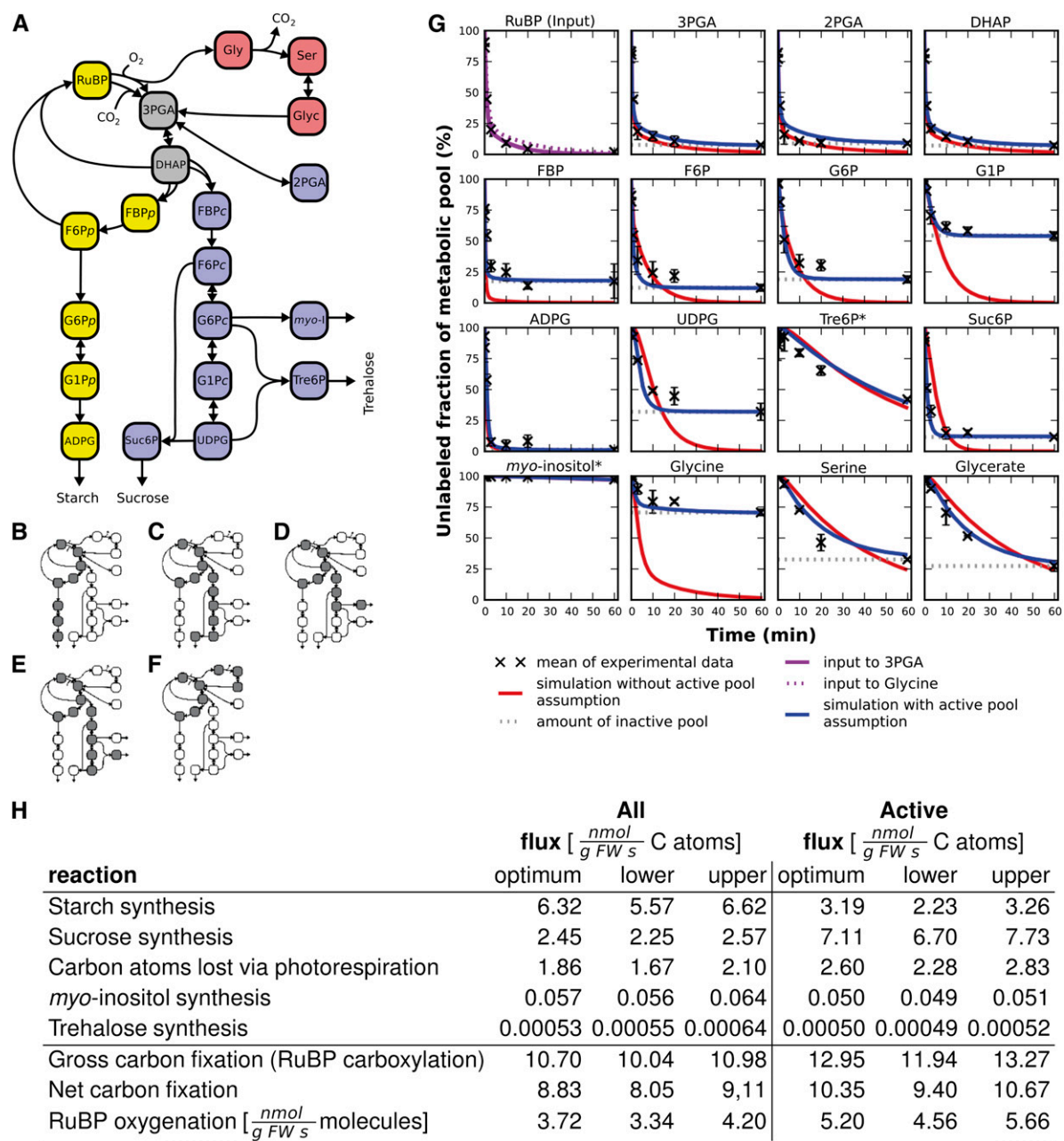


Figure 5. Pathway Model, Elementary Flux Modes, and Flux Estimates.

(A) Pathway model. The model includes the CBC, photorespiration, and Suc, starch synthesis, *myo*-inositol, and trehalose synthesis. There is explicit separation of cytosolic (blue, subscript c) and plastidic pools (yellow, subscript p) that are not equilibrated by transporters. Plastidic and cytosolic pools of 3PGA and DHAP are treated as a single pool (gray) that is in isotopic equilibrium (Stitt et al., 1983) due to rapid exchange via the triose-phosphate phosphate transporter. Metabolite pools involved in photorespiration are shown in pink. Reactions are set as irreversible (single-headed arrow) or reversible (double-headed arrow), based on experimental data (Bassham and Krause, 1969; Stitt et al., 1980).

(B) to (F) Elementary flux modes of the model: synthesis of starch **(B)**, synthesis of Suc **(C)**, synthesis of *myo*-inositol **(D)**, synthesis of trehalose **(E)**, and photorespiration **(F)**.

(G) Simulation of best fit. Measured data for the proportion of the total pool present as the ^{12}C isotopomer are shown as crosses ($\pm\text{SD}$) and the predicted decay dynamics of the ^{12}C isotopomer modeled using the unadjusted data set (red line) and after excluding the inactive pool (blue line). Gray dotted lines indicate the inactive pool. For Tre6P and *myo*-inositol (asterisks), which have a small total pool size, the active pool assumption is not applied. The RuBP panel shows the input models for the influx to the pool of 3PGA (purple solid line) and Gly (purple dotted line). The corresponding crosses indicate the data used for parameter estimation.

synthesis is approximately twofold faster than starch synthesis in *Arabidopsis* in the conditions used in our study (Gibon et al., 2009), while Tre6P synthesis is an order of 1000 slower (Lunn et al., 2006).

Modeled Fluxes

We first modeled fluxes assuming that the entire pool of each metabolite is involved in photosynthetic flux (Figure 5H, case All; full results are presented in Supplemental Tables 5 and 6 online). The value of the variance-weighted mean squared error of the best fit was much larger than one (the variance-weighted mean square error of 8035 and 12 estimated parameters), suggesting unreliable goodness of fit. The estimated rate of RuBP oxygenation was about a third of the rate of carboxylation (3.72:10.70), and the rate of starch synthesis was ~2.6 times higher than the rate of Suc synthesis (6.32:2.45). While the relation between carboxylation and oxygenation is close to expectations, the model seriously overestimates the rate of starch synthesis and underestimates the rate of Suc synthesis. The 95% confidence intervals for the estimated fluxes are given in Figure 5H; interestingly, the data enforce a small and left-skewed estimate of the trehalose synthesis rate, causing it to fall out of its confidence interval. Furthermore, the fitted curves for the washout of ^{12}C showed very poor agreement to measured data for Gly, UDPG, and G1P and relatively poor agreement for G6P, F6P, FBP, and Suc (Figure 5G, red lines). This analysis indicated that the poor performance of the model might be associated with the attempt to fit, in particular, the modeled fluxes to the experimental data for Gly, G1P, and UDPG. Significantly, the washout curve for the ^{12}C isotopomer for each of these metabolites plateaued before 60 min, and a substantial proportion of the pool that had become labeled was present as the fully labeled ^{13}C isotopomer (Figure 2; see Supplemental Figures 3 and 6 online). As already discussed, this pattern may arise due to the presence of two pools, of which only one is involved in photosynthetic metabolism.

The assumption was made that part of the total metabolite pool in the rosette does not participate in photosynthesis because it is located in the vacuole and/or nonphotosynthetic cells. The model was reimplemented after adjusting the pool sizes to only include pools that are likely to be involved in photosynthesis. In the following, this is termed “the active pool assumption.” The active pool was set as the difference between the total pool and the nominal value of the ^{12}C isotopomer after 60 min. The proportion of the metabolite that was not labeled at this time was subtracted from the ^{12}C isotopomer content at each time point (Figures 2 and 4; see Supplemental Figures 3 and 6 online) for the purpose of defining the washout kinetics

and from the total pool (Table 1) for the purpose of defining the absolute pool size. Metabolites for which this led to a major correction include Gly, G1P, and UDPG (active pool equivalent to ~25, 40, and 63% of the total pool, respectively; Figures 2 and 4). As already explained, the isotopomer labeling pattern for these metabolites is in agreement with the existence of two separate pools, rather than incomplete labeling of one pool. The active pool assumption was not applied to Tre6P and *myo*-inositol because their ^{12}C isotopomers had not reached a plateau in the time span of our experiment.

As shown in Figure 5H, case Active, the modeled flux for RuBP carboxylation (12.95 nmol g FW $^{-1}$ s $^{-1}$ RuBP) was ~2.49-fold higher than the rate of oxygenation (5.20 nmol g FW $^{-1}$ s $^{-1}$ RuBP), and the modeled rate of Suc synthesis (7.11 nmol g FW $^{-1}$ s $^{-1}$ C atoms) was ~2.2-fold higher than the rate of starch synthesis (3.19 nmol g FW $^{-1}$ s $^{-1}$ C atoms). The modeled fluxes to *myo*-inositol and to trehalose via Tre6P were very low with values of 0.05 and 0.0005 nmol g FW $^{-1}$ s $^{-1}$ C atoms, respectively. The modeled curves for washout of ^{12}C isotopomers closely matched the experimental data (Figure 5G, blue lines), leading to values for the variance-weighted mean squared error of 2145, which is fourfold smaller than in the previously examined scenario without the active pool assumption.

The goodness-of-fit value reflects the extent to which the model of photosynthetic metabolism matches the gathered data. The current relatively high values for goodness of fit are probably due to aspects of compartmentation, which are not yet accounted for in our underlying metabolic model. We chose to restrict the representation of compartmentation in the model to parameters for which experimental evidence was available and not to seek to improve fit by adding additional untested assumptions.

However, we note that the relatively high goodness of fit would not result from the choice of excluding fluxes from PEP to organic acids and amino acids due to the complexity of modeling these pathways. This might lead to unreliable flux estimates from our model if the excluded fluxes were high. We summed the ^{13}C detected at 60 min in organic acids and amino acids downstream of PEP (Figure 1B) and compared it to the summed ^{13}C found in all measured metabolites. The organic acids and amino acids accounted for only 2.6% of the total ^{13}C . This is probably an overestimate, since this comparison omits ^{13}C in starch and because some of the ^{13}C in organic acids and amino acids is incorporated by PEPc (see Discussion for flux estimates).

Estimation of Unlabeled Influx

The model still does not address the observed incomplete labeling of the CBC intermediates, many of which are thought to

Figure 5. (continued).

(H) Selected fluxes and rates for the two scenarios included that were used for benchmarking. The rates of Rubisco carboxylation and oxygenation are given as RuBP consumption (i.e., use of CO_2 or O_2 , respectively). Fluxes were estimated for two scenarios (1) All, using unadjusted ^{12}C isotopomer decay and metabolite content data sets. (2) Active, using the pool of each metabolite that is actively involved in photosynthetic fluxes. The inactive pool was nominally defined as the proportion that remains as ^{12}C isotopomer at 60 min. It was subtracted from the ^{12}C isotope kinetic (i.e., the 60-min value is set as zero). The absolute pool (Table 1) was also decreased in the same proportion. For each scenario, flux estimates are denoted by the optimal value obtained with the fit “optimum” and the “lower” and “upper” 95% confidence limits obtained from the Monte-Carlo simulation.

be unique to photosynthesis. To address this issue, we treated the C atoms of all the CBC intermediates as one well-mixed pool to which there is an unlabeled influx of C atoms and simulated the dynamics of enrichment. This is justified by the short turn-over times and near-isotopic equilibration of the intermediates (see Supplemental Figure 3B online). The labeling behavior of the CBC intermediates corresponds to that of RuBP. In this simplified model (see Supplemental Figure 7 and Supplemental Table 7 online), the labeling dynamics of this single pool is governed by five fluxes: gross fixation, net fixation (equivalent to net out-flux from the cycle), photorespiration out-flux, photorespiration influx, and an unlabeled influx (see Supplemental Figure 7A online). This model was fitted to the washout of RuBP and the enrichment of the influx to the CBC from photorespiration, described by an exponential function (see Supplemental Figures 7B and 7C online). We again used the variance-weighted mean squared error function. We note that while the influx from photorespiration to the CBC in the full flux model relied on the pool sizes of the metabolites participating in photorespiration, here, this is no longer the case as we directly used the fit to the washout dynamics of glycerate. The best fit to the experimental data for RuBP is obtained by including an additional unlabeled influx of $0.0017 \text{ nmol g FW}^{-1} \text{ s}^{-1}$ C atoms. This is equivalent to $\sim 0.02\%$ of gross C fixation (see Supplemental Figure 7F online). This indicates that the incomplete labeling kinetics of CBC intermediates can be almost fully attributed to the influx of incompletely labeled C from photorespiration (see Supplemental Figures 7D and 7E online). This simplified model also provides an estimated ratio of carboxylation to oxygenation, with the latter being approximately threefold higher. This is in good agreement with the expectation (between three and four; see above) but is somewhat higher than the prediction from the full model implemented with the active pool assumption (only 2.49-fold higher; see above).

Robustness of the Full Model to Alterations in Experimental Values

We further examined these differences in the modeled ratio of carboxylation to oxygenation by considering further modifications of the full model in which, in addition to Tre6P and *myo*-inositol, we did not apply the active pool assumption to the following: (1) the two photorespiratory intermediates glycerate and Ser and (2) glycerate, Ser, and (as an example of for many possible CBC intermediates) triose-phosphates, denoted by Active 2 and 3, respectively, in Supplemental Table 8 online. The modeled ratio of carboxylation to oxygenation rose to 3.0 in Active 2, whereas it remained fairly low (2.68) in Active 3. These results show, not unexpectedly, that the modeled fluxes are sensitive to the model used, and the experimental data values that are supplied to the model.

We also investigated the robustness of the full model to other changes in experimental values. This is an alternative approach to that of Antoniewicz et al. (2006), who established the relative importance of measurements by linking flux variances with the variances of measurements (see Discussion). Supplemental Figure 8 online shows the log-fold change of the relative difference of flux estimates with respect to the reference flux

estimates (given in Figure 5) for each changed input. Successive alterations of the PGA pool size between 50 and 125% of the reference values resulted in little change in CBC flux until PGA was decreased to 50%, with little effect on photorespiration and a shift to increased Suc synthesis at 125% PGA. In addition, there was a more pronounced decrease of the flux to starch at 50% PGA and only slight changes in flux to *myo*-inositol and photorespiration (see Supplemental Figure 8 online). Changing the pool size of ADPG to either 50 or 125% of the nominal value had little effect on CBC and photorespiration, but it resulted in an increase of flux to Suc and a decrease of flux to starch. Changes in the pool size of UDPG decreased the modeled flux through the CBC and, especially, photorespiration and also decreased starch synthesis but had little effect on the flux to Suc. Decreasing the Gly pool to 50% resulted in a decrease of all flux estimates, while decreasing it to 75 or increasing it to 125% lead to a decrease in the flux to starch and a slight increase of flux through photorespiration and to Suc. A progressive increase of the pool size of Ser from 50 to 125% of its nominal value led to a marked decrease of the modeled flux through CBC and photorespiration, with a mixture of effects on the starch and Suc synthesis. We also conducted robustness analysis to quantify the stability of the estimated flux to a simulated dramatic change in subcellular compartmentation of G6P (see Supplemental Figure 9 online). Successive alterations of the compartmentation of the G6P pool between the cytosol and chloroplast from 99:1, 80:20, 60:40, 40:60, to 1:99 resulted in only a mild decrease in flux through the CBC, negligible effects on photorespiration, an increase of fluxes to Suc, a decrease of flux to starch, and negligible effects on trehalose and *myo*-inositol synthesis.

DISCUSSION

We modeled photosynthetic fluxes by exposing the rosette of an intact *Arabidopsis* plant to $^{13}\text{CO}_2$, determining kinetic changes in isotope patterns of 40 metabolites of primary metabolism and analyzing the data using an extended KFP approach. Our approach to flux estimation differs from that used previously in plants (Rontein et al., 2002; Schwender et al., 2004a). These studies used steady state labeling to address a series of important biological questions, including the role of Rubisco in developing seeds, the regulation of oil seed metabolism, and the interaction between primary metabolism and biosynthetic pathways. However, steady state labeling is not applicable to photosynthesis because CO_2 is the only substrate, and the isotopic steady state will not provide an informative labeling pattern for the purpose of estimating fluxes. In a recent elegant study, Young et al. (2011) modified the formulation to facilitate modeling of isotopic nonstationary pools in *Synechocystis* and provide the first metabolic flux model of a photoautotroph. Their study provided a comprehensive flux map for all CBC reactions and some side reactions, including those catalyzed by Glc-6-phosphate dehydrogenase, malic enzyme, and the photorespiratory pathway. It also identified pathways that might compromise cyanobacterial productivity. We used an extension of the KFP approach, as it allowed us to estimate fluxes through photosynthetic end products and to benchmark them against

classically determined flux signatures of photosynthesis. Unlike the approach of Young et al. (2011), in which metabolic pool sizes are fitted as free parameters, we constrained the model with measured pool sizes obtained by mass spectrometry, including the use of nonaqueous fractionation, to provide information on subcellular pool sizes.

Before we discuss the model, some features of the experimental data per se should be addressed. Using *k*-means clustering analysis, we were able to demonstrate a clear temporal sequence of labeling, with CBC intermediates, ADPG, and 2PGA labeling rapidly, followed by metabolites in Suc synthesis and photorespiration, then pyruvate, Ala, and aromatic amino acids, with organic and other amino acids being labeled very slowly or even negligibly. These clusters closely reflect known pathway topologies. The labeling dynamics also fit those expected from pathway stoichiometry and pool sizes (Stitt et al., 1983; Gerhardt et al., 1987; Benson, 2002; Arrivault et al., 2009). In contrast with the situation in cyanobacteria (Young et al., 2011), the labeling kinetics of the CBC intermediates were not clearly discriminated. Labeling of all measured CBC intermediates closely followed that of 3PGA. The estimated half-lives of CBC intermediates are almost all <1 s in *Arabidopsis* leaves (Arrivault et al., 2009). Resolution of fluxes within the CBC in leaves will require even earlier harvests after introducing $^{13}\text{CO}_2$, which is hardly possible due to the time needed to exchange the CO_2 in the chamber and within the leaf or the use of conditions in which the rate of photosynthesis is far lower than that used in this study.

Our data set contain some rather unexpected features. These include (1) the slow labeling kinetics of FBP, (2) the rapid labeling kinetics of maltose, (3) the very incomplete labeling of UDPG and G1P compared with metabolites upstream (F6P and G6P) and downstream (Suc6P) of them in the pathway of Suc synthesis, (4) the very slow and incomplete labeling of many organic acids and especially the Gln 2-oxoglutarate aminotransferase (GOGAT) pathway intermediates Gln, Glu, and 2-oxoglutarate, and (5) the incomplete labeling of all pools including the CBC intermediates. Another important feature is the differential dynamics of labeling of the various pools, which raises the question as to which time scale is the most appropriate for modeling. In their study of ^{13}C labeling of tobacco plants, Hasunuma et al. (2010) reported similar labeling kinetics for many metabolites to those reported here. However, their data analysis was restricted to estimating turnover rates.

We implemented an extension to the KFP approach that allows us to estimate photosynthetic fluxes from the ^{12}C -isotopomer washout kinetics of 16 metabolites. The underlying metabolic model includes prior knowledge about pathways, the reversibility of reactions (Gerhardt et al., 1987; Arrivault et al., 2009), topology, compartmentation (Gerhardt et al., 1987; Table 1), rate of equilibration of label between compartments by the triose-phosphate transporter (Stitt et al., 1983), and experimental information about total pool sizes and their distribution between the plastid and cytosol (Table 1; see Supplemental Table 3 online). The flux estimates were benchmarked against signature flux ratios of photosynthesis previously defined by gas exchange and ^{14}C labeling. For this purpose, we used the ratio of the carboxylation and oxygenation reactions of Rubisco and ratio of the fluxes to Suc and starch. In *Arabidopsis* at ambient

CO_2 , these should be approximately (2.5 to 3):1 and 2:1, respectively (Häusler et al., 2000; Cegelski and Schaefer, 2006; Gibon et al., 2009; Bauwe et al., 2010). It should be noted that although the photorespiratory flux estimate in *Synechocystis* (Young et al., 2011) was even lower than the value cited above, this is likely to be explained by an efficient C concentrating mechanism in this species that suppresses the oxygenase reaction of Rubisco (Kaplan and Reinhold, 1999).

Flux modeling using unadjusted experimental data returned flux ratios that were far from the expected ratios. Furthermore, for many metabolites, the modeled washout kinetics showed a poor fit to the experimental data. Inspection of the full labeling kinetics of individual metabolites revealed that in many cases only part of the total metabolite pool is involved in photosynthesis. Flux modeling using pool sizes that had been corrected to consider only pools actively participating in photosynthetic metabolism gave values of 2.5:1 and 2.2:1 for the carboxylation/oxygenation ratio and the Suc/starch ratio, respectively, a good agreement between the modeled washout kinetics and the experimental data. A further flux, which modeled to trehalose via Tre6P, was very low ($0.0005 \text{ nmol g FW}^{-1} \text{ s}^{-1} \text{ C atoms}$). This corresponds to $0.15 \text{ nmol Tre6P g FW}^{-1} \text{ h}^{-1}$, which is in agreement with the synthesis rate of Tre6P measured by Lunn et al. (2006) after the addition of Suc to starved seedlings. Interestingly, realistic estimates for the carboxylation/oxygenation ratio were obtained without information about labeling of the initial photorespiratory intermediate 2-phosphoglycolate. While it will be important to extend our technical platform to include this metabolite, among others, this points to the robustness of our approach and also shows that flux estimates can be obtained using larger and more slowly labeled pools like Gly, Ser, and glycerate.

The correction of pool sizes to exclude pools that do not participate in photosynthesis is supported by the labeling kinetics and, in the case of Suc synthesis, by a comparison of the labeling kinetics of metabolites located further downstream in the pathway. Nevertheless, this analysis begs the question how active and inactive metabolite pools are discriminated. The most likely explanation is spatial compartmentation, which could occur at various levels, including cellular, subcellular, and within-organellar microcompartmentation. For Gly, Ser, glycerate, and many organic acids, nonaqueous fractionation indicated that a large part of the total pool is indeed located in the vacuole. For UDPG and G1P, we evaluated subcellular distribution and whether the pool sizes of these metabolites were different in parts of the leaf that are not photosynthetically active, namely, the venal tissues. Neither approach pinpointed the location of an inactive pool; nevertheless, two other possibilities remain. First, bioinformatic analysis of *Arabidopsis* metabolite profiles revealed patterns suggestive of microcompartmentation of metabolism within organelles (Krueger et al., 2011), as previously postulated for a pool of UDPG that is involved in cellulose synthesis (Amor et al., 1995). Secondly, recent studies in *Arabidopsis* and potato implicate the presence of as yet unidentified G1P transporters at the plastid and plasma membranes (Fettke et al., 2011). Further analyses will be required to fully understand the exact mechanisms by which the active and inactive pools of these metabolites are separated. Given the rapid advance of techniques for spatial resolution of metabolism (Aharoni and

Brandizzi, 2012), it is likely that the exact reason underlying the unexpected labeling may become apparent in future experiments.

Returning to other unexpected features of our data, the slow labeling of FBP indicates that a substantial part of the total FBP pool is not directly involved in the CBC. This is unlikely to be explained by slower labeling of a cytosolic pool because the latter is small (Table 1) and is in isotopic equilibrium with the triose-phosphates (Stitt et al., 1983). One possible explanation might be binding of FBP on Rubisco active sites (Von Caemmerer and Quick, 2004).

Another noteworthy feature is the rapid labeling of maltose. Maltose is produced during starch degradation at night (Stitt et al., 2010). However, it is unlikely that rapid labeling of maltose is a result of transient starch degradation, since the labeling is very fast, meaning that starch granules would have to be rapidly degraded in the light, which has not been observed (Zeeman et al., 2002) except under special atypical conditions (Stitt and Heldt, 1981). A more likely hypothesis is *de novo* biosynthesis of maltose in the light, possibly in the chloroplasts. Mutagenesis of AGPase to promote *in vivo* activity led to an increase in maltose levels in the light (Hädrich et al., 2012). $^{14}\text{CO}_2$ labeling studies of spinach chloroplasts detected very-short-term labeling of maltose from $^{14}\text{CO}_2$ (Linden et al., 1975; Schilling, 1982; Linden and Schilling, 1984). As this molecule was asymmetrically labeled, its formation cannot be attributed to the action of β -amylase on starch. This mechanism would also explain why the maltose is not completely labeled in our experiments.

The labeling kinetics of organic acids are extremely slow. Until recently (Zell et al., 2010), these had been considered to be minor products of photosynthesis, although net synthesis is required to provide C skeletons for amino acid synthesis. It was also surprising that GOGAT pathway intermediates like Glu and 2-oxoglutarate show very slow labeling. Fluxes through the GOGAT pathway include the refixation of ammonium released by Gly decarboxylase and are therefore of the same order as the rate of photorespiration (Foyer et al., 2009). Indeed, we estimated that <2.6% of the fixed ^{13}C moved into organic acids and amino acids that lie downstream of pyruvate, supporting the small flux through amino acids of negligible effect to the other flux estimates (see Supplemental Table 9 online).

Net synthesis of organic acids and organic acids requires an anaplerotic reaction, which is catalyzed by PEPc in plants. PEPc incorporates $^{13}\text{CO}_2$ into the C1 position of oxaloacetate. As a result of rapid equilibration with malate and fumarate, the label is rapidly randomized between the C1 and C4 positions (Tcherkez et al., 2005). This label will then be converted to other organic acids via the TCAC. It should be noted that total ^{13}C incorporation into organic acids and amino acids will therefore overestimate the flow of ^{13}C from the CBC. Pyruvate can be formed via PK or from malate via NADP- or NAD-malic enzyme or via a direct side product of Rubisco, in which pyruvate is produced at ~0.7% of the rate of 3PGA (Pearce and Andrews, 2003). It is not facile to use mass spectrometric data to discriminate between the fluxes toward organic acid and amino acid formation via PEPc, malic enzyme, the side reaction of Rubisco, PK, and pyruvate dehydrogenase. This would require site-specific labeling data, which could only be obtained by a suite of enzymatic cleavage reactions, resulting in a massive

increase in sample number and data complexity. For this reason, we did not attempt to model fluxes from the CBC to organic acids and amino acids.

One potential way to circumvent this problem in the future may be to attempt simultaneous ^{13}C and ^{15}N feeding studies. Another perhaps simpler approach would be to extend the mass spectrometry analysis platform using NMR to evaluate positional isotopomers at the atomic level (Tcherkez et al., 2011, 2012b). However, it is important to note that such analyses are currently technically restricted for two reasons. First, due to sensitivity issues, NMR experiments still require large sample sizes (Kruger et al., 2008); to perform such experiments would thus necessitate the growth of a massive number of plants and require a huge acquisition time. Second, to date, a method for efficient and rapid ^{15}N labeling of leaf material is not available. These hurdles notwithstanding, such an experiment remains an exciting future prospect, as is the extension of modeling strategies to further characterize the fluxes in these pathways.

At a qualitative level, the low level of label in GOGAT intermediates implies that 2-oxoglutarate is internally recycled, with very little *de novo* synthesis and/or is obtained from a preexisting unlabeled pool. In agreement with this notion, it has been proposed that 2-oxoglutarate is synthesized in the light from a preexisting pool of citrate (Tcherkez et al., 2012a, 2012b). More generally, the slow labeling of organic acids and amino acids derived from them is consistent with the idea that glycolysis and the TCAC are inhibited in the light, when the TCAC operates in a noncyclic manner (Tcherkez et al., 2009, 2012a; Sweetlove et al., 2010). The very low enrichment in organic acids like isocitrate, fumarate, and malate can also be explained because the vast majority of these metabolites are located in the vacuole (Table 1; Lips and Beevers, 1966a, 1966b; Steer and Beevers, 1967).

Another interesting feature of our data set is the incomplete labeling of the CBC intermediates, including metabolites that are unique to the CBC like SBP and RuBP. A similar finding was reported in a recent study in tobacco leaves (Hasunuma et al., 2010) as well as an earlier, more focused study that determined the ^{13}C labeling of the 3PGA pool in *Quercus rubra* (Delwiche and Sharkey, 1993). Incomplete labeling of CBC intermediates indicates the presence of an unlabeled influx that dilutes the $^{13}\text{CO}_2$ that is fixed by Rubisco and/or dilutes metabolic pools involved in regeneration of RuBP. Our computational analysis demonstrates that the incomplete labeling of CBC intermediates can be almost completely explained by the incomplete labeling of the C that returns to the CBC from photorespiration. It is likely that this is the result of a slow exchange of labeled C in the pools of Gly, Ser, and glycerate that are directly involved in photorespiration with pools of Gly, Ser, and glycerate that are not directly involved in photorespiration and act as a temporary reservoir of unlabeled C that is slowly introduced into the CBC (see above). A best fit of the simplified model was obtained by adding a further very small additional influx of unlabeled C, equivalent to ~0.02% of the gross fixation. This could derive from a variety of sources, including very slow degradation of starch (Weise et al., 2006) and refixation of CO_2 that is respired from unlabeled substrates in nonphotosynthetic cells in the leaf.

The simplified model yielded a slight increase in the value for the rate of carboxylation relative to oxygenation (to 3.02,

compared with 2.87 and 2.49 in the full model implemented with total pools and with active pools, respectively). The estimate from the simplified model is closest to the expected range of 3 to 4 (Sharkey, 1988; Cegelski and Schaefer, 2006), while when the full model is used, a better fit for this output, but not for other outputs, was obtained when it was implemented with total pools rather than the active pool assumption. We interpret this as indicating that these models represent approximations that do not fully represent a more complex situation, where there is probably partial label exchange between two or more pools of various intermediates. Nevertheless, the relation between the modeled rates of carboxylation and oxygenation are relatively robust against these changes in the model and experimental inputs. The same held for tests in which the levels and compartmentation of other metabolites were altered. This is an alternative approach to robustness to that used by Antoniewicz et al. (2006), who established the relative importance of measurements by linking flux variances with the variances of measurements. However, in the context of a plant leaf, which contains many cell types and subcellular compartments, sources, or errors may not be fully captured by just considering the variance of the data. It also requires consideration of the potential impact of multiple metabolite pools, which may participate to differing degrees in the flux in question.

In summary, we were able to establish an experimental setup to perform short-term $^{13}\text{CO}_2$ labeling of *Arabidopsis* rosettes, in a manner that allowed rapid quenching of metabolism, to determine the labeling kinetics of 40 metabolites of primary C metabolism and to model the major fluxes during photosynthesis via kinetic flux profiling. Implementation of an approach that discriminates between active and inactive metabolite pools and only takes the active pools into consideration returned flux ratio estimates in keeping with those canonically reported. This finding demonstrates that it is possible to use stable isotope feeding alongside mass spectrometry profiling to gain insights into the dynamics and fluxes in a metabolic system as complex as photosynthesis in a C_3 leaf. Our study also indicates the importance of information about metabolite compartmentation and suggests that its use will be a prerequisite for modeling of photosynthetic, and probably other metabolic processes, in multicellular eukaryotic tissues. Future application of the response of the metabolic network of photosynthesis to environmental or genetic perturbation will be essential to deepen our understanding of the metabolic regulation of this key process and may have implications for the improvement of crop yield and ultimately the redirection of C to high value natural products. In addition, utilization of this approach to study the even more complex photosynthesis pathways, like that exhibited in C_4 plants such as maize, may provide important enabling insights into harnessing this pathway in synthetic biology approaches to enhance the efficiency of photosynthesis of C_3 species.

METHODS

Chemicals

$^{13}\text{CO}_2$ (isotopic purity 99 atom percentage) was purchased from Campro Scientific. All other chemicals were purchased from Sigma-Aldrich, Roche, or Merck.

Plant Growth

Arabidopsis thaliana, accession Columbia-0, was grown under 8/16-h day/night cycles at an average irradiance of $120 \mu\text{mol m}^{-2} \text{s}^{-1}$, temperatures of $22/20^\circ\text{C}$, and 50% relative humidity. Plants were grown in individual 6-cm-diameter pots, with water/gas-permeable plastic foil (Aquafoil) between the rosette and the soil. Plants with fully expanded 5-week-old rosettes (stage 3.90; Boyes et al., 2001) were used for $^{13}\text{CO}_2$ feeding experiments and subcellular metabolite level determination.

$^{13}\text{CO}_2$ Feeding Experiments

The gas mixture was prepared using mass flow controllers (Brooks Instrument), one controller per gas type. Each gas type was supplied separately at a fixed flow rate and mixed in a single PVC tube, resulting to a final concentration of 78% N_2 , 21% O_2 , 400 ppm $^{13}\text{CO}_2$, and a final flow of 5 liters min^{-1} . After passing through a humidifier, the gas mixture was supplied to the inside of the transparent labeling chamber (Magenta GA-7 plant culture box), of volume 380 mL, by three transparent PVC pipes placed on the top rear of the box in such a way that the gas stream was directed to the plant rosette. These highly transparent boxes allow the transmission of 97% of the irradiance. Therefore, a photon flux density of $115 \mu\text{mol m}^{-2} \text{s}^{-1}$ (as measured in the box with a LI-250A light meter; Li-Cor) was provided by a FL-460 lighting unit from Walz. The labeling chamber was continuously washed with this mixture through the whole experiment.

Within a maximum of a few seconds, it is possible to completely remove $^{12}\text{CO}_2$ from the atmosphere in the labeling chamber and maintain this state throughout the entire experiment. To estimate the removal rate of $^{12}\text{CO}_2$, an empty labeling chamber was washed with the same gas mixture as during the experiment (flow 5 liters min^{-1}), and the $^{12}\text{CO}_2$ concentration was tracked using an infrared CO_2 gas analyzer (Li-Cor LI-800). After 3 to 5 s, the $^{12}\text{CO}_2$ concentration was negligible, approximating 0 ppm. In addition, we estimated the time of the exchange of gases in the chamber by constructing a mathematical model: Given that the volume of the chamber (V) and the gas flow (F) are known, the influx and efflux are the same, and unlabeled CO_2 is rapidly mixing with $^{13}\text{CO}_2$ inside the chamber, the time course of the $^{12}\text{CO}_2$ content inside the chamber can be described by an exponential function, whose half-life-period is given by $t_{1/2} = \ln 2 \cdot V/F$. The estimated $t_{1/2}$ for the gas in the chamber with volume of 380 mL is 3 s. In addition, we calculated the residence time (volume/flow rate) in the humidifier to be 6 s (flow rate of 5 liters min^{-1} and volume of 500 mL). Since the gas flow was constant during the entire experiment, the residence time of the humidifier should not affect the ^{12}C wash out time in the box.

The experiment was started 2 h after the onset of light in the growth chamber, and the last labeled plant was harvested 1 h before the offset of lights. Individual plants in their pot were quickly moved from the growth chamber to the labeling chamber (<5 s) and quenched 5 or 10 s and 1, 3, 10, 20, or 60 min after the start of labeling in a random manner. Three biological replicates were obtained for each labeling condition. Metabolism was quenched directly in the chamber by pouring a large volume of liquid nitrogen over the rosette through a funnel that was placed through a small outlet in the side of the box and held just above and slightly to the side of the plant in such a way as to avoid shading the rosette. All frozen plant material above the plastic foil was collected and stored at -80°C .

Determination of Metabolite Levels and Isotope Distributions

Prior to utilization, plant material was ground to a fine powder using a Retsch ball-mill. For GC-TOF-MS, the levels of all metabolites were quantified essentially as described by Roessner et al. (2001). Metabolites were extracted from 100 mg (fresh weight) of frozen plant powder, and derivatization was performed as described by Fiehn et al. (2000). The

GC-TOF-MS was run using the same settings as detailed by Lisec et al. (2006). The resulting chromatograms were processed using TagFinder software. Analytes were manually identified using the TagFinder plug-in of the TagFinder software (Luedemann et al., 2008) and the reference library mass spectra and retention indices housed in the Golm Metabolome Database (<http://gmd.mpimp-golm.mpg.de>; Kopka et al., 2005). Interpretation of gas chromatography–electron impact fragments derived in GC-TOF-MS analysis were performed based on previously published detailed EI fragmentation pattern of trimethylsilylated and methoxiaminated carbohydrates (DeJongh et al., 1969; Laine and Sweeley, 1973; MacLeod et al., 2001; Sanz et al., 2002) and amino acids (Abramson et al., 1974; Leimer et al., 1977). Furthermore, interpretation was supported by the mass shifts observed upon *in vivo* ^{13}C labeling (Huege et al., 2007). Since mass fragments comprising the full metabolite C backbone, such as M^+ (molecular ion) or $\text{M}-15^+$ (mass fragment generated by the loss of CH_3^+ group), were often mostly present at low intensities or even below their detection limit, alternative fragment ions for mass isotopomer analysis, proposed by Huege et al. (2007), were used (see Supplemental Table 4 online).

For LC-MS/MS quantification, metabolites were extracted from 15 mg (fresh weight) of frozen plant powder as described by Lunn et al. (2006) and Arrivault et al. (2009). Suc6P and Tre6P were measured as described by Lunn et al. (2006). Other measurements were performed as described previously (Arrivault et al., 2009), but mass spectrometry settings were adapted for the quantification of all isotopomers of the compounds as shown in Supplemental Table 10 online. The run was divided into four segments with dwell times of 100 ms or less, adapted to obtain a minimum of 15 scans per chromatogram. For the nucleotide sugars ADPG and UDPG, the isotopomers were restricted to labeling occurring in the hexose, but the fully labeled isotopomers were also monitored. For the partially labeled isotopomers of 2-oxoglutarate and succinate, two labeling alternatives were possible and monitored, considering the label being present in the product ion or not. For these isotopomers, signal peak areas from both alternatives were summed. In the case of 2PGA and 3PGA, which could be separated by the liquid chromatography condition used, the chromatograms obtained with the standards were of poor quality compared with the ones observed in plant extract. Consequently, quantification was not performed for these compounds, and the data presented are solely based on signal peak areas obtained in extracts. The obtained peaks were integrated using the Thermo Finnigan processing software package LCQuan-2.5.

The electron impact fragmentation of trimethylsilylated and methoxiaminated metabolite derivatives (analytes), which are observed in routine metabolite profiles using gas chromatography–mass spectrometry (GC-MS) technology (see for example Fiehn et al., 2000; Lisec et al., 2006), require thorough interpretation of gas chromatography–electron impact fragmentation patterns and knowledge concerning the sum formula of each analyzed mass fragment when using ^{13}C -isotope labeling. By contrast, the LC-MS/MS method allows the quantification of the whole C backbone of the metabolites, which is highly beneficial when calculating ^{13}C fractional enrichment. Since mass spectrometry detects ionized compounds separated by their mass-to-charge ratio, the mass-to-charge ratio of ^{13}C -labeled compounds increases by an amount that equals the number of incorporated ^{13}C atoms (see the example in Supplemental Figure 2 online). Therefore, by determining the ratio of intensity of the monoisotopic ion and its isotopic ions, the ratio of stable isotope labeling can be quantified (Hasunuma et al., 2010).

Both GC-TOF-MS and LC-MS/MS matrices were subsequently processed using the Corrector software tool (http://www-en.mpimp-golm.mpg.de/03-research/researchGroups/01-dept1/Root_Metabolism/smp/CORRECTOR/index.html). After correction, quantification of the metabolites was performed based on calibration curves obtained with authentic standards whose matrices were also corrected. Relative isotopomer

abundance (m_n) for each metabolite in which n ^{13}C atoms are incorporated is calculated in mass fragments (Wittmann and Heinzle, 1999; van Winden et al., 2002; Huege et al., 2007) from GC-MS analysis and in whole molecules from LC-MS/MS analysis by the following equation:

$$m_n (\%) = \frac{M_n}{\sum_{j=0}^n M_j} \times 100,$$

where M_n represents the isotopomer abundance for each metabolite. The ^{13}C enrichment of the metabolite possessing i C atoms is calculated as follows:

$$^{13}\text{C} \text{ enrichment } (\%) = \sum_{n=1}^i \frac{i \times m_n}{i}.$$

Removal of G1P by Enzymatic Reactions

All reactions (final reaction volume 165 μL) contained 150 μL of plant extract (corresponding to 10 mg FW material), 20 mM HEPES-KOH, pH 8, and 5 mM MgCl_2 . To remove G1P from the extracts, either 0.4 units of phosphoglucumutase, 0.7 units of glucose 6-phosphate dehydrogenase and 0.75 mM NADP, or 0.5 units of UGPase, 0.2 units of PPase, and 0.75 mM UTP were added to the reaction mixtures. Control reactions were performed as described above, but enzymes were omitted. Mixtures were incubated at 30°C for 1.5 h, heated at 100°C for 2 min, and precipitated proteins removed by centrifugation (14,000 rpm, 5 min). For LC-MS/MS measurements, 10 μL of the mixtures was analyzed.

Nonaqueous Fractionation

For determination of subcellular metabolite levels, cellular compartments were separated using density gradient centrifugation under nonaqueous condition as described in Krueger et al. (2011). Metabolites were extracted from dried fraction aliquots and quantified by GC-TOF-MS (Roessner et al., 2001) and LC-MS/MS (Lunn et al., 2006; Arrivault et al., 2009). Based on enzymatic markers, subcellular metabolite distributions were computed using the BestFit command line tool (Krueger et al., 2011).

Extended KFP and Robustness Analysis

KFP allows for determining reaction fluxes based on a mass-action-like differential equation model for the washout of the unlabeled fraction of metabolic pools, whereby

$$\frac{dx^u}{dt} = \sum_r F_{X,r}^{in} \prod_{i \in S_r} \left(\frac{x_i^u}{x_i^t} \right)^{\alpha_i} - \sum_r F_{X,r}^{out} \frac{x^u}{x^t},$$

where x^u is the unlabeled content of metabolite X , $F_{X,r}^{in}$ is the influx to metabolite X from reaction r , and $F_{X,r}^{out}$ denotes the out-flux from X . The model of central C metabolism is comprised of 30 mass-action-like differential equations, shown in Supplemental Methods 6 online. The net fluxes of each reaction can be expressed as a positive linear combination of six independent modes, which describe the way of a fixated C atom to an out-flux of the system. Since each of these out-fluxes is normalized to one C atom per second, the coefficients of the positive linear combination are the parameters to be estimated. Unlike the original KFP approach whereby local fits are conducted for each reaction in the model, we provide a global fit of the model to the experimental data. We use the time-resolved washout of the unlabeled fraction for all pools as well as nonaqueous fractionation data for the compartmentalized pools (see Supplemental Data Set 1 and Supplemental Tables 3 and 7 online). Double-exponential function is fitted to the washout kinetics of RuBP for the purpose of estimating individual fluxes (see Supplemental Table 3 online), while an exponential function with an offset is fitted to the washout kinetics of glycerate (see Supplemental Table 7 online) to estimate the unlabeled influx to explain the incomplete labeling of CBC intermediates. In the case of RuBP, the input function is corrected for the possibility of spawning unlabeled molecules (see Supplemental Methods 6 online). For compartmentalized pools, the weighted

sum according to the nonaqueous fractionation data is fitted. Simulated annealing approach, followed by quasi-Newton optimization, are used to estimate the model parameters with variance-weighted mean squared error function (see Supplemental Methods 4 online). The correspondence between the reactions and fluxes is given in Supplemental Table 8 online. For each fit, 30 repetitions are performed and the best result is reported. The estimated net flux of a reaction is given in $\frac{\text{nmol}}{\text{gFW}\cdot\text{s}}$ of C atoms entering or leaving a particular pool participating in the reaction, except for carboxylation and oxygenation, for which the unit is $\frac{\text{nmol}}{\text{gFW}\cdot\text{s}}$ RuBP. The active pool for each metabolite is given by the fraction of the pool that labeled 60 min into the experiment, termed active pool assumption. For compartmentalized pools, the weighted sum according to the nonaqueous fractionation data is fitted only to the active pool. Confidence intervals for the flux estimates are obtained from Monte Carlo sampling (see Supplemental Methods 5 online).

Supplemental Data

The following materials are available in the online version of this article.

Supplemental Figure 1. Schematic Visualization of the Chamber Used for *Arabidopsis* Rosette Labeling.

Supplemental Figure 2. Exemplary Mass Distribution of 3PGA.

Supplemental Figure 3. $^{13}\text{CO}_2$ Labeling Kinetics of Metabolites from Calvin-Benson Cycle, Starch, Sucrose, and Trehalose Biosynthesis Pathways.

Supplemental Figure 4. Removal of G1P by Enzymatic Reactions.

Supplemental Figure 5. Time Course of Mass Distribution of Maltose and Sucrose.

Supplemental Figure 6. Time Course of Mass Distribution of Sugars, Amino Acids, and Organic Acids.

Supplemental Figure 7. Simplified Model for Estimating Unlabeled Influx.

Supplemental Figure 8. Variation of Pool Sizes.

Supplemental Figure 9. Variation in Compartmentalization Data for G6P.

Supplemental Table 1. Metabolic Content of $^{13}\text{CO}_2$ -Labeled *Arabidopsis* Rosettes.

Supplemental Table 2. $^{13}\text{CO}_2$ Enrichment of Metabolites.

Supplemental Table 3. Parameters and Data Used for Flux Estimates.

Supplemental Table 4. Gas Chromatography–Electron Impact Fragmentation Patterns.

Supplemental Table 5. Reactions, Flux Notation, and Flux Estimates.

Supplemental Table 6. Reactions, Flux Notation, and Exchange Flux Estimates.

Supplemental Table 7. Parameters and Data Used for the Simplified Model.

Supplemental Table 8. Comparison of Flux Estimates Regarding the Different Model Assumption.

Supplemental Table 9. Comparison of Flux Estimates Regarding the Influence of an Additional Flux Mode toward Amino Acid Synthesis.

Supplemental Table 10. Specific Isotopomer-Dependent MS Parameters Used in Selected Reaction Monitoring.

Supplemental Methods 1. Compartmentalization and Major Pathways of Carbon Metabolism in a Photosynthetically Active Leaf.

Supplemental Methods 2. Labeling Strategies.

Supplemental Methods 3. Introduction to Extended Kinetic Flux Profiling.

Supplemental Methods 4. Optimization Fit to the Mass Spectrometric Data.

Supplemental Methods 5. Estimation of Confidence Interval by Monte Carlo Simulation.

Supplemental Methods 6. Application to Central Carbon Metabolism.

Supplemental Data Set 1. Relative Isotopomer Abundance.

ACKNOWLEDGMENTS

We thank the Max Planck Society for support. A.R.F. thanks the Deutsche Forschungsgemeinschaft for funding in the framework of the Forschergruppe PROMICS FOR1186. A.R.F., M.S., and S.A. are also supported by the European Union Collaborative Project 3to4 and the European Union FP7 collaborative project TiMet under Contract 245143. R.H. and Z.N. were also supported by GoFORSYS Project 0313924 funded by the German Federal Ministry of Science and Education. We thank Joachim Kopka and Joost van Dongen for discussions.

AUTHOR CONTRIBUTIONS

S.A. and M.Sc. conducted the experiments and analyzed the LC-MS/MS and GC-MS data, respectively. R.F. and J.L. measured Suc6P and Tre6P by LC-MS/MS. R.H. performed the in silico modeling and estimations of reaction fluxes based on data. D.V. performed nonaqueous fractionation. J.H. adapted the Corrector software for LC-MS/MS data. A.N.-N. and M.Sc. were involved in harvesting and experimental setup. T.T. conducted the clustering analysis and was involved in interpretation of results. M.St., A.R.F., and Z.N. wrote the article and were involved in the discussion of the results. All authors read, commented on, and approved the final version of the article.

Received October 31, 2012; revised January 25, 2013; accepted February 12, 2013; published February 26, 2013.

REFERENCES

- Abramson, F.P., McCaman, M.W., and McCaman, R.E. (1974). Femtomole level of analysis of biogenic amines and amino acids using functional group mass spectrometry. *Anal. Biochem.* **57**: 482–499.
- Aharoni, A., and Brandizzi, F. (2012). High-resolution measurements in plant biology. *Plant J.* **70**: 1–4.
- Amor, Y., Haigler, C.H., Johnson, S., Wainscott, M., and Delmer, D.P. (1995). A membrane-associated form of sucrose synthase and its potential role in synthesis of cellulose and callose in plants. *Proc. Natl. Acad. Sci. USA* **92**: 9353–9357.
- Andriotis, V.M., Pike, M.J., Kular, B., Rawsthorne, S., and Smith, A.M. (2010). Starch turnover in developing oilseed embryos. *New Phytol.* **187**: 791–804.
- Antoniewicz, M.R., Kelleher, J.K., and Stephanopoulos, G. (2006). Determination of confidence intervals of metabolic fluxes estimated from stable isotope measurements. *Metab. Eng.* **8**: 324–337.
- Antoniewicz, M.R., Kelleher, J.K., and Stephanopoulos, G. (2007). Elementary metabolite units (EMU): A novel framework for modeling isotopic distributions. *Metab. Eng.* **9**: 68–86.
- Arrivault, S., Guenther, M., Ivakov, A., Feil, R., Vosloh, D., van Dongen, J.T., Sulpice, R., and Stitt, M. (2009). Use of reverse-phase liquid chromatography, linked to tandem mass spectrometry,

- to profile the Calvin cycle and other metabolic intermediates in *Arabidopsis* rosettes at different carbon dioxide concentrations. *Plant J.* **59**: 826–839.
- Badger, M.R., Sharkey, T.D., and von Caemmerer, S.** (1984). The relationship between steady-state gas exchange of bean leaves and the levels of carbon-reduction-cycle intermediates. *Planta* **160**: 305–313.
- Bassham, J.A., and Krause, G.H.** (1969). Free energy changes and metabolic regulation in steady-state photosynthetic carbon reduction. *Biochim. Biophys. Acta* **189**: 207–221.
- Bauwe, H., Hagemann, M., and Fernie, A.R.** (2010). Photorespiration: Players, partners and origin. *Trends Plant Sci.* **15**: 330–336.
- Benson, A.A.** (2002). Following the path of carbon in photosynthesis: A personal story. *Photosynth. Res.* **73**: 29–49.
- Biehl, A., Richly, E., Noutsos, C., Salamini, F., and Leister, D.** (2005). Analysis of 101 nuclear transcriptomes reveals 23 distinct regulons and their relationship to metabolism, chromosomal gene distribution and co-ordination of nuclear and plastid gene expression. *Gene* **344**: 33–41.
- Birkemeyer, C., Luedemann, A., Wagner, C., Erban, A., and Kopka, J.** (2005). Metabolome analysis: The potential of in vivo labeling with stable isotopes for metabolite profiling. *Trends Biotechnol.* **23**: 28–33.
- Blank, L.M., and Sauer, U.** (2004). TCA cycle activity in *Saccharomyces cerevisiae* is a function of the environmentally determined specific growth and glucose uptake rates. *Microbiology* **150**: 1085–1093.
- Boyes, D.C., Zayed, A.M., Ascenzi, R., McCaskill, A.J., Hoffman, N.E., Davis, K.R., and Görlach, J.** (2001). Growth stage-based phenotypic analysis of *Arabidopsis*: A model for high throughput functional genomics in plants. *Plant Cell* **13**: 1499–1510.
- Calvin, M.** (1956). The photosynthetic carbon cycle. *J. Chem. Soc.* 1895–1915.
- Cegelski, L., and Schaefer, J.** (2006). NMR determination of photorespiration in intact leaves using in vivo $^{13}\text{CO}_2$ labeling. *J. Magn. Reson.* **178**: 1–10.
- Cruz, J.A., Emery, C., Wüst, M., Kramer, D.M., and Lange, B.M.** (2008). Metabolite profiling of Calvin cycle intermediates by HPLC-MS using mixed-mode stationary phases. *Plant J.* **55**: 1047–1060.
- DeJongh, D.C., Radford, T., Hribar, J.D., Hanessia, S., Bieber, M., Dawson, G., and Sweeley, C.C.** (1969). Analysis of trimethylsilyl derivatives of carbohydrates by gas chromatography and mass spectrometry. *J. Am. Chem. Soc.* **91**: 1728–1740.
- DellaPenna, D., and Last, R.L.** (2008). Genome-enabled approaches shed new light on plant metabolism. *Science* **320**: 479–481.
- Delwiche, C.F., and Sharkey, T.D.** (1993). Rapid appearance of C-13 in biogenic isoprene when (Co2)-C-13 is fed to intact leaves. *Plant Cell Environ.* **16**: 587–591.
- Eisenreich, W., and Bacher, A.** (2007). Advances of high-resolution NMR techniques in the structural and metabolic analysis of plant biochemistry. *Phytochemistry* **68**: 2799–2815.
- Fettke, J., Malinova, I., Albrecht, T., Hejazi, M., and Steup, M.** (2011). Glucose-1-phosphate transport into protoplasts and chloroplasts from leaves of *Arabidopsis*. *Plant Physiol.* **155**: 1723–1734.
- Fiehn, O., Kopka, J., Dörmann, P., Altmann, T., Trethewey, R.N., and Willmitzer, L.** (2000). Metabolite profiling for plant functional genomics. *Nat. Biotechnol.* **18**: 1157–1161.
- Foyer, C.H., Bloom, A.J., Queval, G., and Noctor, G.** (2009). Photorespiratory metabolism: Genes, mutants, energetics, and redox signaling. *Annu. Rev. Plant Biol.* **60**: 455–484.
- Gauthier, P.P., Bligny, R., Gout, E., Mahé, A., Nogués, S., Hodges, M., and Tcherkez, G.G.** (2010). In folio isotopic tracing demonstrates that nitrogen assimilation into glutamate is mostly independent from current CO₂ assimilation in illuminated leaves of *Brassica napus*. *New Phytol.* **185**: 988–999.
- Gerhardt, R., Stitt, M., and Heldt, H.W.** (1987). Subcellular metabolite levels in spinach leaves: Regulation of sucrose synthesis during diurnal alterations in photosynthetic partitioning. *Plant Physiol.* **83**: 399–407.
- Gibon, Y., Bläsing, O.E., Palacios-Rojas, N., Pankovic, D., Hendriks, J.H.M., Fisahn, J., Höhne, M., Günther, M., and Stitt, M.** (2004). Adjustment of diurnal starch turnover to short days: Depletion of sugar during the night leads to a temporary inhibition of carbohydrate utilization, accumulation of sugars and post-translational activation of ADP-glucose pyrophosphorylase in the following light period. *Plant J.* **39**: 847–862.
- Gibon, Y., Pyl, E.T., Sulpice, R., Lunn, J.E., Höhne, M., Günther, M., and Stitt, M.** (2009). Adjustment of growth, starch turnover, protein content and central metabolism to a decrease of the carbon supply when *Arabidopsis* is grown in very short photoperiods. *Plant Cell Environ.* **32**: 859–874.
- Hädrich, N., Hendriks, J.H., Kötting, O., Arrivault, S., Feil, R., Zeeman, S.C., Gibon, Y., Schulze, W.X., Stitt, M., and Lunn, J.E.** (2012). Mutagenesis of cysteine 81 prevents dimerization of the APS1 subunit of ADP-glucose pyrophosphorylase and alters diurnal starch turnover in *Arabidopsis thaliana* leaves. *Plant J.* **70**: 231–242.
- Hasunuma, T., Harada, K., Miyazawa, S.I., Kondo, A., Fukusaki, E., and Miyake, C.** (2010). Metabolic turnover analysis by a combination of in vivo ^{13}C -labelling from $^{13}\text{CO}_2$ and metabolic profiling with CE-MS/MS reveals rate-limiting steps of the C₃ photosynthetic pathway in *Nicotiana tabacum* leaves. *J. Exp. Bot.* **61**: 1041–1051.
- Häusler, R.E., Schlieben, N.H., and Flügge, U.I.** (2000). Control of carbon partitioning and photosynthesis by the triose phosphate/phosphate translocator in transgenic tobacco plants (*Nicotiana tabacum*). II. Assessment of control coefficients of the triose phosphate/phosphate translocator. *Planta* **210**: 383–390.
- Haverkorn van Rijsewijk, B.R., Nanchen, A., Nallet, S., Kleijn, R.J., and Sauer, U.** (2011). Large-scale ^{13}C -flux analysis reveals distinct transcriptional control of respiratory and fermentative metabolism in *Escherichia coli*. *Mol. Syst. Biol.* **7**: 477.
- Hibberd, J.M., and Covshoff, S.** (2010). The regulation of gene expression required for C4 photosynthesis. *Annu. Rev. Plant Biol.* **61**: 181–207.
- Huege, J., Goetze, J., Schwarz, D., Bauwe, H., Hagemann, M., and Kopka, J.** (2011). Modulation of the major paths of carbon in photorespiratory mutants of synechocystis. *PLoS ONE* **6**: e16278.
- Huege, J., Sulpice, R., Gibon, Y., Lisec, J., Koehl, K., and Kopka, J.** (2007). GC-EL-TOF-MS analysis of in vivo carbon-partitioning into soluble metabolite pools of higher plants by monitoring isotope dilution after $^{13}\text{CO}_2$ labelling. *Phytochemistry* **68**: 2258–2272.
- Ito, O., and Mitsumori, F.** (1992). Transformation and translocation of photoassimilated (Co2)-C-13 and glycine-2-C-13 in sunflower leaves detected by C-13-NMR. *Soil Sci. Plant Nutr.* **38**: 347–360.
- Jensen, R.G., and Bassham, J.A.** (1966). Photosynthesis by isolated chloroplasts. *Proc. Natl. Acad. Sci. USA* **56**: 1095–1101.
- Kaplan, A., and Reinhold, L.** (1999). CO₂ concentrating mechanisms in photosynthetic microorganisms. *Annu. Rev. Plant Physiol. Plant Mol. Biol.* **50**: 539–570.
- King, R.W., Wardlaw, I.F., and Evans, L.T.** (1967). Effect of assimilate utilization on photosynthetic rate in wheat. *Planta* **77**: 261–276.
- Kopka, J., et al.** (2005). GMD@CSB.DB: The Golm Metabolome Database. *Bioinformatics* **21**: 1635–1638.
- Krueger, S., Gialvalisco, P., Krall, L., Steinhauser, M.C., Büssis, D., Usadel, B., Flügge, U.I., Fernie, A.R., Willmitzer, L., and Steinhauser, D.** (2011). A topological map of the compartmentalized *Arabidopsis thaliana* leaf metabolome. *PLoS ONE* **6**: e17806.

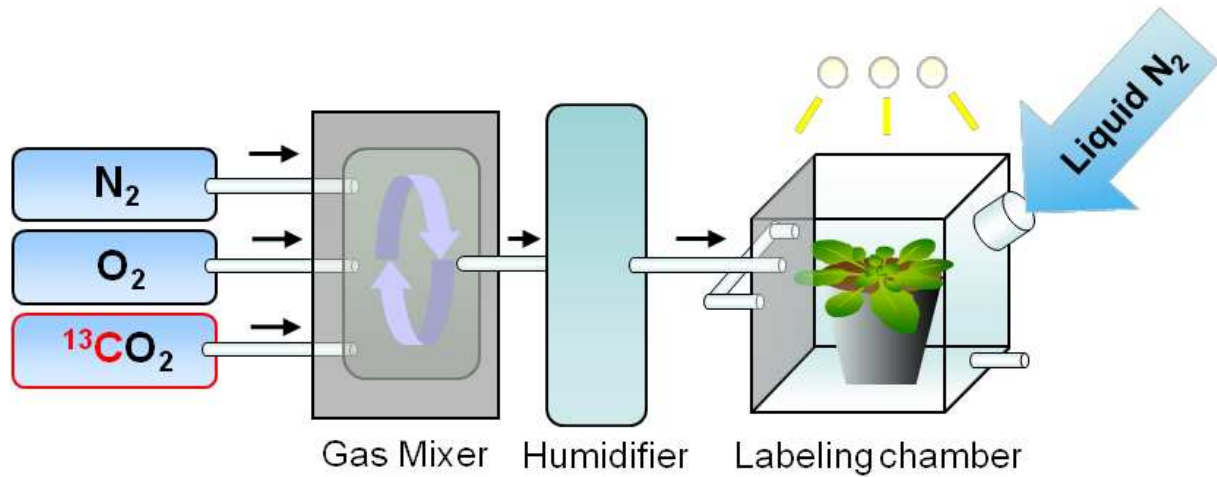
- Kruger, N.J., Troncoso-Ponce, M.A., and Ratcliffe, R.G. (2008). ^1H NMR metabolite fingerprinting and metabolomic analysis of perchloric acid extracts from plant tissues. *Nat. Protoc.* **3**: 1001–1012.
- Laine, R.A., and Sweeley, C.C. (1973). O-methyl oximes of sugars - Analysis as O-trimethylsilyl derivatives by gas-liquid chromatography and mass-spectrometry. *Carbohydr. Res.* **27**: 199–213.
- Leimer, K.R., Rice, R.H., and Gehrke, C.W. (1977). Complete mass spectra of N-trifluoroacetyl-n-butyl esters of amino acids. *J. Chromatogr. A* **141**: 121–144.
- Linden, J.C., and Schilling, N. (1984). De novo maltotriose biosynthesis from the reducing end by *Spinacia oleracea* L. chloroplasts. *Plant Physiol.* **74**: 795–799.
- Linden, J.C., Schilling, N., Brackenhofer, H., and Kandler, O. (1975). Asymmetric labelling of maltose during photosynthesis in $^{14}\text{CO}_2$. *Plant Physiol.* **76**: 176–181.
- Lips, S.H., and Beevers, H. (1966a). Compartmentation of organic acids in corn roots I. Differential labeling of 2 malate pools. *Plant Physiol.* **41**: 709–712.
- Lips, S.H., and Beevers, H. (1966b). Compartmentation of organic acids in corn roots II. The cytoplasmic pool of malic acid. *Plant Physiol.* **41**: 713–717.
- Lisec, J., Schauer, N., Kopka, J., Willmitzer, L., and Fernie, A.R. (2006). Gas chromatography mass spectrometry-based metabolite profiling in plants. *Nat. Protoc.* **1**: 387–396.
- Luedemann, A., Strassburg, K., Erban, A., and Kopka, J. (2008). TagFinder for the quantitative analysis of gas chromatography—mass spectrometry (GC-MS)-based metabolite profiling experiments. *Bioinformatics* **24**: 732–737.
- Lunn, J.E., Feil, R., Hendriks, J.H., Gibon, Y., Morcuende, R., Osuna, D., Scheible, W.R., Carillo, P., Hajirezaei, M.R., and Stitt, M. (2006). Sugar-induced increases in trehalose 6-phosphate are correlated with redox activation of ADPglucose pyrophosphorylase and higher rates of starch synthesis in *Arabidopsis thaliana*. *Biochem. J.* **397**: 139–148.
- MacLeod, J.K., Flanagan, I.L., Williams, J.F., and Collins, J.G. (2001). Mass spectrometric studies of the path of carbon in photosynthesis: positional isotopic analysis of (^{13}C) -labelled C(4) to C(7) sugar phosphates. *J. Mass Spectrom.* **36**: 500–508.
- Mardia, K.V., Kent, J.T., and Bibby, J.M. (1979). *Multivariate Analysis*. (London: Academic Press).
- Nunes-Nesi, A., Carrari, F., Lytovchenko, A., Smith, A.M.O., Loureiro, M.E., Ratcliffe, R.G., Sweetlove, L.J., and Fernie, A.R. (2005). Enhanced photosynthetic performance and growth as a consequence of decreasing mitochondrial malate dehydrogenase activity in transgenic tomato plants. *Plant Physiol.* **137**: 611–622.
- Pearce, F.G., and Andrews, T.J. (2003). The relationship between side reactions and slow inhibition of ribulose-bisphosphate carboxylase revealed by a loop 6 mutant of the tobacco enzyme. *J. Biol. Chem.* **278**: 32526–32536.
- Piques, M., Schulze, W.X., Höhne, M., Usadel, B., Gibon, Y., Rohwer, J., and Stitt, M. (2009). Ribosome and transcript copy numbers, polysome occupancy and enzyme dynamics in *Arabidopsis*. *Mol. Syst. Biol.* **5**: 314.
- Press, W.P., Vetterling, S.A., and Teukolsky, S.A. (2007). *Numerical Recipes: The Art of Scientific Computing*, 3rd ed (Cambridge, UK: Cambridge University Press).
- Quick, W.P., Schurr, U., Scheibe, R., Schulze, E.-D., Rodermeil, S. R., Bogorad, L., and Stitt, M. (1991). Decreased Rubisco in tobacco transformed with 'antisense' rbcS. I. Impact on photosynthesis in ambient growth conditions. *Planta* **183**: 542–554.
- Ratcliffe, R.G., and Shachar-Hill, Y. (2006). Measuring multiple fluxes through plant metabolic networks. *Plant J.* **45**: 490–511.
- Riens, B., Lohaus, G., Heineke, D., and Heldt, H.W. (1991). Amino acid and sucrose content determined in the cytosolic, chloroplastic, and vacuolar compartments and in the phloem sap of spinach leaves. *Plant Physiol.* **97**: 227–233.
- Römisch-Margl, W., et al. (2007). $^{13}\text{CO}_2$ as a universal metabolic tracer in isotopologue perturbation experiments. *Phytochemistry* **68**: 2273–2289.
- Roessner, U., Luedemann, A., Brust, D., Fiehn, O., Linke, T., Willmitzer, L., and Fernie, A.R. (2001). Metabolic profiling allows comprehensive phenotyping of genetically or environmentally modified plant systems. *Plant Cell* **13**: 11–29.
- Roessner-Tunali, U., Liu, J., Leisse, A., Balbo, I., Perez-Melis, A., Willmitzer, L., and Fernie, A.R. (2004). Kinetics of labelling of organic and amino acids in potato tubers by gas chromatography-mass spectrometry following incubation in (^{13}C) labelled isotopes. *Plant J.* **39**: 668–679.
- Rontein, D., Dieuaide-Noubhani, M., Dufourc, E.J., Raymond, P., and Rolin, D. (2002). The metabolic architecture of plant cells. Stability of central metabolism and flexibility of anabolic pathways during the growth cycle of tomato cells. *J. Biol. Chem.* **277**: 43948–43960.
- Saito, K., and Matsuda, F. (2010). Metabolomics for functional genomics, systems biology, and biotechnology. *Annu. Rev. Plant Biol.* **61**: 463–489.
- Sanz, M.L., Sanz, J., and Martinez-Castro, I. (2002). Characterization of O-trimethylsilyl oximes of disaccharides by gas chromatography-mass spectrometry. *Chromatographia* **56**: 617–622.
- Schaefer, J., Kier, L.D., and Stejskal, E.O. (1980). Characterization of photorespiration in intact leaves using carbon dioxide labeling. *Plant Physiol.* **65**: 254–259.
- Schilling, N. (1982). Characterization of maltose biosynthesis from alpha-D-glucose-1-phosphate in *Spinacia oleracea* L. *Planta* **154**: 87–93.
- Schwender, J., Goffman, F., Ohlrogge, J.B., and Shachar-Hill, Y. (2004b). Rubisco without the Calvin cycle improves the carbon efficiency of developing green seeds. *Nature* **432**: 779–782.
- Schwender, J., Ohlrogge, J., and Shachar-Hill, Y. (2004a). Understanding flux in plant metabolic networks. *Curr. Opin. Plant Biol.* **7**: 309–317.
- Schwender, J., Shachar-Hill, Y., and Ohlrogge, J.B. (2006). Mitochondrial metabolism in developing embryos of *Brassica napus*. *J. Biol. Chem.* **281**: 34040–34047.
- Sharkey, T.D. (1988). Estimating the rate of photorespiration in leaves. *Physiol. Plant.* **78**: 147–152.
- Sriram, G., Fulton, D.B., Iyer, V.V., Peterson, J.M., Zhou, R., Westgate, M.E., Spalding, M.H., and Shanks, J.V. (2004). Quantification of compartmented metabolic fluxes in developing soybean embryos by employing biosynthetically directed fractional (^{13}C) labeling, two-dimensional $[(^{13}\text{C}), (^1\text{H})]$ nuclear magnetic resonance, and comprehensive isotopomer balancing. *Plant Physiol.* **136**: 3043–3057.
- Steer, B.T., and Beevers, H. (1967). Compartmentation of organic acids in corn roots. III. Utilization of exogenously supplied acids. *Plant Physiol.* **42**: 1197–1201.
- Stitt, M., and Heldt, H.W. (1981). Physiological rates of starch breakdown in isolated intact spinach chloroplasts. *Plant Physiol.* **68**: 755–761.
- Stitt, M., Lunn, J., and Usadel, B. (2010). *Arabidopsis* and primary photosynthetic metabolism - More than the icing on the cake. *Plant J.* **61**: 1067–1091.
- Stitt, M., and Rees, T.A. (1980). Carbohydrate breakdown by chloroplasts of *Pisum sativum*. *Biochim. Biophys. Acta* **627**: 131–143.
- Stitt, M., Wirtz, W., and Heldt, H.W. (1980). Metabolite levels during induction in the chloroplast and extrachloroplast compartments of spinach protoplasts. *Biochim. Biophys. Acta* **593**: 85–102.

- Stitt, M., Wirtz, W., and Heldt, H.W.** (1983). Regulation of sucrose synthesis by cytoplasmic fructosebiphosphatase and sucrose phosphate synthase during photosynthesis in varying light and carbon-dioxide. *Plant Physiol.* **72**: 767–774.
- Sulpice, R., et al.** (2010). Network analysis of enzyme activities and metabolite levels and their relationship to biomass in a large panel of *Arabidopsis* accessions. *Plant Cell* **22**: 2872–2893.
- Suzuki, Y., Fujimori, T., Kanno, K., Sasaki, A., Ohashi, Y., and Makino, A.** (2012). Metabolome analysis of photosynthesis and the related primary metabolites in the leaves of transgenic rice plants with increased or decreased Rubisco content. *Plant Cell Environ.* **35**: 1369–1379.
- Sweetlove, L.J., Beard, K.F.M., Nunes-Nesi, A., Fernie, A.R., and Ratcliffe, R.G.** (2010). Not just a circle: Flux modes in the plant TCA cycle. *Trends Plant Sci.* **15**: 462–470.
- Tcherkez, G., Boex-Fontvieille, E., Mahé, A., and Hodges, M.** (2012a). Respiratory carbon fluxes in leaves. *Curr. Opin. Plant Biol.* **15**: 308–314.
- Tcherkez, G., Cornic, G., Bligny, R., Gout, E., and Ghashghaie, J.** (2005). In vivo respiratory metabolism of illuminated leaves. *Plant Physiol.* **138**: 1596–1606.
- Tcherkez, G., Mahé, A., Boex-Fontvieille, E., Gout, E., Guérard, F., and Bligny, R.** (2011). Experimental evidence of phosphoenolpyruvate resynthesis from pyruvate in illuminated leaves. *Plant Physiol.* **157**: 86–95.
- Tcherkez, G., Mahé, A., Gauthier, P., Mauve, C., Gout, E., Bligny, R., Cornic, G., and Hodges, M.** (2009). In folio respiratory fluxomics revealed by ¹³C isotopic labeling and H/D isotope effects highlight the noncyclic nature of the tricarboxylic acid “cycle” in illuminated leaves. *Plant Physiol.* **151**: 620–630.
- Tcherkez, G., Mahé, A., Guérard, F., Boex-Fontvieille, E.R., Gout, E., Lamothe, M., Barbour, M.M., and Bligny, R.** (2012b). Short-term effects of CO₂ and O₂ on citrate metabolism in illuminated leaves. *Plant Cell Environ.* **35**: 2208–2220.
- Timm, S., Nunes-Nesi, A., Pärnik, T., Morgenthal, K., Wienkoop, S., Keerbergh, O., Weckwerth, W., Kleczkowski, L.A., Fernie, A.R., and Bauwe, H.** (2008). A cytosolic pathway for the conversion of hydroxypyruvate to glycerate during photorespiration in *Arabidopsis*. *Plant Cell* **20**: 2848–2859.
- van Winden, W.A., Wittmann, C., Heinzle, E., and Heijnen, J.J.** (2002). Correcting mass isotopomer distributions for naturally occurring isotopes. *Biotechnol. Bioeng.* **80**: 477–479.
- Von Caemmerer, S., and Quick, W.P.** (2004). RubisCO: Physiology in vivo. In *Advances in Photosynthesis*. R.C. Leegood, T.D. Sharkey, and S. Von Caemmerer, eds (Dordrecht, The Netherlands: Kluwer), pp. 85–113.
- Weiner, H., and Heldt, H.W.** (1992). Inter- and intracellular distribution of amino acids and other metabolites in maize (*Zea mays* L.) leaves. *Planta* **187**: 242–246.
- Weise, S.E., Schrader, S.M., Kleinbeck, K.R., and Sharkey, T.D.** (2006). Carbon balance and circadian regulation of hydrolytic and phosphorolytic breakdown of transitory starch. *Plant Physiol.* **141**: 879–886.
- Williams, T.C., Poolman, M.G., Howden, A.J., Schwarzlander, M., Fell, D.A., Ratcliffe, R.G., and Sweetlove, L.J.** (2010). A genome-scale metabolic model accurately predicts fluxes in central carbon metabolism under stress conditions. *Plant Physiol.* **154**: 311–323.
- Winter, H., Robinson, D., and Heldt, H.** (1994). Subcellular volumes and metabolite concentrations in spinach leaves. *Planta* **193**: 530–535.
- Winter, H., Robinson, D.G., and Heldt, H.W.** (1993). Subcellular volumes and metabolite concentrations in barley leaves. *Planta* **191**: 180–190.
- Wittmann, C., and Heinzle, E.** (1999). Mass spectrometry for metabolic flux analysis. *Biotechnol. Bioeng.* **62**: 739–750.
- Young, J.D., Shastri, A.A., Stephanopoulos, G., and Morgan, J.A.** (2011). Mapping photoautotrophic metabolism with isotopically nonstationary (¹³C) flux analysis. *Metab. Eng.* **13**: 656–665.
- Young, J.D., Walther, J.L., Antoniewicz, M.R., Yoo, H., and Stephanopoulos, G.** (2008). An elementary metabolite unit (EMU) based method of isotopically nonstationary flux analysis. *Biotechnol. Bioeng.* **99**: 686–699.
- Yuan, J., Bennett, B.D., and Rabinowitz, J.D.** (2008). Kinetic flux profiling for quantitation of cellular metabolic fluxes. *Nat. Protoc.* **3**: 1328–1340.
- Yuan, J., Fowler, W.U., Kimball, E., Lu, W., and Rabinowitz, J.D.** (2006). Kinetic flux profiling of nitrogen assimilation in *Escherichia coli*. *Nat. Chem. Biol.* **2**: 529–530.
- Zeeman, S.C., Tiessen, A., Pilling, E., Kato, K.L., Donald, A.M., and Smith, A.M.** (2002). Starch synthesis in *Arabidopsis*. Granule synthesis, composition, and structure. *Plant Physiol.* **129**: 516–529.
- Zell, M.B., Fahnenstich, H., Maier, A., Saigo, M., Voznesenskaya, E.V., Edwards, G.E., Andreo, C., Schleifenbaum, F., Zell, C., Drincovich, M.F., and Maurino, V.G.** (2010). Analysis of *Arabidopsis* with highly reduced levels of malate and fumarate sheds light on the role of these organic acids as storage carbon molecules. *Plant Physiol.* **152**: 1251–1262.

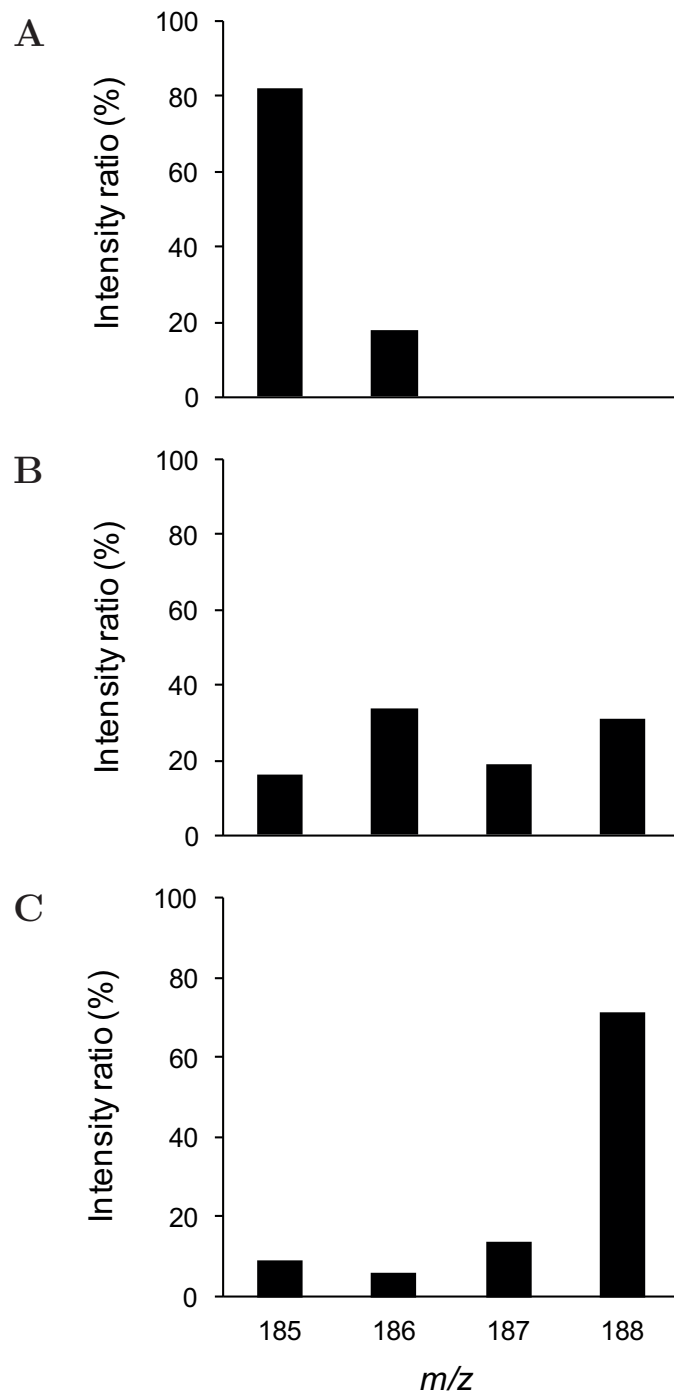
Table of Contents

Supplemental Figure 1. Schematic visualization of the chamber used for Arabidopsis rosette labeling	2
Supplemental Figure 2. Exemplary mass distribution of 3PGA	3
Supplemental Figure 3. $^{13}\text{CO}_2$ labeling kinetics of metabolites from Calvin-Benson cycle, starch and sucrose bio-synthesis pathways	4
Supplemental Figure 4. Removal of G1P by enzymatic reactions	5
Supplemental Figure 5. Time course of mass distribution of maltose and sucrose . .	6
Supplemental Figure 6. Time course of mass distribution of sugars, amino acids and organic acids	7
Supplemental Figure 7. Simplified model for estimating unlabeled in-flux	8
Supplemental Figure 8. Variation of pool size	9
Supplemental Figure 9. Variation in compartmentalization data for G6P	10
Supplemental Table 1. Metabolic content of $^{13}\text{CO}_2$ labeled Arabidopsis rosettes . .	11
Supplemental Table 2. $^{13}\text{CO}_2$ enrichment of metabolites	12
Supplemental Table 3. Parameter and data used for flux estimates	13
Supplemental Table 4. Gas chromatography-electron impact fragmentation patterns	14
Supplemental Table 5. Reactions, flux notation, and net flux estimates	15
Supplemental Table 6. Reactions, flux notation, and exchange flux estimates	16
Supplemental Table 7. Parameter and data used for the simplified model	17
Supplemental Table 8. Comparison of flux estimates regarding different model assumptions	18
Supplemental Table 9. Comparison of flux estimates regarding the influence of an additional flux mode towards amino acid synthesis.	19
Supplemental Table 10. Specific isotopomer-dependent MS parameters used in selected reaction monitoring	20
Supplemental Methods 1. Compartmentalization and major pathways of carbon metabolism in a photo-synthetically active leaf	21
Supplemental Methods 2. Labeling Strategies	21
Supplemental Methods 3. Extended Kinetic Flux Profiling	22
Supplemental Methods 4. Optimization - Fit to the mass-spectrometric data	31
Supplemental Methods 5. Estimation of confidence intervals from Monte Carlo simulation	31
Supplemental Methods 6. Application to Central Carbon Metabolism	32
Supplemental References	42

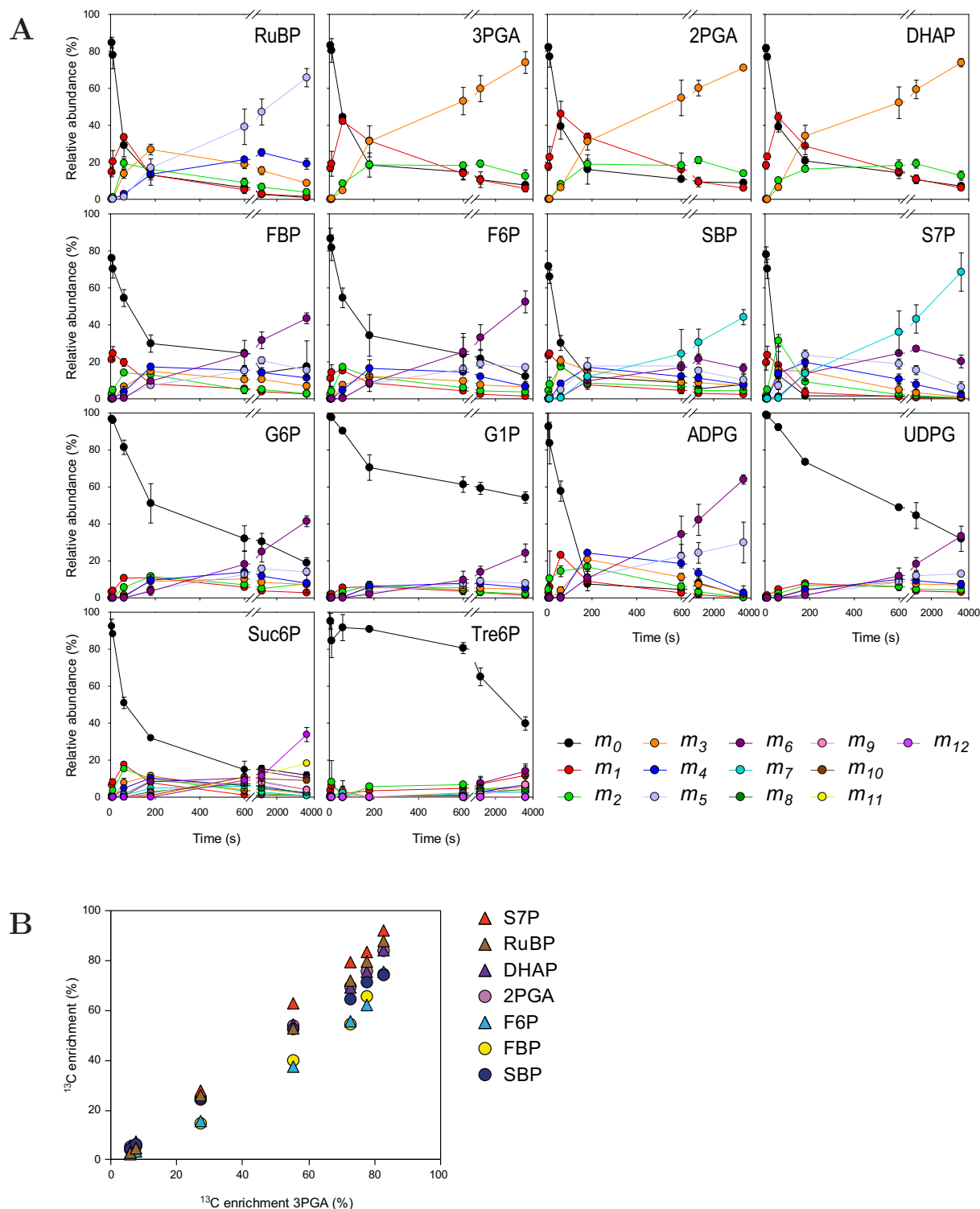
Supplemental Figures



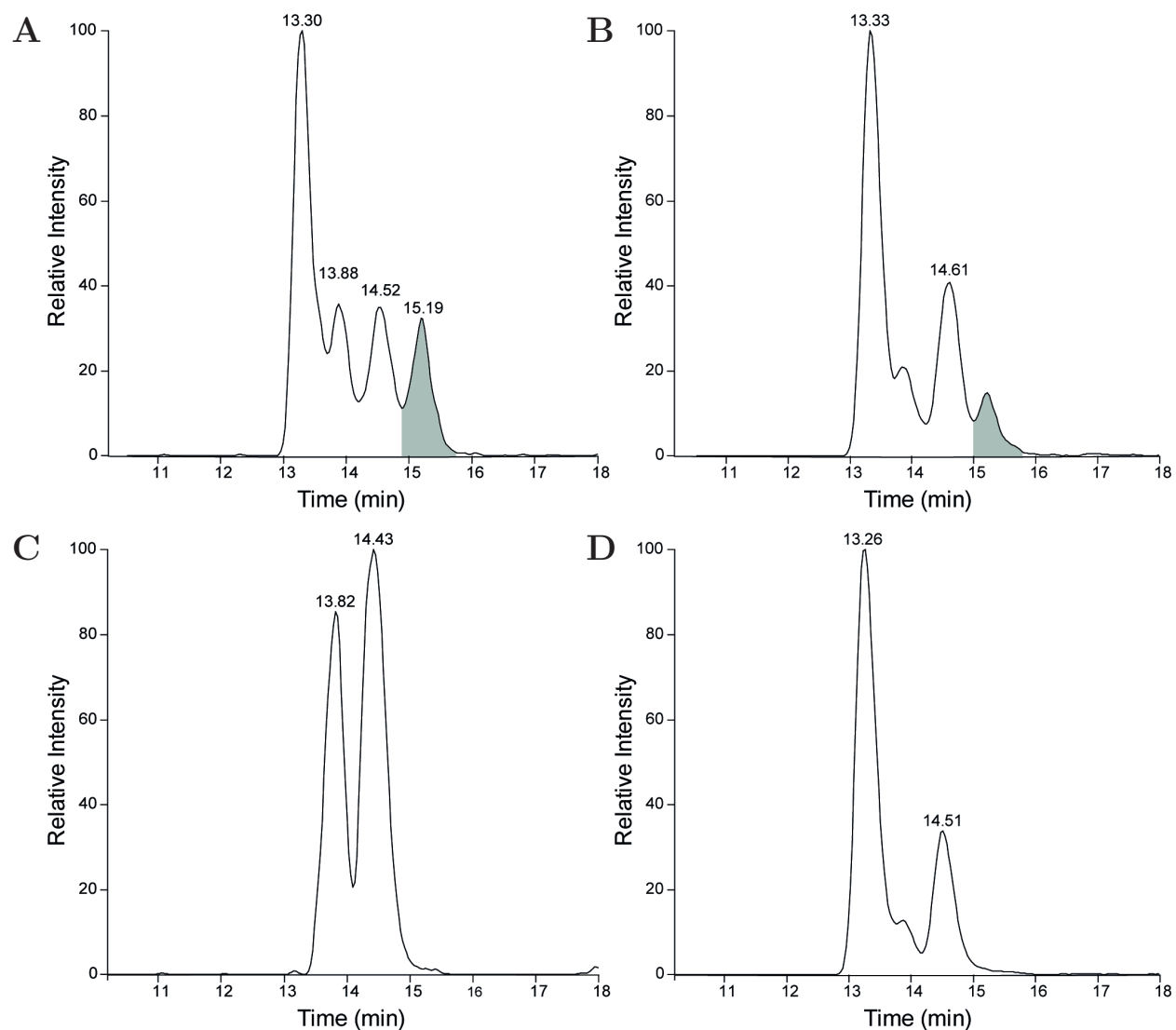
Supplemental Figure 1: Schematic visualization of the chamber used for *Arabidopsis* rosette labeling. The transparent labeling chamber was continuously washed by stream of air (5 L sec^{-1}) prepared from cylinders, containing pure N_2 , O_2 and $^{13}\text{CO}_2$ after mixture in a gas mixer, to a final concentration of 78% N_2 , 21% O_2 and 400 ppm of $^{13}\text{CO}_2$. After passing through an humidifier, gas was supplied to the inside of the chamber by three transparent PVC pipes placed on the top rear of the box in the way the gas stream is directed to the plant rosette. In the labeling chamber, plants were subjected to a photon flux density of $115 \mu\text{mol m}^{-2} \text{ min}^{-1}$ and quenched 5 s, 10 s, 1 min, 3 min, 10 min, 20 min or 60 min after start of labeling. A large volume of liquid nitrogen was poured over the rosette through a funnel that was placed through a small outlet in the side of the box and held just above and slightly to the side of the plant.



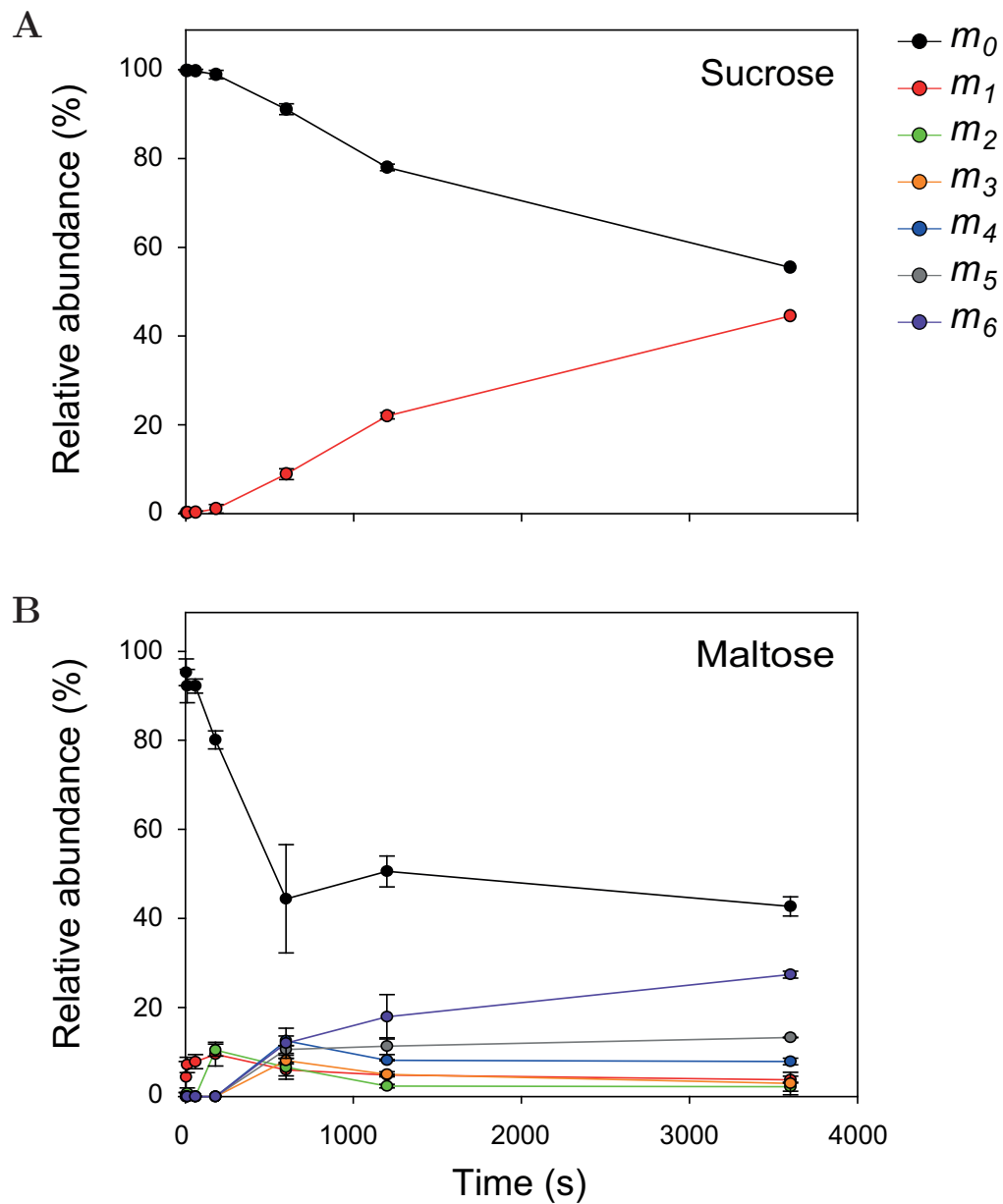
Supplemental Figure 2: Exemplary mass distribution of 3PGA. Mass distribution at 5 s (**A**), 3 min (**B**), and 60 min (**C**) after start of ^{13}C labeling using $^{13}\text{CO}_2$. The isotopomer with mass to charge ratio (m/z) 185 corresponds to the non-labeled form of 3PGA (3-phosphoglyceric acid), an analyte containing three carbons. The mass is increasing by an amount equal to the number of stable isotopes incorporated. Each isotopomer is presented as a ratio of its abundance to the sum of abundance of all isotopomers.



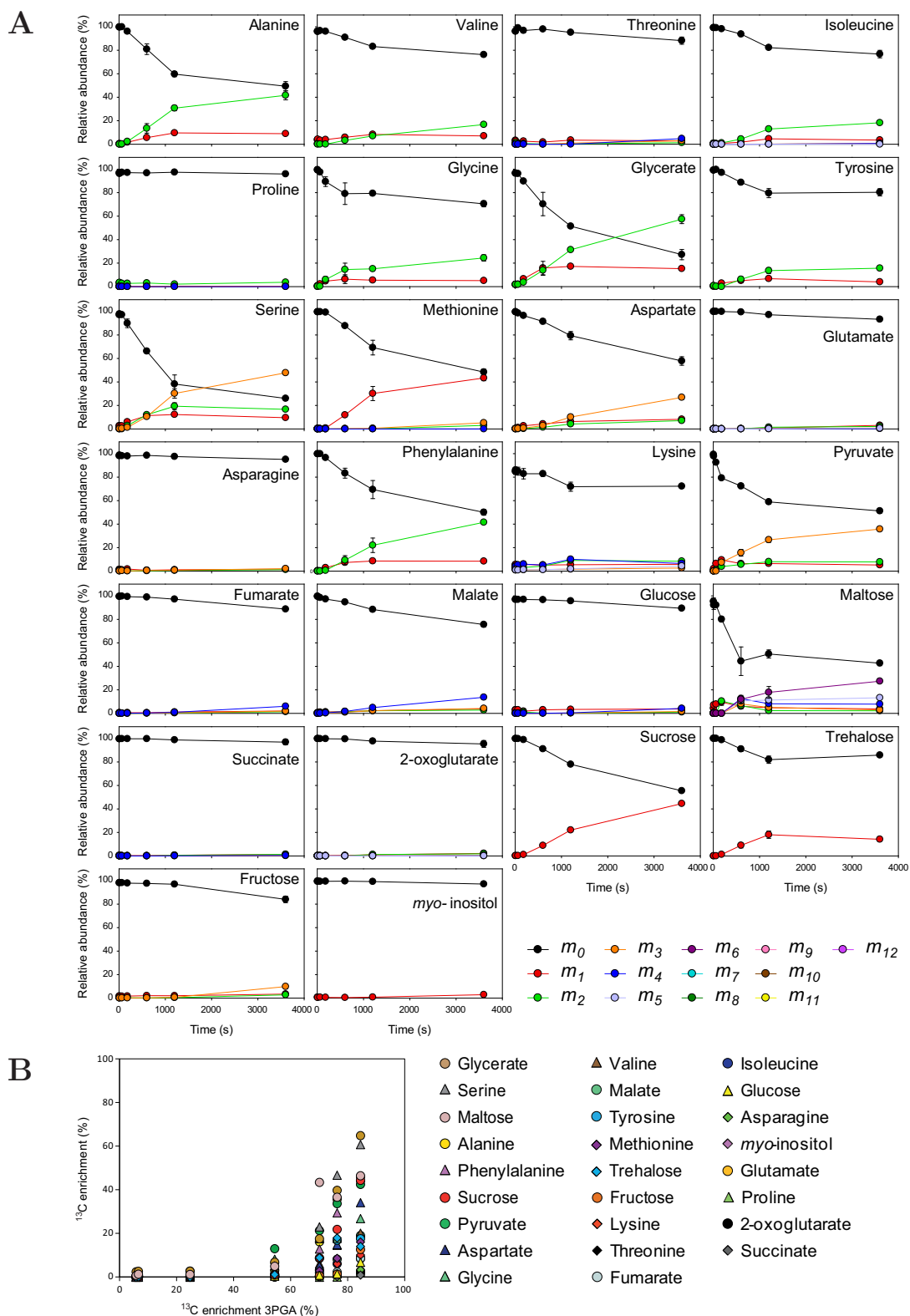
Supplemental Figure 3: $^{13}\text{CO}_2$ labeling kinetics of metabolites from Calvin-Benson cycle, starch, sucrose and trehalose bio-synthesis pathways. (A) Data as in Figure 2A of the main text, but a split x -axis is used to allow clearer visualization of early time points. **(B)** Correlation plot between $^{13}\text{CO}_2$ enrichment of Calvin-Benson cycle intermediates and that of 3PGA. Values (%) are average of three biological replicates, \pm SD. For clarity SD are not shown in panel B.



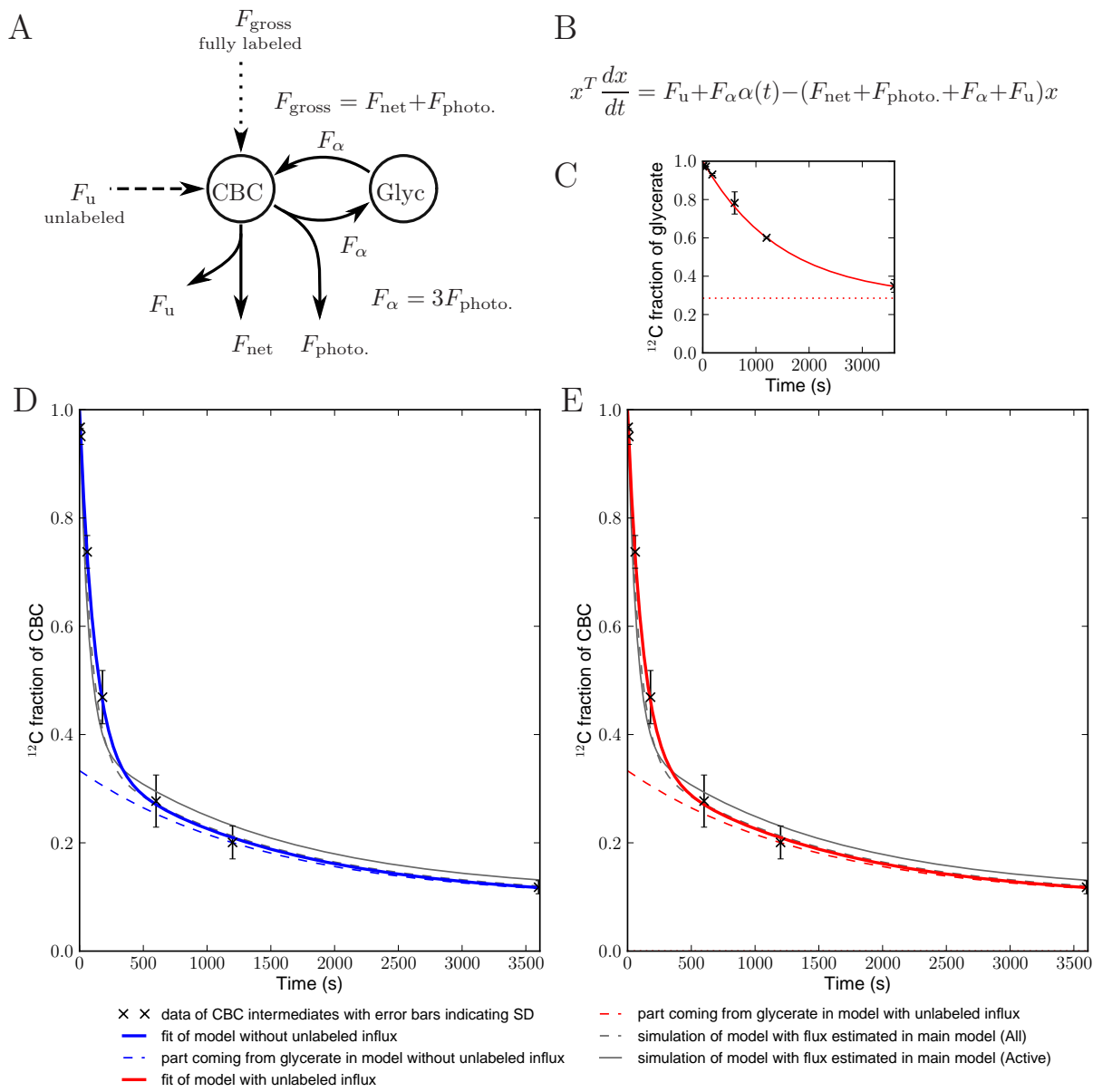
Supplemental Figure 4: Removal of G1P by enzymatic reactions. Hexose phosphate chromatograms from extracts of Arabidopsis labeled 20 min. **(A-B)** Extracts from 2 different plants, untreated with enzymes. The compounds shown, by increasing order of retention time, are G6P, an unknown hexose phosphate, F6P and G1P (marked in gray). **(C)** Extract shown in (A) pre-incubated with phosphoglucosyltransferase; **(D)** Extract shown in (B) pre-incubated with UGPase. Each of these enzyme reactions having G1P as substrate was coupled with a second enzymatic reaction to avoid an equilibrium of G1P (G6PDH and PPase for phosphoglucosyltransferase and UGPase, respectively), leading in (B) to complete removal of G6P. In (B-C), the signal attributed to G1P was not present.



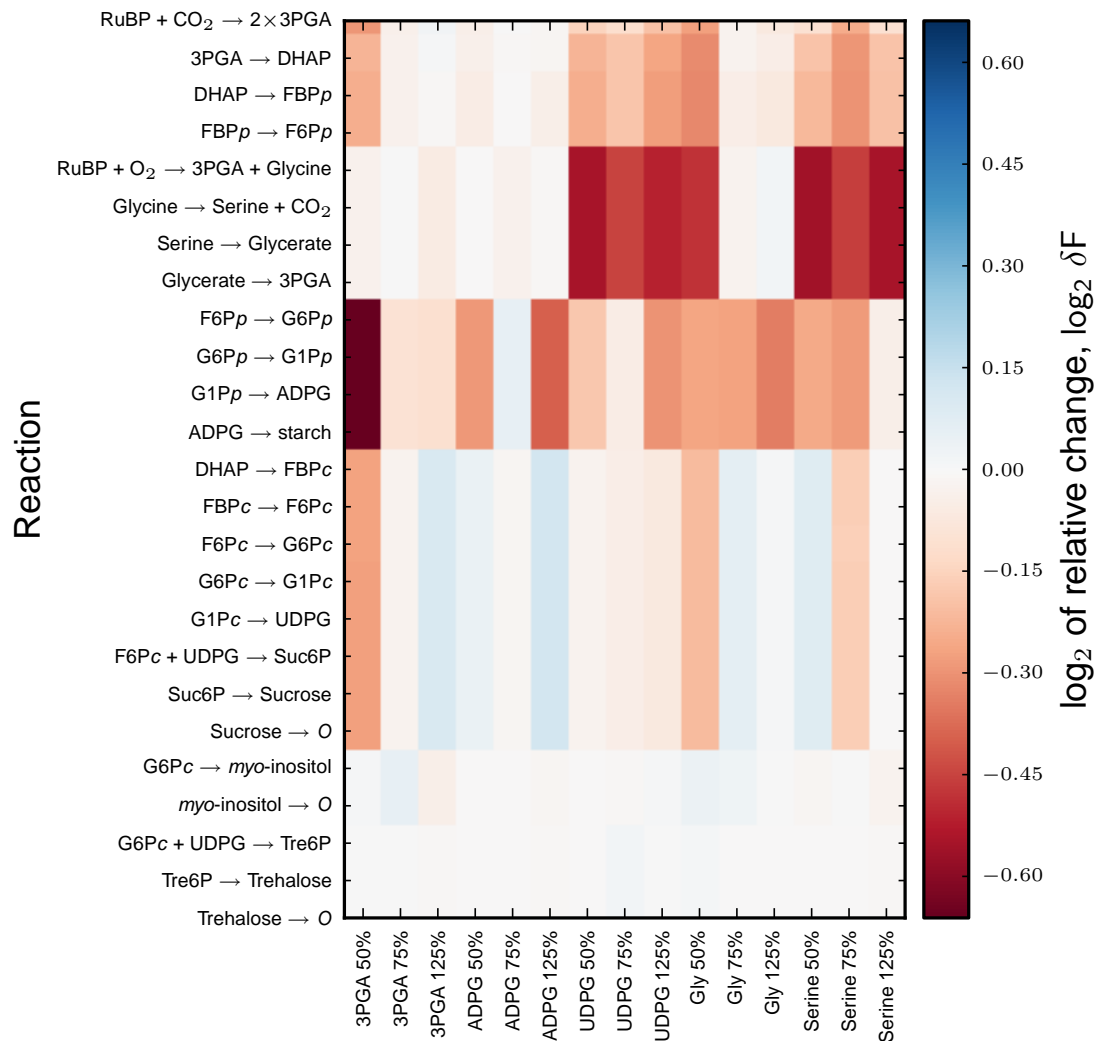
Supplemental Figure 5: Time course of mass distribution of maltose and sucrose. (A) Sucrose. **(B)** Maltose. The relative abundance of each isotopomer (m_n) for a given metabolite is represented. n corresponds to the number of ^{13}C atoms incorporated in the metabolite. Values (%) are average of three biological replicates, \pm SD.



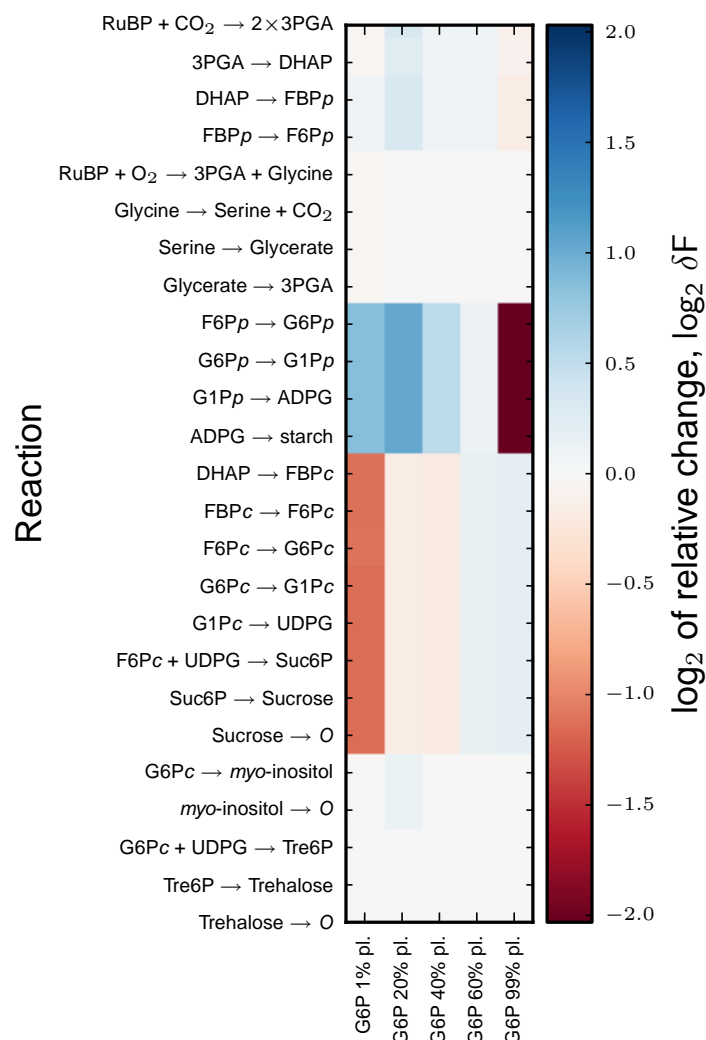
Supplemental Figure 6: Time course of mass distribution of sugars, amino acids and organic acids. (A) Time-course distribution. The relative abundance of each isotopomer (m_n) for a given metabolite is represented. n corresponds to the number of ^{13}C atoms incorporated in the metabolite. **(B)** Correlation plot between ^{13}C enrichment of sugars, amino acids, organic acids and that of 3PGA. Values (%) are average of three biological replicates, \pm SD. For clarity SD are not shown in panel B.



Supplemental Figure 7: Simplified model for estimating unlabeled in-flux. (A) Schematic representation of the simplified model. CBC denotes the pool whose labeling behavior corresponds to behavior of RuBP. The model includes five fluxes: the gross fixation in-flux, F_{gross} , net fixation out-flux, F_{net} , photorespiration out-flux, $F_{\text{photo.}}$, the in-flux from glycerate, F_α , and the unlabeled in-flux, F_u , which is to be estimated. (B) Differential equation whose solution gives the dynamics of the wash-out of the CBC pool. (C) The data for the wash-out of glycerate is used for fitting $\alpha(t) = Ce^{-ct} + (1 - C)$, which is an exponential function with offset. Panels (D) and (E) depict the model fits with and without unlabeled in-flux, shown in blue and red bold lines, respectively. For comparison, the fit with flux estimates from the main model for the cases with and without the active pool assumption are also included. (F) Tabular representation of the numerical results depicted in panels (D) and (E). The flux estimates are denoted by the optimal value obtained from the fit 'opt' and the 'lower' and 'upper' 95% confidence limits obtained from the Monte Carlo simulation. The parameter and pool sizes used for estimating fluxes are shown in Supplemental Table 7.



Supplemental Figure 8: Variation of pool size. The effect of varying the pool size of a metabolite on the estimates of individual net fluxes is visualized with the help of heatmaps. The figure refers to the 'Active' scenario. Each column corresponds to a change in the pool size of a particular metabolites. Variations in the pool size of 3PGA, ADPG, UDPG, serine, and glycine to 50, 75, and 125% of the nominal value, shown in **Supplemental Table 3**, are considered. Effect is quantified by \log_2 of the relative change in flux: $\delta F = \frac{F}{F^{\text{ref}}}$. The reference flux F^{ref} is shown in **Supplemental Table 5** ('Active', opt.).



Supplemental Figure 9: Variation in compartmentalization data for G6P. The effect of varying the compartmentalization data for G6P on the estimates of individual net fluxes is visualized with the help of heatmaps. The figure refers to the 'Active' scenario. Each column corresponds to a unique variation in the compartmentalization of G6P. Variations in the distribution data of G6P to 40, 60, and 80% of the nominal value in plastid (17%), shown in **Supplemental Table 3**, are considered. Effect is quantified by \log_2 of the relative change in flux: $\delta F = \frac{F}{F^{\text{ref.}}}$. The reference flux $F^{\text{ref.}}$ is shown in **Supplemental Table 5** ('Active', opt.).

Supplemental Tables

Compounds	$\frac{nmol}{g\ FW}$	5s/10s	10s/60s	60s/180s	180s/600s	600s/1200s	1200s/3600s
2PGA	n.d.	n.d.	n.d.	n.d.	n.d.	n.d.	n.d.
3PGA	n.d.	n.d.	n.d.	n.d.	n.d.	n.d.	n.d.
ADPG	0.71 \pm 0.29	0.271	0.034	0.275	0.194	0.431	0.278
DHAP	15.9 \pm 5.5	0.947	0.950	0.119	0.738	0.137	0.751
F6P	129 \pm 26	0.705	0.640	0.091	0.493	0.141	0.370
FBP	21.2 \pm 9.6	0.622	0.347	0.144	0.816	0.153	0.542
G1P	18.9 \pm 6.1	0.931	0.538	0.212	0.440	0.578	0.630
G6P	213 \pm 50	0.783	0.650	0.104	0.552	0.205	0.393
RuBP	84.6 \pm 23.4	0.283	0.139	0.195	0.720	0.057	0.884
S7P	65.3 \pm 13.0	0.405	0.907	0.918	0.843	0.131	0.342
SBP	16.3 \pm 4.9	0.975	0.995	0.368	0.522	0.234	0.623
UDPG	92.6 \pm 19.5	0.129	0.748	0.071	0.794	0.393	0.265
Tre6P	0.16 \pm 0.03	0.609	0.712	n.d.	n.d.	0.515	0.466
Suc6P	0.82 \pm 0.36	0.555	0.488	n.d.	n.d.	0.004	0.009
Glycine	532 \pm 205	0.460	0.052	0.885	0.786	0.272	0.358
Glycerate	17.3 \pm 4.5	0.066	0.394	0.159	0.259	0.311	0.799
Serine	1000 \pm 195	0.863	0.624	0.921	0.926	0.305	0.326
myo-inositol	153 \pm 19	0.478	0.401	0.473	0.465	0.424	0.424
Sucrose	1114 \pm 117	0.411	0.215	0.341	0.709	0.424	0.422
Trehalose	2.86 \pm 0.86	0.135	0.402	0.043	0.004	0.420	0.420
Glutamate	1278 \pm 230	0.394	0.784	0.007	0.581	0.180	0.565
Malate	761 \pm 270	0.428	0.674	0.480	0.622	0.379	0.921
2-oxoglutarate	47.9 \pm 19.7	0.742	0.934	0.273	0.520	0.419	0.758
Alanine	325 \pm 85	0.213	0.200	0.613	0.472	0.525	0.692
Pyruvate	24.1 \pm 5.2	0.293	0.461	0.721	0.601	0.430	0.334
Valine	51.9 \pm 8.1	0.985	0.569	0.287	0.095	0.435	0.392
Isoleucine	12.5 \pm 2.4	0.858	0.753	0.582	0.238	0.429	0.429
Proline	131 \pm 63	0.634	0.790	0.073	0.689	0.378	0.597
Threonine	180 \pm 39	0.541	0.395	0.821	0.499	0.503	0.193
Fumarate	108 \pm 54	0.179	0.605	0.962	0.800	0.422	0.432
Aspartate	35.1 \pm 5.0	0.430	0.373	0.670	0.596	0.423	0.505
Phenylalanine	18.3 \pm 5.6	0.984	0.671	0.662	0.604	0.427	0.419
Asparagine	114 \pm 31	0.822	0.498	0.514	0.296	0.429	0.420
Fructose	1058 \pm 237	0.933	0.062	0.574	0.604	0.422	0.421
Glucose	1859 \pm 88	0.133	0.136	0.339	0.869	0.422	0.422
Tyrosine	1.98 \pm 0.47	0.531	0.819	0.638	0.369	0.429	0.425
Succinate	27.6 \pm 15.4	0.659	0.675	0.372	0.461	0.983	0.947
Lysine	15.0 \pm 2.4	0.957	0.686	0.205	0.302	0.429	0.427
Maltose	13.9 \pm 16.4	0.385	0.876	0.209	0.022	0.417	0.418

Supplemental Table 1: Metabolic content of $^{13}\text{CO}_2$ labeled Arabidopsis rosettes. For a given compound, amounts of all isotopomers were summed. Values are average of 21 biological replicates, \pm SD, with the exception of Tre6P and Suc6P for which are average of 19 biological replicates. Student's t-Tests (two tailed; heteroscedastic) were performed on metabolite levels at subsequent labeling durations (e.g., 5 s versus 10 s). Significant differences are indicated in bold (p -value < 0.05). As indicated in Materials and Methods, quantification was not performed for 3PGA and 2PGA. n.d. stands for not determined.

Compounds	5 s	10 s	60 s	180 s	600 s	1200 s	3600 s
2PGA	5.9±0.7	7.6±1.9	27.1±2.2	55.1±6.6	72.4±4.5	77.3±3.2	82.4±1.2
3PGA	5.6±0.6	6.4±2.2	24.5±1.3	54.2±7.1	69.9±6.0	76.1±5.9	84.3±3.0
ADPG	2.0±2.3	4.5±4.4	11.3±2.2	53.5±6.6	73.6±5.7	74.8±8.3	91.6±2.3
DHAP	6.1±0.6	7.7±0.5	27.9±1.7	54.7±5.0	69.5±5.3	75.8±3.3	84.5±0.1
F6P	2.6±1.1	3.7±1.6	15.9±2.6	37.7±9.9	55.9±10.7	62.5±6.6	75.8±4.2
FBP	4.5±0.2	5.7±1.1	15.0±2.1	40.3±1.1	54.8±3.8	66.0±4.0	74.9±2.7
G1P	0.4±0.1	0.5±0.1	2.6±0.4	14.6±5.0	26.1±5.7	30.8±3.4	37.7±4.2
G6P	0.5±0.2	0.7±0.3	4.9±1.2	23.6±6.9	46.5±8.1	52.4±5.8	65.0±1.5
RuBP	3.2±0.7	4.9±1.8	26.3±3.7	53.1±7.0	72.3±5.9	79.9±3.7	88.2±1.7
S7P	3.3±0.9	5.1±0.9	28.1±9.0	63.2±6.0	79.7±6.4	83.8±4.2	92.4±3.7
SBP	4.8±0.2	6.6±1.0	25.1±3.6	52.9±4.8	64.9±8.0	71.7±4.7	74.5±6.0
UDPG	0.2±0.2	0.3±0.2	2.0±0.4	11.6±0.9	33.0±2.5	40.4±5.6	54.5±4.2
Tre6P	0.6±0.5	1.9±1.8	1.0±1.7	2.9	1.7±1.1	12.5±3.8	20.8±8.1
Suc6P	0.7±0.4	1.3±0.2	9.3±1.2	9.8	54.9±7.6	55.4±5.2	71.3±2.1
Glycine	0.3±0.4	0.6±0.5	1.4±0.1	8.3±3.3	17.7±7.3	17.9±1.6	27.0±2.6
Glycerate	2.5±0.1	2.7±0.9	2.8±0.2	6.9±0.6	17.7±7.1	40.0±0.6	65.1±4
Serine	0.2±0.1	0.1±0.1	0.4±0.2	5.2±2.0	23.2±0.6	46.9±5.2	61.0±1.3
<i>myo</i> -inositol	0.7±0.1	0.4±0.3	0.7±0.4	0.6±0.3	0.4±0.0	0.8±0.0	2.9±0.1
Sucrose	0.2±0.1	0.2±0.1	0.2±0.1	1.1±0.3	8.9±1.0	22±1.0	44.6±0.7
Trehalose	0.0±0.0	0.1±0.2	0.0±0.0	1.2±1.3	9.0±2.2	18.1±3.1	14.2±1.6
Glutamate	0.1±0.0	0.1±0.1	0.1±0.0	0.1±0.0	0.4±0.1	1.4±28.1	2.9±0.6
Malate	0.1±0.0	0.1±0.1	0.5±0.3	1.3±0.2	3.3±0.8	8.3±1.0	19.2±1.8
2-oxoglutarate	0.0±0.1	0.1±0.1	0.1±0.1	0.2±0.2	0.1±0.1	0.9±0.5	1.8±1.0
Alanine	0.0±0.1	0.2±0.2	0.0±0.0	3.1±0.3	16.3±4.3	35.9±1.7	46.1±3.9
Pyruvate	0.2±0.1	0.7±0.1	2.8±0.5	13.1±0.6	21.4±2.2	33.8±1.6	42.7±1.7
Valine	2.1±0.5	2.1±0.2	1.7±0.3	2.0±0.1	6.1±1.3	10.5±4.8	20.3±1
Isoleucine	0.2±0.2	0.2±0.2	0.3±0.1	0.6±0.1	2.2±0.8	6.2±1.1	8.6±1.1
Proline	0.0±0.0	1.3±1.2	0.0±0.0	0.6±1.0	0.0±0.0	0.1±0.2	2.0±0.3
Threonine	1.1±0.5	0.7±0.6	0.2±0.3	0.8±0.7	0.5±0.2	1.1±0.3	9.6±0.5
Fumarate	0.1±0.0	0.1±0.1	0.0±0.1	0.1±0.1	0.3±0.4	2.4±1.2	8.6±0.9
Aspartate	0.1±0.1	0.0±0.0	0.4±0.2	1.7±0.3	5.2±1.3	15±3.1	34.3±2.8
Phenylalanine	0.1±0.2	0.1±0.2	0.1±0.1	2.0±0.7	13.0±4.0	29.6±10.5	45.7±1.9
Asparagine	0.9±0.2	0.5±0.5	1.0±0.7	0.8±0.6	0.7±0.5	1.5±22.5	3.4±0.8
Fructose	0.6±0.2	0.6±0.2	0.6±0.1	0.7±0.2	0.7±0.1	1.5±0.2	12.8±2.1
Glucose	0.8±0.1	0.8±0.1	0.8±0.0	0.5±0.5	1.0±0.1	1.6±0.0	6.9±0.7
Tyrosine	0.6±0.5	0.8±1.5	0.3±0.4	1.4±0.9	8.7±1.6	17.0±6.1	17.7±2.5
Succinate	0.1±0.0	0.1±0.1	0.1±0.1	0.1±0.0	0.1±0.0	0.5±0.3	1.5±1.2
Lysine	0.4±0.7	0.3±0.3	0.5±0.5	0.6±0.5	1.6±1.3	6.2±1.1	10.2±1.4
Maltose	0.9±0.4	1.4±0.6	1.3±0.3	5.1±0.4	43.6±13	36.8±6.2	46.7±0.9
Methionine	0.1±0.1	0.1±0.2	0.1±0.1	0.2±0.1	3.0±0.4	8.7±2	16.2±1.1

Supplemental Table 2: $^{13}\text{CO}_2$ enrichment (%) of metabolites. Duration of labeling is indicated in seconds. Values are average of three biological replicates, \pm SD, except at time point 180s for Tre6P and Suc6P.

Input model											
$h_{3\text{PGA,oxy.}}^{\text{input}}(t) = Ae^{-at} + Be^{-bt}$, with A+B=1				A=0.7690, B=0.2310, a=0.0200s ⁻¹ , b=0.0014s ⁻¹							
$h_{\text{gly,oxy.}}^{\text{input}}(t) = Ae^{-at} + Be^{-bt}$, with A+B=1				A=0.7615, B=0.2385, a=0.0133s ⁻¹ , b=0.0008s ⁻¹							
Pool size data											
metabolite	measured pool size ($\frac{nmol}{qFW}$)	All				Active					
		η (%)	pool size x^T ($\frac{nmol}{qFW}$ C atoms)			$\eta_{\text{act.}}$ (%)	$\eta_{\text{inact.}}$ (%)	$x_{\text{act.}}^T$ ($\frac{nmol}{qFW}$ C atoms)		$x_{\text{inact.}}^T$ ($\frac{nmol}{qFW}$ C atoms)	
3PGA [‡]	200.10	-	600.30			93	7	558.28		42.02	
DHAP [‡]	15.88	-	47.64			93	7	44.30		3.33	
ADPG	0.55	-	3.3			99	1	3.27		0.03	
UDPG	35.75	-	214.50			68	32	145.86		68.64	
Suc6P	0.82	-	9.84			88	12	8.66		1.18	
Tre6P*	0.16	-	1.92			100	0	1.92		-	
myo-Inositol*	921.58	-	5529.48			100	0	5529.48		-	
Glycine	543.15	-	1086.30			30	70	325.89		760.41	
Serine	4264.63	-	12793.89			67	33	8571.91		4221.98	
Glycerate	168.82	-	506.46			73	27	369.72		136.74	
2PGA	20.01	-	60.03			91	9	54.63		5.40	
		$\eta_{\text{pl.}}$	$\eta_{\text{cyt.}}$	$x_{\text{pl.}}^T$	$x_{\text{cyt.}}^T$	$\eta_{\text{pl.}}$	$\eta_{\text{cyt.}}$	$\eta_{\text{inact.}}$	$x_{\text{act.pl.}}^T$	$x_{\text{act.cyt.}}^T$	$x_{\text{inact.}}^T$
FBP [†]	8.93	70	30	37.51	16.07	58	25	18	31.08	13.40	9.64
F6P [†]	86.36	34	66	176.17	341.99	30	58	12	155.45	300.53	62.18
G6P [†]	172.91	17	83	176.37	861.09	14	67	19	145.24	695.10	197.12
G1P [†]	11.68	8	92	5.61	64.47	4	42	54	2.80	29.43	37.84

Supplemental Table 3: Parameter and data used for flux estimates. The estimates for the four parameters of the double-exponential function, used as input models, are included. The data for the measured pool sizes and their compartmentalization into metabolic pools for the cases with and without the active pool assumption are given in the columns titled 'Active' and 'All', respectively. Metabolites marked by [†] occur in plastid and cytosol. Metabolic pools of 3PGA and DHAP, marked by [‡], occur in plastid and cytosol, but are assumed to be in rapid equilibrium. For metabolites marked by *, an inactive pool was not assumed.

Compounds	Ion mass (m/z)	Full-labeled ion mass (m/z)	Backbone C atoms	Ion sum formula
Phenylalanine 2TMS	218	220	2	C ₈ H ₂₀ N ₁ Si ₂
Asparagine 3TMS	231	234	3	C ₉ H ₂₃ O ₁ N ₂ Si ₂
Lysine 3TMS	156	161	5	C ₇ H ₁₄ O ₁ N ₁ Si ₁
Serine 3TMS	218	220	2	C ₁₁ H ₂₈ O ₃ N ₁ Si ₃
Threonine 3TMS	320	324	4	C ₁₂ H ₃₀ O ₃ N ₁ Si ₃
Isoleucine 2TMS	158	163	5	C ₈ H ₂₀ N ₁ Si ₁
Alanine 3TMS	188	190	2	C ₈ H ₂₂ N ₁ Si ₂
Proline 2TMS	216	220	4	C ₉ H ₂₂ O ₁ N ₁ Si ₂
Valine 2TMS	218	220	2	C ₈ H ₂₀ O ₂ N ₁ Si ₂
Glycine 3TMS	276	278	2	C ₁₀ H ₂₆ O ₂ N ₁ Si ₃
Aspartate 3TMS	232	235	3	C ₉ H ₂₂ O ₂ N ₁ Si ₂
Tyrosine 3TMS	218	220	2	C ₈ H ₂₀ O ₂ N ₁ Si ₂
Glutamate 3TMS	246	250	4	C ₁₀ H ₂₄ O ₂ N ₁ Si ₂
Malate 3TMS	233	236	3	C ₉ H ₂₁ O ₃ Si ₂
Fumarate 2TMS	245	249	4	C ₉ H ₁₇ O ₄ Si ₂
Glycerate 3TMS	189	191	2	C ₇ H ₁₇ O ₂ Si ₂
Glucose 5TMS	319	323	4	C ₁₃ H ₃₁ O ₃ Si ₃
Sucrose 8TMS	103	104	1	C ₄ H ₁₁ O ₁ Si ₁
Trehalose 8TMS	103	104	1	C ₄ H ₁₁ O ₁ Si ₁
Maltose 8TMS	361	367	6	C ₁₅ H ₃₃ O ₄ Si ₃
myo-Inositol 6TMS	103	104	1	C ₄ H ₁₁ O ₁ Si ₁
Pyruvate 1TMS	174	177	3	C ₆ H ₁₂ O ₃ N ₁ Si ₁
Fructose 5TMS	307	310	3	C ₁₂ H ₃₁ O ₃ Si ₃
Methionine 2TMS	176	180	4	C ₇ H ₁₈ N ₁ S ₁ Si ₁

Supplemental Table 4: Gas chromatography–electron impact (GC-EI) fragmentation patterns. TMS: trimethylsilylation. Backbone C atoms stand for the number of carbon atoms from the analyte backbone that can be labeled.

reaction				net flux		[$\frac{nmol}{gFW_s}$ C atoms]					
						opt	All lower	upper	opt	Active lower	upper
	⁵ RuBP	+	¹ CO ₂ $\xrightarrow{6}$ 2 ³ PGA	$F_{(0,CO_2),(1)}$	64.18	60.26	65.90	77.68	71.66	79.65	
				F_{RuBP}^{out}	53.49	50.22	54.92	64.74	59.71	66.37	
				$F_{CO_2}^{out}$	10.70	10.04	10.98	12.95	11.94	13.27	
	⁵ RuBP	+	⁰ O ₂ $\xrightarrow{5}$ ³ PGA + ² Gly	$F_{(0,O_2),(1,16)}$	18.62	16.73	21.02	25.99	22.83	28.34	
				F_{3PGA}^{in}	11.17	10.04	12.61	15.60	13.70	17.00	
				F_{Gly}^{in}	7.45	6.69	8.41	10.40	9.13	11.34	
2	³ PGA		$\xrightleftharpoons{3}$ ³ DHAP	$F_{1,2}$	80.94	76.51	84.23	101.08	93.62	104.57	
	³ DHAP		$\xrightleftharpoons{6}$ ⁶ FBP _{pl.}	$F_{2,3}$	35.17	32.99	36.64	39.48	36.25	40.66	
	⁶ FBP _{pl.}		$\xrightarrow{6}$ ⁶ F6P _{pl.}	$F_{3,4}$	35.17	32.99	36.64	39.48	36.25	40.66	
	⁶ F6P _{pl.}		$\xrightleftharpoons{6}$ ⁶ G6P _{pl.}	$F_{4,5}$	6.32	5.58	6.62	3.19	2.23	3.26	
	⁶ G6P _{pl.}		$\xrightleftharpoons{6}$ ⁶ G1P _{pl.}	$F_{5,6}$	6.32	5.58	6.62	3.19	2.23	3.26	
	⁶ G1P _{pl.}		$\xrightleftharpoons{6}$ ⁶ ADPG	$F_{6,7}$	6.32	5.58	6.62	3.19	2.23	3.26	
	⁶ ADPG		$\xrightarrow{6}$ O	$F_{7,O}$	6.32	5.58	6.62	3.19	2.23	3.26	
	2	³ DHAP		$\xrightleftharpoons{6}$ ⁶ FBP _{cyt.}	$F_{2,8}$	2.51	2.31	2.63	7.16	6.75	7.78
⁶ FBP _{cyt.}			$\xrightleftharpoons{6}$ ⁶ F6P _{cyt.}	$F_{8,9}$	2.51	2.31	2.63	7.16	6.75	7.78	
⁶ F6P _{cyt.}			$\xrightleftharpoons{6}$ ⁶ G6P _{cyt.}	$F_{9,10}$	1.28	1.18	1.34	3.60	3.40	3.92	
⁶ G6P _{cyt.}			$\xrightleftharpoons{6}$ ⁶ G1P _{cyt.}	$F_{10,11}$	1.23	1.12	1.29	3.56	3.35	3.87	
⁶ G1P _{cyt.}			$\xrightleftharpoons{6}$ ⁶ UDPG	$F_{11,12}$	1.23	1.12	1.29	3.56	3.35	3.87	
⁶ F6P _{cyt.}		+	⁶ UDPG $\xrightarrow{12}$ ¹² Suc6P	$F_{(9,12),13}$	2.45	2.25	2.57	7.11	6.7	7.73	
				$F_{F6P_{cyt.}}^{out}$	1.23	1.12	1.29	3.55	3.35	3.87	
				F_{UDPG}^{out}	1.23	1.12	1.29	3.55	3.35	3.87	
	¹² Suc6P		$\xrightarrow{12}$ O	$F_{13,O}$	2.45	2.25	2.57	7.11	6.70	7.73	
	⁶ G1P _{cyt.}		$\xrightarrow{6}$ ⁶ Myo	$F_{10,14}$	0.057	0.056	0.061	0.050	0.049	0.051	
	⁶ Myo		$\xrightarrow{6}$ O	$F_{14,O}$	0.057	0.056	0.061	0.050	0.049	0.051	
	⁶ G6P _{cyt.}	+	⁶ UDPG $\xrightarrow{12}$ ¹² Tre6P	$F_{(10,12),15}$	0.00053	0.00055	0.00064	0.00050	0.00049	0.00052	
				F_{G6P}^{out}	0.00026	0.00028	0.00032	0.00025	0.00024	0.00026	
				F_{UDPG}^{out}	0.00026	0.00028	0.00032	0.00025	0.00024	0.00026	
	¹² Tre6P		$\xrightarrow{12}$ O	$F_{15,O}$	0.00053	0.00055	0.00064	0.00050	0.00049	0.00052	
2	² Gly		$\xrightarrow{4}$ ³ Ser + ¹ CO ₂	$F_{16,(17,CO_2)}$	7.45	6.69	8.41	10.4	9.13	11.34	
				$F_{CO_2}^{in}$	1.86	1.67	2.10	2.60	2.28	2.83	
				F_{Ser}^{in}	5.59	5.02	6.30	7.80	6.85	8.50	
	³ Ser		$\xrightleftharpoons{3}$ ³ Glyc	$F_{17,18}$	5.59	5.02	6.30	7.80	6.85	8.50	
	³ Glyc		$\xrightarrow{3}$ ³ 3PGA	$F_{18,1}$	5.59	5.02	6.30	7.80	6.85	8.50	
	³ 3PGA		$\xrightleftharpoons{3}$ ³ 2PGA	$F_{1,19}$	0	-	-	0	-	-	
	³ 2PGA		$\xrightarrow{3}$ O	$F_{19,O}$	0	-	-	0	-	-	

Supplemental Table 5: Reactions, flux notation, and net flux estimates. Reactions of the model and notation of corresponding flux in carbon atoms participating in each reaction are included. The number above a metabolite indicates the number of carbon atoms in the metabolite. The number above an arrow indicates the number of carbon atoms participating in the reaction. An out-flux of the system is denoted by O used as an index. Note that multi-molecular fluxes are additionally specified as in-flux or out-flux of the corresponding pool. The values of the individual fluxes with and without the active pool assumption are given in the columns titled 'Active' and 'All' respectively. The flux estimates are denoted by the optimal value obtained from the fit 'opt' and the 'lower' and 'upper' 95% confidence limits obtained from the Monte Carlo simulation. The indices correspond to those appearing below the metabolite names in **Supplemental Figure M2** in Supplemental Methods 6. The parameter for the input models and the pool sizes are shown in **Supplemental Table 3**. The time courses of the unlabeled fraction are a part of **Supplemental Dataset 1**.

reaction		exchange flux		[$\frac{nmol}{gFW_s}C$ atoms]					
				All			Active		
				opt	lower	upper	opt	lower	upper
$\overset{3}{3PGA}$	$\xrightleftharpoons{3}$	$\overset{3}{DHAP}$	$F_{1,2}^{ex}$	inf.	132.23	inf.	1.62	0.72	17.48
$\overset{6}{G6P_{pl.}}$	$\xrightleftharpoons{6}$	$\overset{6}{G1P_{pl.}}$	$F_{5,6}^{ex}$	inf.	200.14	inf.	0.02	0.01	4.69
$\overset{6}{F6P_{cyt.}}$	$\xrightleftharpoons{6}$	$\overset{6}{G6P_{cyt.}}$	$F_{9,10}^{ex}$	inf.	21.71	inf.	0.51	0.33	4.04
$\overset{6}{G6P_{cyt.}}$	$\xrightleftharpoons{6}$	$\overset{6}{G1P_{cyt.}}$	$F_{10,11}^{ex}$	inf.	200.14	inf.	inf.	31.08	inf.
$\overset{6}{G1P_{cyt.}}$	$\xrightleftharpoons{6}$	$\overset{6}{UDPG}$	$F_{11,12}^{ex}$	85.56	248.26	inf.	7.90	5.74	inf.
$\overset{3}{Ser}$	$\xrightleftharpoons{3}$	$\overset{3}{Glyc}$	$F_{17,18}^{ex}$	61.29	152.49	inf.	2.12	1.21	inf.
$\overset{3}{3PGA}$	$\xrightleftharpoons{3}$	$\overset{3}{2PGA}$	$F_{1,19}^{ex}$	inf.	28.57	inf.	inf.	23.68	inf.

Supplemental Table 6: Reactions, flux notation, and exchange flux estimates. Reactions of the model and notation of corresponding flux in carbon atoms participating in each reaction are included. The number above a metabolite indicates the number of carbon atoms in the metabolite. The number above an arrow indicates the number of carbon atoms participating in the reaction. The values of the individual fluxes with and without the active pool assumption are given in the columns titled 'Active' and 'All' respectively. The flux estimates are denoted by the optimal value obtained from the fit 'opt' and the 'lower' and 'upper' 95% confidence limites obtained from the Monte Carlo simulation. The indices correspond to those appearing below the metabolite names in **Supplemental Figure M2** in Supplemental Methods 6. The parameter for the input models and the poolsizes are show in **Supplemental Table 3**. The time courses of the unlabeled fraction are a part of **Supplemental Dataset 1**. Unidentifiability of the upper bound is indicated by 'inf.', by corresponding to a set upper bound of 999.

Input function for Glycerate							
$\alpha(t) = Ce^{-ct} + (1 - C) \quad C=0.7147, c=6.808 \cdot 10^{-4} \text{ s}^{-1}$							
Pool size data							
intermediate of CBC	carbon per molecule	total content ($\frac{nmol}{gFW}$)	$\eta_{pl.}$ (%)	remark	pool size ($\frac{nmol}{gFW}$ C atoms)		
RuBP	5	46.7 \pm 8.2	100	assumpt.	233.35 \pm	41.1	
3PGA	3	200.1 \pm 44.8	100	r.e.	600.3 \pm	134.4	
DHAP	3	15.9 \pm 0.6	100	r.e.	47.7 \pm	1.8	
FBP	6	8.9 \pm 2.3	70	n.a.f.	37.38 \pm	9.66	
F6P	6	86.4 \pm 14.6	34	n.a.f.	176.3 \pm	29.78	
SBP	7	9.6 \pm 3.0	75	n.a.f.	50.40 \pm	15.75	
S7P	7	28.0 \pm 5.4	82	n.a.f.	160.72 \pm	30.996	
R5P	5	1.2 \pm 0.2	49	n.a.f.	2.94 \pm	0.49	
RuBP+X5P	5	8.7 \pm 2.6	100	n.a.f.	43.5 \pm	13.00	
2PGA	3	20.0 \pm 4.5	100	r.e.	60.0 \pm	13.5	
sum					1412.59 \pm	290.476	

Supplemental Table 7: Parameter and data used for the simplified model. The part of the denoted pool size of a metabolite effectively taking part in the Calvin-Benson cycle (CBC) is denoted by $\eta_{pl.}$. These values are either taken from the non-aqueous-fractionation data (n.a.f.) or, due to the rapid equilibrium assumption (r.e.), are set to 100% of the plastidic and cytosolic part of the metabolite (*e.g.*, for 3PGA, DHAP, and 2PGA). RuBP is assumed to be exclusively in the plastid (assumpt.).

net flux ($\frac{nmol}{gFWs}$ C atoms)	Simplified model																	
	All			Active			Active 2			Active 3			without F_u			with F_u		
	opt	lower	upper	opt	lower	upper	opt	lower	upper	opt	lower	upper	opt	lower	upper	opt	lower	upper
Starch synthesis	6.32	5.58	6.62	3.19	2.24	3.25	2.57	2.07	2.99	2.68	2.15	2.79	-	-	-	-	-	-
Sucrose synthesis	2.45	2.25	2.57	7.11	6.69	7.73	8.34	7.34	8.39	6.59	6.38	7.46	-	-	-	-	-	-
C atoms lost via photorespiration	1.86	1.67	2.10	2.60	2.28	2.83	2.21	2.01	2.37	2.14	2.03	2.39	1.35	1.09	1.63	1.34	0.71	1.62
myo-inositol synthesis	0.057	0.056	0.061	0.050	0.049	0.051	0.0486	0.0483	0.0508	0.051	0.049	0.043	-	-	-	-	-	-
Trehalose synthesis ($\frac{pmol}{gFWs}$ C atoms)	0.53	0.55	0.64	0.50	0.49	0.52	0.50	0.48	0.52	0.50	0.46	0.51	-	-	-	-	-	-
Gross C fixation	10.70	10.04	10.98	12.95	11.94	13.27	13.17	12.01	13.28	11.46	11.09	12.27	8.10	7.10	9.08	8.09	6.88	9.09
Net C fixation	8.83	8.05	9.11	10.35	9.40	10.67	10.96	9.81	11.08	9.32	8.67	10.05	6.75	5.84	7.51	6.75	5.84	7.73
unlabeled back-flow	-	-	-	-	-	-	-	-	-	-	-	-	0.0017	0.0	0.54	-	-	-
RuBP carboxylation ($\frac{nmol}{gFWs}$)	10.70	10.04	10.98	12.95	11.94	13.27	13.17	12.01	13.28	11.46	11.09	12.27	8.10	7.10	9.08	8.09	6.88	9.09
RuBP oxygenation ($\frac{nmol}{gFWs}$)	3.72	3.35	4.20	5.20	4.57	5.66	4.41	4.02	4.75	4.28	4.07	4.78	2.70	2.18	3.26	2.68	1.42	3.24
$\frac{\text{RuBP oxygenation}}{\text{RuBP carboxylation}}$ (%)	34.8	-	-	40.1	-	-	33.5	-	-	37.3	-	-	33.3	-	-	33.1	-	-

Supplemental Table 8: Comparison of flux estimates regarding different model assumptions. Selected fluxes of the model with regard to different assumptions of inactive pools and fluxes of the simplified model. All: no inactive pools; Active: no inactive pools for Myo and Tre6P; Active 2: no inactive pools for Myo, Tre6P, Ser, Glyc; Active 3: no inactive pools for Myo, Tre6P, Ser, Glyc, 3PGA, 2PGA and DHAP; without F_u : simplified model without unlabeled backflow F_u ; with F_u : simplified model with unlabeled backflow F_u . The flux estimates are denoted by the optimal value obtained from the fit 'opt' and the 'lower' and 'upper' 95% confidence limites obtained from the Monte Carlo simulation.

net flux ($\frac{nmol}{gFWs}$ C atoms)	Active (amino acid mode)			Active		
	opt	lower	upper	opt	lower	upper
Starch synthesis	3.44	2.93	3.80	3.19	2.24	3.25
Sucrose synthesis	6.40	5.54	6.92	7.11	6.69	7.73
C atoms lost via photorespiration	2.53	2.12	2.76	2.60	2.28	2.83
<i>myo</i> -inositol synthesis	0.050	0.047	0.051	0.050	0.049	0.051
Trehalose synthesis ($\frac{pmol}{gFWs}$ C atoms)	0.50	0.49	0.51	0.50	0.49	0.52
Amino acid synthesis	0.00043	0.0	0.35	-	-	-
Gross C fixation	12.41	10.96	13.28	12.95	11.94	13.27
Net C fixation	9.88	8.58	10.66	10.35	9.40	10.67
RuBP carboxylation ($\frac{nmol}{gFWs}$)	12.41	10.96	13.28	12.95	11.94	13.27
RuBP oxygenation ($\frac{nmol}{gFWs}$)	5.05	4.23	5.53	5.20	4.57	5.66
$\frac{\text{RuBP oxygenation}}{\text{RuBP carboxylation}}$ (%)	40.7	-	-	40.1	-	-

Supplemental Table 9: Comparison of flux estimates regarding the influence of an additional flux mode towards amino acid synthesis. The additional flux mode is shown in **Supplemental Figure M2** panel G and **Supplemental Table M3**. The optimal values of the flux estimates are given in the column titled 'opt', while 'lower' and 'upper' contain the 95% confidence intervals obtained from the Monte Carlo simulation.

Compounds	Parent ion	Masses ([M-H] ⁻) formula	Collision energy (eV)	Preferred product ion formula	Masses
Succinatea-0, -1, -2, -3, -4	C ₄ H ₅ O ₄ ⁻	117, 118, 119, 120, 121	10	-CO ₂	73, 73/74, 74/75, 75/76,76
Malate-0, -1, -2, -3, -4	C ₄ H ₅ O ₅ ⁻	133, 134, 135, 136, 137	10	-H ₂ O	115, 116, 117, 118 119
2-oxoglutaratea-0, -1, -2, -3, -4, -5	C ₅ H ₅ O ₅ ⁻	145, 146, 147, 148, 149, 150	10	-CO ₂	101, 101/102, 102/103, 103/104, 104/105, 105
Glutamate-0, -1, -2, -3, -4, -5	C ₅ H ₈ NO ₄ ⁻	146, 147, 148, 149, 150, 151	10	-H ₂ O	128, 129, 130, 131, 132,133
DHAP-0, -1, -2, -3	C ₃ H ₆ O ₆ P ⁻	169, 170, 171, 172	10	[H ₂ PO ₄] ⁻	97
2PGA/3PGA-0, -1, -2, -3	C ₃ H ₆ O ₇ P ⁻	185, 186,187, 188	26	[PO ₃] ⁻	79
G6P/F6P-0, -1, -2, -3, -4, -5, -6	C ₆ H ₁₂ O ₉ P ⁻	259, 260, 261, 262, 263, 264, 265	22	[H ₂ PO ₄] ⁻	97
G1P-0, -1, -2, -3, -4, -5, -6	C ₆ H ₁₂ O ₉ P ⁻	259, 260, 261, 262, 263, 264, 265	31	[PO ₃] ⁻	79
S7P-0, -1, -2, -3, -4, -5, -6, -7	C ₇ H ₁₄ O ₁₀ P ⁻	289, 290, 291, 292, 293, 294, 295, 296	20	[H ₂ PO ₄] ⁻	97
RuBP-0, -1, -2, -3, -4, -5	C ₅ H ₁₁ O ₁₁ P ₂ ⁻	309, 310, 311, 312, 313, 314	22	[H ₂ PO ₄] ⁻	97
FBP-0, -1, -2, -3, -4, -5, -6	C ₆ H ₁₃ O ₁₂ P ₂ ⁻	339, 340, 341, 342, 343, 344, 345	27	[H ₂ PO ₄] ⁻	97
SBP-0, -1, -2, -3, -4, -5, -6, -7	C ₇ H ₁₅ O ₁₃ P ₂ ⁻	369, 370, 371, 372, 373, 374, 375, 376	29	[H ₂ PO ₄] ⁻	97
UTP-0; -9	C ₉ H ₁₄ N ₂ O ₁₅ P ₃ ⁻	483; 492	28	[HO ₆ P ₂] ⁻	159
ATP-0; -10	C ₁₀ H ₁₅ N ₅ O ₁₃ P ₃ ⁻	506.2; 516.2	21	C ₁₀ H ₁₂ N ₅ O ₉ P ₂ ⁻	408; 418
UDPG-0, -1, -2, -3, -4, -5, -6; -15	C ₁₅ H ₂₃ N ₂ O ₁₇ P ₂ ⁻	565, 566, 567, 568, 569, 570, 571; 580	28	C ₉ H ₁₂ N ₂ O ₉ P ⁻	323.1; 332.1
ADPG-0, -1, -2, -3, -4, -5, -6; -16	C ₁₆ H ₂₄ N ₅ O ₁₅ P ₂ ⁻	588, 589, 590, 591, 592, 593, 594; 604	28	C ₁₀ H ₁₃ N ₅ O ₇ P ⁻	346.1; 356.1
Tre6P/Suc6P-0, -1, -2, -3, -4, -5, -6, -7, -8, -9, -10, -11, -12	C ₁₂ H ₂₂ O ₁₄ P ⁻	421 - 433	41	[PO ₃] ⁻	79

Supplemental Table 10: Specific isotopomer-dependent MS parameters used in selected reaction monitoring (SRM). The number associated to the compounds represents the number of ¹³C incorporated in the molecule. A compounds for which the labeling can be present or not in the product ion, leading to alternative parameters for the isotopomers.

Supplemental Methods 1. Compartmentalization and major pathways of carbon metabolism in a photo-synthetically active leaf

The Calvin-Benson cycle and starch synthesis occur in the chloroplast. Starch is synthesized from the Calvin-Benson cycle intermediate F6P via phosphoglucoisomerase, phosphoglucomutase and ADPglucose pyrophosphorylase (AGPase), followed by a complex set of polymerization reactions. Sucrose synthesis involves the export of triose-phosphates from the chloroplast via the triose-phosphate:phosphate translocator (TPT) (Fliege et al., 1978), followed by their conversion to hexose phosphates by a cytosolic FBPase and conversion of hexose phosphates and UDP-glucose (UDPG) to sucrose by the dedicated and plant-specific enzymes sucrose phosphate synthase (SPS) and sucrose phosphatase (Stitt et al., 1980, 1989, 2010), which are exported. TPT also catalyze the exchange of triose-phosphate and 3PGA that facilitates export of ATP and NADPH to the cytosol. The bio-synthetic pathways are regulated by metabolic reactions involving sugar nucleotides, which are tightly regulated by metabolic reactions involving ADP-glucose (ADPG) pyrophosphorylase, converting G1P into ADPG and regulating starch bio-synthesis (Zeeman et al., 2007), and by the cytosolic FBPase and sucrose phosphate synthase, transforming UDPG into sucrose-6-phosphate and regulating sucrose content (Stitt, 1987; Stitt et al., 2010).

The complexity of compartmentalization is even larger for the non-phosphorylated metabolites involved in photorespiration and sugar, organic acid and amino acid metabolism. Photorespiration involves reactions in the peroxisome, mitochondria and cytosol, before glycerate returns to the chloroplast (for recent reviews, see (Stitt et al., 2010; Bauwe et al., 2010)). Organic acid and amino acid metabolism is distributed between the cytosol, plastids and mitochondria. Furthermore, the vacuole, which occupies most of the volume of a plant cell, contains substantial pools of sugars, organic acids and amino acids. Consequently, information about the overall content of metabolites does not provide a reliable guide to the levels of metabolites in the individual sub-cellular compartments and pathways.

Sub cellular fractionation studies show that Calvin-Benson cycle intermediates, such as: RuBP, SBP and FBP, are largely confined to the plastid, as is ADPG which is a dedicated precursor for starch synthesis. While triose-phosphates, 3PGA and hexose-phosphates are distributed between the plastid and cytosol, UDPG (involved in sucrose metabolism), 2-phosphoglycerate and PEP are largely restricted to the cytosol. Furthermore, a substantial part of the cellular complement of sucrose and amino acids and almost the entire cellular complement of organic acids, like malate and fumarate and free reducing hexose sugars (glucose and fructose), is located in the vacuole (Gerhardt and Heldt, 1984; Gerhardt et al., 1987).

Supplemental Methods 2. Labeling Strategies

Differential pool size turnover during photosynthesis

A considerable challenge is posed by the interplay between the interlocked pathways of carbon (C) fixation, and by the very large range in the predicted turnover times of metabolites in these pathways. An enormous range in the half-time of different processes is a hallmark of photosynthesis ranging from 6-13 ms (Cournac et al., 2002), for photo-chemical reactions, to 150 ms (Maxwell and Biggins, 1976), for steps in electron transport, and 2-20 s for turnover of ATP and NADPH (Bialeski, 1973). Based on the pathway stoichiometry and the measured size of the metabolite pools, the estimated turnover times of many Calvin-Benson cycle metabolites during rapid photosynthesis are less than a second (Stitt et al., 1980; Arrivault et al., 2009). Even though only one C is fixed per cycle turnover, the recurring passage of metabolites, multiple times around the cycle, will result in rapid randomization of label implying that it may be difficult to resolve detailed labeling patterns in the Calvin-Benson cycle. The turnover rates of cytosolic metabolites involved in sucrose synthesis may be considerably slower (Stitt et al., 1980, 1983; Arrivault et al., 2009). The levels of metabolites like glycine and serine, which are involved in photorespiration, are also high. Assuming that the entire pool participates in the photorespiratory pathways, their turnover times may be of the order of 5 min or more (Cegelski and Schaefer, 2005). Slow turnover of these pools is also indicated by the occurrence of a large so-called “post-illumination” burst of CO₂ release. This lasts several minutes, is only seen in conditions when photorespiration is occurring and is thought to reflect the decarboxylation of large internal photorespiratory pools that have accumulated in the light. We can therefore anticipate that while there will be rapid and coordinated incorporation of ¹³CO₂ in all Calvin-Benson cycle intermediates, this will be modified by continuing in-fluxes of unlabeled C from photorespiration until the pools in the latter pathway are fully labeled. It is of prime importance

that these differential turnover rates are considered in the design and subsequent interpretation of labeling strategies, since it may be required to discard different data points across the kinetics of labeling for a given pathway depending on the turnover rates of the metabolite pools which it contains.

Brief review of methods for flux estimation from labeling data

Approaches to model individual reaction rates from ^{13}C labeling data can be classified based on two criteria: (i) the type of metabolic state from which the data is obtained and (ii) the biochemical knowledge used in the mathematical formulation. With respect to the first criterion, experimental ^{13}C labeling approaches can be divided into metabolic non-steady-state and steady-state experiments (Wahl et al., 2008). Data from non-stationary experiments can be employed to identify the properties of reaction kinetics, while data from metabolic stationary approaches are usually used to quantify intracellular fluxes. Several types of biochemical knowledge can be used to support flux estimation: (i) the stoichiometry of the metabolic reactions, (ii) carbon fate (so-called atom) mappings, which describe the transition of carbon atoms for each reaction in the system, (iii) optimization of an objective function (e.g., sum of squared residuals weighted by the inverse of the experimental variances) can be used to further constrain which theoretically feasible fluxes are consistent with the available data, and (iv) various kinetic parameters that capture allosteric regulations (for details, see (Selivanov et al., 2006; Sauer, 2006; Wahl et al., 2008)).

The mathematical apparatus used to translate this biochemical knowledge into a metabolic model ranges from simple mass-balance equations (Katz and Wood, 1960), isotopomer balance equations (Wiechert et al., 1999), elementary metabolite units (EMUs) (Antoniewicz et al., 2006; Young et al., 2008), employing decompositions of linear systems of equations formulated by using atom mapping matrices, to systems of ordinary differential equations (Mason and Rothman, 2004) coupled with atom mapping matrices (Schmidt et al., 1997). Atomic mappings are usually obtained from computational predictions with additional set of assumptions (Ravikirthi et al., 2011).

However, these methods require knowledge about the fragment position in the molecule.

In addition, constraint-based models resulting from the combination of mass balances and flux ratios with the objective of minimizing the sum of the weighted squared residuals have been employed to obtain the distribution of reaction fluxes (Fischer et al., 2004). While these methods have proven valuable for estimating the inter-cellular fluxes in some systems (see e.g. (Young et al., 2011)), to quantify the inter-cellular net fluxes of a larger set of photosynthesis-related pathways in illuminated *Arabidopsis thaliana* we chose to make use of another computational alternative, which can be readily implemented for flux estimation.

Supplemental Methods 3. Extended Kinetic Flux Profiling

Kinetic Flux Profiling (KFP) (Yuan et al., 2006, 2008) is a method for determining reaction fluxes based on the washout of the unlabeled fraction of a metabolic pool. The method is based on modeling the delay in labeling of substrate and product pools of a mono-molecular reaction. The substrate pool is assumed to show an exponential-decay-like behavior. Applied to each mono-molecular reaction in a given network, the method allows estimation of fluxes as local properties of the network. We extend the method to irreversible multi-molecular reactions to estimate the steady-state flux distribution of all reactions as a global property, and call it extended KFP. A list of all mathematical definitions is shown in **Supplemental Table M1**. Given a metabolite X , let x^u denote its unlabeled content, and x^T , its total content in an observed (measured) metabolic steady state. The unlabeled fraction of X , denoted by \tilde{x} , is then defined as:

$$\tilde{x} = \frac{x^u}{x^T}. \quad (1)$$

Assumptions

Kinetic Flux Profiling is based on three assumptions: (i) The metabolic system is at a metabolic steady state, *i.e.*, all concentrations of metabolites and fluxes are constant¹; (ii) Enzymes do not discriminate

¹Note that the metabolic steady state refers to the total number of molecules in a pool, whereas the isotopic steady state deals with the distribution of different mass isotopomers.

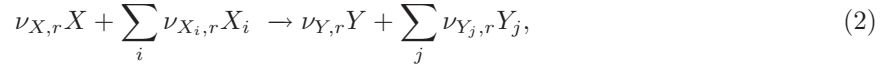
$\alpha(t)$	input function presenting unlabeled fraction of glycerate in simplified model
$\eta, \eta_{\text{cyt.}}, \eta_{\text{pl.}}$	fraction of the total content in cytosol or plastid
\hat{x}_i	isotopic peak with i labeled carbon atoms
ν_r	rate of reaction r
$\nu_{X_i, r}, \nu_{i, r}$	stoichiometric coefficient of metabolite X_i and reaction r
ϕ^l	amount of non cyclic mode \vec{M}^l
$\sigma_{i, j}$	mean absolute difference of flux $F_{i, j}$ in leave-one-out validation
\mathbf{N}	stoichiometric matrix
$\theta(t)$	function generating unlabeled in-flux from labeled fraction
$\tilde{x}, \tilde{x}_{\text{cyt.}}, \tilde{x}_{\text{pl.}}$	unlabeled fraction of X
\tilde{x}^*	partially labeled pool
$\varphi_{i, j}$	amount of exchange flux $M_{i, j}^{\text{ex}}$
$\varsigma_{i, j}$	relative mean absolute difference of flux $F_{i, j}$ in leave-one-out validation
\vec{M}^l	elementary mode of steady state flux distribution
\vec{v}	rate vector
A, B, a, b, C, c	parameters of exponential fits in input functions
F^{ex}	exchange flux
$F_{X, r}^{\text{in/out}}$	in-flux or out-flux of X caused by reaction r
$f_{X, r}^{\text{in/out}}$	unlabeled in-flux or out-flux of X caused by reaction r
$F_X^{\text{in/out}}$	in-flux or out-flux of X
F^{net}	net flux
$F_{(a, b), (c, d)}$	flux of a reaction with a and b as indices of substrates and c and d of products
F_{gross}	gross carbon fixation (simplified model)
F_{net}	net carbon fixation (simplified model)
F_{photo}	flux of carbon atoms lost via photorespiration (simplified model)
F_u	unlabeled in-flux to CBC (simplified model)
$F_{i, j}$	flux from pool with i to pool with index j
F_X	overall flux through a pool X caused by all reactions
h_X^{in}	effective unlabeled in-flux
k	time constant
$M_{i, j}^l$	flux of elementary mode of steady state flux distribution \vec{M}^l
n_r	number of carbon atoms participating in reaction r
n_X	number of carbon atoms of interest of metabolite X
r	reaction
S_e^r	set of indices of products of reaction r
X	metabolite
$x^T, x_{\text{cyt.}}^T, x_{\text{pl.}}^T$	total amount of X or steady state pool size
x^u	unlabeled (mono-isotopic) amount of X
act.	active
cyt.	cytosol
inact.	inactive
pl.	plastid
ref	reference
C	carbon
CBC	Calvin-Benson cycle
CTM	Carbon transition maps
eKFP	extended Kinetic flux profiling
KFP	Kinetic flux profiling
m/z	ratio mass/charge
SD	standard deviation
t	time

Supplemental Table M1: List of mathematical definitions

between molecules of different labeling state, *i.e.*, enzymes are insensitive to the incorporated heavy isotopes; and finally, (iii) The metabolic pools are considered well-mixed. Therefore, an enzyme does not distinguish between molecules belonging to the same metabolic pool. Moreover, implicitly, all molecules of the same pool have equal probability to react, and all effects of spatial distributions and those of enzymatic mechanism are assumed negligible. Following these assumptions a model of differential equations can be derived to describe the time-dependent behavior of the washout via mass-action-like kinetics.

General remarks regarding fluxes and rates

A chemical reaction r describes a process of transformation of substrate molecules to product molecules. The corresponding rate v_r of the reaction affects the quantities of the involved molecules constrained by the stoichiometric coefficients. From the perspective of metabolic pools, the rate acts as an out-flux at the pool of a substrate and as an in-flux at a product side. Given a reaction r :



let $F_{X,r}^{\text{out}}$ denote the out-flux from the pool of substrate X through r , $F_{Y,r}^{\text{in}}$, the in-flux to the pool of product Y , and $\nu_{X,r}$ the corresponding stoichiometric coefficient. In- and out-fluxes are coupled by their stoichiometry:

$$F_{X,r}^{\text{out}} = \nu_{X,r}v_r \quad (3)$$

$$F_{Y,r}^{\text{in}} = \nu_{Y,r}v_r. \quad (4)$$

The overall in-flux F_X^{in} to the pool of metabolite X is the sum over in-fluxes $F_{X,r}^{\text{in}}$ of the reactions in which X appears as a product, while the overall out-flux F_X^{out} is the sum over out-fluxes $F_{X,r}^{\text{out}}$ of all reactions in which X acts as a substrate, *i.e.*,

$$F_X^{\text{in}} = \sum_r F_{X,r}^{\text{in}}, \quad (5)$$

$$F_X^{\text{out}} = \sum_r F_{X,r}^{\text{out}}. \quad (6)$$

If a flux of atoms, *e.g.*, carbon (C) atoms, is of interest rather than a flux of molecules, the flux can be expressed as:

$$F'_X = nF_X = n\nu_{X,r}v_r, \quad (7)$$

where n denotes either the number of atoms of interest within a molecule X or the number of carbon atoms participating in the reaction r . The reference to these fluxes should be clear from the context.

Constraints of metabolic steady state

In a metabolic steady state, the overall in-flux F_X^{in} equals the overall out-flux F_X^{out} . Therefore, both in- and out-fluxes can be used to describe the overall flux through the pool of X :

$$F_X = F_X^{\text{in}} = F_X^{\text{out}}. \quad (8)$$

Since in a reaction network at metabolic steady state, the total pool size, x^T , of each metabolite, X , does not change, the mass balance equation yields the following constraint:

$$\frac{dx^T}{dt} = \sum_r F_{X,r}^{\text{in}} - \sum_r F_{X,r}^{\text{out}} = 0. \quad (9)$$

For a given reaction network, by using Eqs. (3) and (4), this can be alternatively expressed as:

$$\mathbf{N}\vec{v} = 0, \quad (10)$$

where \mathbf{N} denotes the stoichiometric matrix and $\vec{\nu}$ is the rate vector (Heinrich and Schuster, 1996). Each solution of the algebraic systems in Eqs. (9) and (10) describes a possible flux distributions for the reaction network in a metabolic steady state. The general solution can be expressed as a linear combination of a set comprising l linearly independent flux distributions, generating the kernel (null-space) of the stoichiometric matrix. For instance, the general solution can be expressed as a non-negative linear combination of extreme pathways (Schilling et al., 2000) or elementary flux modes (Schuster et al., 1999). If all reactions are assumed to be irreversible, or rather only the net flux of the reactions is of interest, each extreme pathway is an elementary mode (Papin et al., 2004). Each of these descriptions provides a parameterization of all possible steady-state flux distributions.

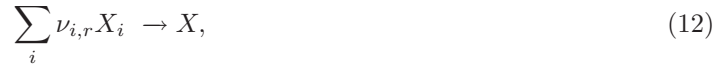
Fluxes of unlabeled metabolites

Due to assumptions (ii) and (iii), the unlabeled out-flux $f_{X,r}^{\text{out}}$ in the out-flux $F_{X,r}^{\text{out}}$ from the pool of X is given by:

$$f_{X,r}^{\text{out}} = F_{X,r}^{\text{out}} \frac{x^u}{x^T}. \quad (11)$$

In other words, the unlabeled fraction of the out-flux equals the unlabeled fraction of the corresponding pool of the substrate.

Out-fluxes may result in in-fluxes to the product pool of the reaction. The unlabeled fraction of an in-flux depends on all reactants. The resulting product is only unlabeled if all reactants are unlabeled. Given a reaction r in which metabolite X is produced by consuming $\nu_{i,r}$ molecules of metabolite X_i , the reaction can be written as:



where $\nu_{i,r}$ are the stoichiometric coefficients. Let

$$S_e^r = \{X_i \mid \nu_{i,r} \neq 0\} \quad (13)$$

denote the set of substrate metabolites of reaction r . The unlabeled in-flux, $f_{X,r}^{\text{in}}$, of such a reaction is given by the following mass-action-like relationship:

$$f_{X,r}^{\text{in}} = F_{X,r}^{\text{in}} \prod_{i \in S_e^r} \left(\frac{x_i^u}{x_i^T} \right)^{\nu_{i,r}}. \quad (14)$$

The total fluxes $F_{X,r}^{\text{in}}$ and $F_{X,r}^{\text{out}}$ of such a multi-molecular reactions are stoichiometrically constrained, as shown in Eqs. (3) and (4), by:

$$F_{X,r}^{\text{in}} = \frac{F_{X,r}^{\text{out}}}{\nu_{i,r}}. \quad (15)$$

In-fluxes from decay-like reactions with more than one product, *i.e.*, reactions of the form:



are more difficult to handle in the framework of KFP, as partially labeled molecules can split in labeled and unlabeled fragments. These reactions are excluded from further considerations, and, as a result, reactions of type given in Eq. (12) are treated as irreversible. To solve this problem several approaches may be applied:

1. Carbon transition maps (CTM) (Mu et al., 2007) offer the means to resolve the problem; if accurate mappings are known. The number of equations increases exponentially and leads to difficulties with regard to fitting the equations to available experimental data.

2. The unlabeled in-flux can be extended to:

$$f_{X_j,r}^{\text{in}} = F_{X_j,r}^{\text{in}} \left(\frac{x^u}{x^T} + \sum_{i=1}^n \theta_{i,r}(t) \frac{x^{(i)}}{x^T} \right), \quad (17)$$

where n denotes the number of carbon atoms of the metabolite X_j , $x^{(i)}$, the isotopic content with i labeled carbon atoms and $\theta_{i,r}$, denoting a time-dependent function, describes the effective generation of unlabeled metabolite X_j from labeled metabolite X . Note that:

$$f_{X_j,r}^{\text{in}} \leq F_{X_j,r}^{\text{in}} \Rightarrow \frac{x^u}{x^T} + \sum_{i=1}^n \theta_{i,r}(t) \frac{x^{(i)}}{x^T} \leq 1. \quad (18)$$

The function θ_i could be approximated by fitting the model to experimental data and may further be restricted by additional knowledge about the underlying reaction.

3. If the label can be assumed to be randomly distributed within each mass-isotopomer for the substrates molecule and all times, all $\theta_{i,r}(t)$ are constant. They are given by the ratio of the number of possible labeling patterns resulting in an unlabeled product to the number of all possible labeling patterns:

$$\theta_i(t) = \frac{\binom{n}{i}}{\binom{n-n_s}{i}}. \quad (19)$$

The number of carbon atom of the product is denote as n_s .

4. Partially labeled pools can be included in the model. Thereby, partially labeled pools trace partially labeled molecules which can decay in their unlabeled and labeled “sub-units“. This approach might be only useful for small network, since such a tracing or mapping of a smallest sub-unit may essentially be identical to the CTM approach, discussed above.

Dynamics of unlabeled/mono-isotopic states

The mass-balance equation for the unlabeled amount of a metabolic pool X can be derived by summing over all in-flux and out-flux reactions, in which X participates as product and substrate, respectively:

$$\frac{dx^u}{dt} = \sum_r F_{X,r}^{\text{in}} \prod_{i \in S_e^r} \left(\frac{x_i^u}{x_i^T} \right)^{\nu_i} - \sum_r F_{X,r}^{\text{out}} \frac{x^u}{x^T}. \quad (20)$$

Similarly, by using Eqs. (1) and (20), the unlabeled fraction of X is described by:

$$\frac{d\tilde{x}}{dt} = \sum_r \frac{F_{X,r}^{\text{in}}}{x^T} \prod_{i \in S_e^r} \tilde{x}_i^{\nu_i} - \sum_r \frac{F_{X,r}^{\text{out}}}{x^T} \tilde{x}. \quad (21)$$

An analytical solution of this non-linear differential equation cannot be found in general. However, a numerical solution can be readily obtained. The possible stiffness of the system of differential equations has to be taken into account, and a proper numerical integration algorithms chosen (Ernst and Gerhard, 1996; Hindmarsh, 1983; Petzold, 1983). For a given metabolic network such a system of differential equations can be derived and solved; moreover, a minimum-error-solution can be fitted to available data. To this end, different heuristic techniques of numerical non-linear optimization, *e.g.*, simulated annealing, evolutionary algorithms, or swarm-based techniques, can be applied (Chong and Zak, 2008). The optimization problem is constrained by the condition of the metabolic steady state in Eq. (9). The choice of optimization algorithm depends on the particular system properties and, thus, on the network structure. For instance, for a simple network of only a few metabolites other optimization algorithms based on gradient-descend or Newton method may be more efficient.

Note that for resolving a minimum error solution for the fluxes, the total pool size, x^T , of every metabolite in the system has to be known. According to the experimental setup, the initial conditions of the system are given as fully unlabeled pools for most of the metabolites. Therefore, the used experimental data have to be corrected for natural abundance (van Winden et al., 2002). In addition, one

or maybe more in-fluxes are fully labeled, or their time-dependent labeling state is known. Pools which are partially or fully labeled in the beginning are pools which are replaced by labeled metabolites due to the experimental setup. A complete replacement of such metabolites can be modeled as an indicator function. In addition variance-weighted error function is predominantly used when dealing with data showing variance (Press et al., 2007).

Technical Remarks

The effective unlabeled fraction $h_X^{\text{in}}(t)$ of the in-flux to a pool x can be defined as the ratio of the sum over all unlabeled in-fluxes $f_{X,r}^{\text{in}}$, given in Eq. (14), to the overall flux F_X through the metabolic pool, given in Eq. (8); thus:

$$h_X^{\text{in}}(t) = \frac{\sum_r F_{X,r}^{\text{in}} \prod_{i \in S_e^r} \left(\frac{x_i^u}{x_i^T} \right)^{\nu_i}}{\sum_r F_{X,r}^{\text{in}}} = \frac{\sum_r F_{X,r}^{\text{in}} \prod_{i \in S_e^r} \left(\frac{x_i^u}{x_i^T} \right)^{\nu_i}}{F_X^{\text{in}}}. \quad (22)$$

By using Eqs. (5)-(8) and (22), the mass-balance equation for x can be expressed as:

$$\frac{dx^u}{dt} = F_X h_X^{\text{in}} - F_X \frac{x^u}{x^T}. \quad (23)$$

With respect to Eqs. (14) and (22), if there does not exist X such that $X = X_i$ with $i \in S_e^r$, we call $f_{X,r}^{\text{in}}$ and h_X^{in} independent of $x(t)$. In this strictly forward-coupled case, Eq. (20) becomes an in-homogeneous linear differential equation whose solution can be expressed as:

$$\frac{x^u(t)}{x^T} = e^{-kt} + k \int_0^t e^{-k\tau} h_X^{\text{in}}(t - \tau) d\tau, \quad (24)$$

$$k = \frac{\sum_r F_{X,r}}{x^T} = \frac{F_X}{x^T}. \quad (25)$$

With respect to the theory of linear filters (Brockwell and Davis, 2006), each metabolic pools whose in-fluxes are independent of its own state can be viewed as a linear filter of first order, which exponentially smooths $h_X^{\text{in}}(t)$ as its input function. In other words, each metabolic pool relaxes to the state of its in-flux with its own time constant k and in this way smooths the input. The solution for all $x^u(t)$ in strictly forward-coupled networks or parts of a networks can be calculated successively by applying Eq. (24).

For a system composed only of mono-molecular reactions the mass-balance equation Eq. (20) reduces to

$$\frac{dx^u}{dt} = \sum_r F_{X,r}^{\text{in}} \frac{x_i^u}{x_i^T} - \sum_r F_{X,r}^{\text{out}} \frac{x^u}{x^T}. \quad (26)$$

The index i denotes the pools of the substrates of the reaction r . For reasons of brevity the notation can be changed by denoting fluxes from pool i to pool j as $F_{i,j}$:

$$\frac{dx_m^u}{dt} = \sum_i F_{i,m} \frac{x_i^u}{x_i^T} - \sum_j F_{m,j} \frac{x_m^u}{x_m^T}. \quad (27)$$

Here Eq. (27) represents a linear differential equations with constant coefficients. The form of the analytical solution can always be found by standard techniques (Bronshtein et al., 2007), and is represented by a linear combination of exponential functions. Note that this only refers to the non-singular solution. Moreover, for a reversible mono-molecular reaction, a rapid-equilibrium approximation can be employed (Heinrich and Schuster, 1996). If metabolic pools are connected via high exchange fluxes, they can be approximately modeled as one pool, showing the same labeling behavior. This, then, decreases the number of independent parameters of the system. As a result, the differential equation system is converted to algebraic differential equation system.

Illustrative examples

In the following, the KFP approach will be illustrated with five examples of reactions typically arising in large models. In each example a single metabolite pool takes a fully labeled in-flux, whereas all pools are fully unlabeled in the beginning.

Example 1: Exponential washout of a single metabolite The washout-behavior of one pool of a metabolite X_1 with only one in-flux, which is completely labeled in the beginning of the experiment, can be described by:

$$\frac{dx_1^u}{dt} = -F \frac{x_1^u}{x_1^T}. \quad (28)$$

As there is only labeled in-flux to the pool, the unlabeled in-flux is equal to zero. The solution of this equation is an exponential function of the unlabeled part of the pool (see **Supplemental Figure M1A**):

$$x_1^u(t) = x_1^T e^{-k_1 t}, \quad (29)$$

$$k_1 = \frac{F}{x_1^T}. \quad (30)$$

Example 2: Metabolic chain In a mono-molecular chain, the metabolite X_1 (from Example 1) may irreversibly react to produce metabolite X_2 . The differential equation for x_2^u , as a successor, can be expressed as:

$$\frac{dx_2^u}{dt} = F \frac{x_1^u}{x_1^T} - F \frac{x_2^u}{x_2^T}. \quad (31)$$

Since there is no flux from x_2 to x_1 , the equations for x_1 remain unchanged. The corresponding solution:

$$\frac{x_2^u(t)}{x_2^T} = \frac{k_1}{k_1 - k_2} e^{-k_2 t} - \frac{k_2}{k_1 - k_2} e^{-k_1 t}, \quad (32)$$

$$k_1 = \frac{F}{x_1^T}, \quad (33)$$

$$k_2 = \frac{F}{x_2^T}, \quad (34)$$

shows a delay, which is caused by unlabeled molecules coming from pool x_1 and passing through pool x_2 (see **Supplemental Figure M1B**).

Example 3: Branched chain and unlabeled in-fluxes Additional completely unlabeled in-fluxes $F_{0,i}^u$ to one of the pools in such a irreversible mono-molecular chain may be caused by degradation of macro-molecules, prohibiting complete washout of the pool (Yuan et al., 2008). Such a system is specified by:

$$\frac{dx_1^u}{dt} = F_{0,1}^u - (F_{1,2} + F_{1,0}) \frac{x_1^u}{x_1^T}, \quad (35)$$

$$\frac{dx_2^u}{dt} = F_{1,2} \frac{x_1^u}{x_1^T} + F_{0,2}^u - F_{1,0} \frac{x_2^u}{x_2^T}. \quad (36)$$

The system in Eqs. (35) and (36) describes a simple irreversible branched chain with an additional out-flux of the precursor pool, x_1 . The corresponding solution shows an offset, which is given by the proportion of the effective unlabeled in-flux to the overall in-flux of the pool (see **Supplemental Figure M1C**). The effective unlabeled in-flux is caused by all unlabeled in-fluxes of the precursor pools:

$$\frac{x_1^u(t)}{x_1^T} = (1 - \alpha) e^{-k_1 t} + \alpha, \quad (37)$$

$$\frac{x_2^u(t)}{x_2^T} = \frac{(1 - \alpha)(1 - \beta)}{k_1 - k_2} (k_1 e^{-k_2 t} - k_2 e^{-k_1 t}) + (1 - (1 - \alpha)(1 - \beta)), \quad (38)$$

$$k_1 = \frac{F_{1,2} + F_{1,0}}{x_1^T}, \quad (39)$$

$$k_2 = \frac{F_{1,2} + F_{0,2}}{x_2^T}, \quad (40)$$

$$\alpha = \frac{F_{0,1}}{F_{0,1} + F_{1,2}}, \quad (41)$$

$$\beta = \frac{F_{0,2}}{F_{0,2} + F_{2,0}}. \quad (42)$$

As already mentioned, a mono-molecular reaction network can be described by a system of linear ordinary differential equations. The solution for the time-dependent behavior of the unlabeled fraction is in general a sum of exponential functions. The non-singular case is here excluded. In an irreversible branched chain, all time constants of the exponential are given as quotients of the overall fluxes and pool sizes, which can be derived from Eq. (24). Note that the behavior changes if the system becomes reversible or cyclic. In such a case, the time-constants can be expressed as a function of all pools and fluxes in the system.

Example 4: Reversibility As the simplest case, a reversible mono-molecular reaction can be captured by an irreversible in-flux and an irreversible out-flux. For reversible reactions, it is useful to describe the flux as net and exchange fluxes:

$$F^{\text{net}} = F_{1,2} - F_{2,1}, \quad (43)$$

$$F^{\text{ex}} = F_{2,1}. \quad (44)$$

The example can in turn be described as:

$$\frac{dx_1^u}{dt} = -(F^{\text{net}} + F^{\text{ex}}) \frac{x_1^u}{x_1^T} + F^{\text{ex}} \frac{x_2^u}{x_2^T}, \quad (45)$$

$$\frac{dx_2^u}{dt} = (F^{\text{net}} + F^{\text{ex}}) \frac{x_1^u}{x_1^T} - (F^{\text{net}} + F^{\text{ex}}) \frac{x_2^u}{x_2^T}. \quad (46)$$

The time constants $k_{1,2}$ of this system are given by:

$$k_{1,2} = -\frac{(F^{\text{net}} + F^{\text{ex}})(x_1^T + x_2^T)}{x_1^T x_2^T} \pm \sqrt{\frac{(F^{\text{net}} + F^{\text{ex}})^2 (x_1^T + x_2^T)^2}{(x_1^T x_2^T)^2} - \frac{F^{\text{net}} + F^{\text{ex}}}{x_1^T x_2^T} F^{\text{net}}}. \quad (47)$$

If the exchange flux F^{ex} equals zero, the system becomes identical to that in Example 2 with the corresponding time constants. The limits of k_1 and k_2 for F^{ex} at infinity show the following behavior:

$$\lim_{F^{\text{ex}} \rightarrow \infty} k_1 = -\frac{F^{\text{net}}}{x_1^T + x_2^T}, \quad (48)$$

$$\lim_{F^{\text{ex}} \rightarrow \infty} k_2 = -\infty, \quad (49)$$

where k_1 results in the same value one would expect for a pool z with corresponding pool size $z^T = x^T + y^T$, which behaves like Example 1 (Eqs. (29) - (30)). In this case, the solution for both pools is the same exponential decay with time constant k_1 . The second time-constant k_2 bears less importance for the solution, with $F^{\text{ex}} \rightarrow \infty$, since the weight of the corresponding exponential function reaches zero. Both pools are in rapid equilibrium and, therefore, they behave as one pool. The dashed lines in **Supplemental Figure M1D** illustrates the smaller differences in the time-dependent behavior of both pools with increasing exchange flux.

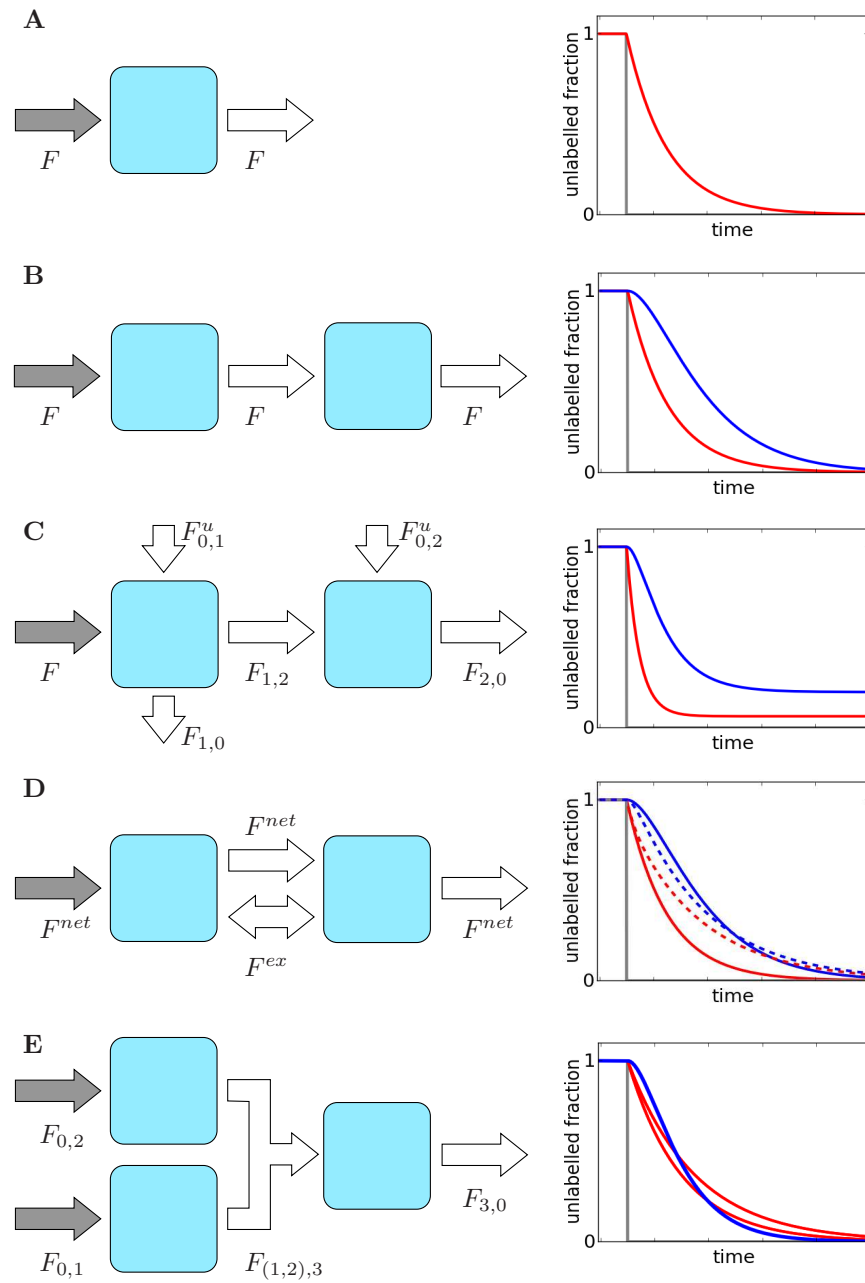
Example 5: An irreversible bi-molecular reaction In an irreversible bi-molecular system, both pools of the substrates might show an exponential decay of their unlabeled fractions:

$$\frac{x_1^u(t)}{x_1^T} = e^{-k_1 t}, \quad (50)$$

$$\frac{x_2^u(t)}{x_2^T} = e^{-k_2 t}. \quad (51)$$

The dynamic behavior of the pool of the product, according to Eq. (24), can be expressed as:

$$\frac{dx_3^u}{dt} = F_{(1,2),3} \frac{x_1^u}{x_1^T} \frac{x_2^u}{x_2^T} - F_{(1,2),3} \frac{x_3^u}{x_3^T}. \quad (52)$$



Supplemental Figure M1: Illustration of KFP on reactions typically occurring in network models. Grey arrows and lines indicate fluxes completely labeled at $t = 0$. Red lines indicate precursors and blue lines successors. Solid lines in panel D are for $F^{ex} = 0$, and dashed lines are for $F^{ex} > 0$.

The solution for the product x_3 is:

$$\frac{x_3^u(t)}{x_3^T} = \frac{k_3}{k_3 - (k_1 + k_2)} e^{-(k_1 + k_2)t} - \frac{k_1 + k_2}{k_3 - (k_1 + k_2)} e^{-k_3 t}, \quad (53)$$

$$k_3 = \frac{F_{(1,2),3}}{x_3^T}. \quad (54)$$

Although the solution shows a delay, the unlabeled fraction of the product can decay faster than the reactants (see **Supplemental Figure M1E**). This follows from the higher number of possible labeling positions in the product.

Supplemental Methods 4. Optimization - Fit to the mass-spectrometric data

According to Eqs. (71) and (72), all fluxes in the differential equations system can be expressed as a function of the independent parameters. The system can be integrated numerically for a given set of parameters. The obtained solutions describe the time-dependent washout of the unlabeled fraction for all modeled pools. The solutions for the phosphorylated hexoses are compartmentalized between plastid and cytosol. Therefore, the plastidic and cytosolic pool have to be weighted summed in order to fit them to the experimental data of the unlabeled fraction of the metabolite:

$$\tilde{x}_{\text{all}}(t) = \eta_{\text{pl.}} \tilde{x}_{\text{pl.}}(t) + \eta_{\text{cyt.}} \tilde{x}_{\text{cyt.}}(t). \quad (55)$$

The weights η display the proportion provided by non-aqueous-fractionation.

The variance-weighted mean squared error (WMSE) is given by:

$$WMSE = \sum_m \sum_t \frac{(\tilde{x}_{t,m}^{\text{obs.}} - \tilde{x}_{t,m}^{\text{sim.}})^2}{\sigma_{t,m}^{\text{obs.}}}, \quad (56)$$

where $\tilde{x}_{t,m}^{\text{obs.}}$ denotes the observe unlabeled fraction of metabolite m at time t and $\tilde{x}_{t,m}^{\text{sim.}}$ the corresponding simulation. In order to find a minimum-error solution, a simulated annealing algorithm (Kirkpatrick et al., 1983) is applied, followed by a quasi-Newton optimization (BFGS) (Byrd et al., 1995). All $\varphi_{i,j}$ are hyperbolically transformed by:

$$\varphi'_{i,j} = \frac{\varphi_{i,j}}{1 + \varphi_{i,j}} \quad (57)$$

in order to take values from the interval $[0, 1]$ (Wiechert and De Graaf, 1997). For each particular fit, 40 such runs are performed and the best one is chosen. The used parameters are given in **Supplemental Table M2**. **Supplemental Dataset 1** includes the used the experimental data and the corresponding standard deviations.

For Tre6P and Suc6P only one replica was measure. In order to obtain a standard deviation for this measurement we chose the largest standard deviation of the time course of the particular metabolite. **Supplemental Table 3** shows the experimental data of the poolsizes.

The model is implemented by using Python 2.6.0, Numpy 1.3.0 and Scipy 1.3.0. Numerical integration is performed with `scipy.integrate.odeint`, which is a wrapper for LSODA (Petzold, 1983) from the library ODEPACK (Hindmarsh, 1983). The simulated annealing was implemented in Python 2.6.0. The quasi-Newton optimization is performed by `scipy.optimize.fmin_l_bfgs_b` (Zhu et al., 1997).

Supplemental Methods 5. Estimation of confidence intervals from Monte Carlo simulation

Monte Carlo simulation is performed as described in Numerical Recipes (Press et al., 2007). For each metabolite, every time point in the time course of the unlabeled fraction is resampled from an assumed standard distribution with mean and standard deviation shown in **Supplemental Dataset 1**. The optimization is repeated with the resampled data for 1000 times. The obtained distribution of fluxes is used to determine the 95% confidence interval for each flux.

parameter	value
initial temperature	10.
minimal temperature	0.000001
factor of temperature decline	0.9
runs per temperature	200
standard deviation of noise	0.1

Supplemental Table M2: Parameters of the simulated annealing The second column lists the values for the parameters of the simulated annealing used to fit the model.

Supplemental Methods 6. Application to Central Carbon Metabolism

We applied extended KFP to the central carbon metabolism of C3-plants. The used pathway model comprises a part of the Calvin-Benson cycle and the pathway of starch synthesis, both located in the chloroplast, the photorespiration pathway, which takes place in different compartments, as well as the pathways of the synthesis of sucrose, trehalose and myo-inositol in the cytosol (see **Supplemental Figure M2A**). Furthermore, a branch to the amino-acid metabolism via 2PGA is considered in the setting of the equations. However, we note that in the model used for the estimation of fluxes this branch is constrained to zero.

From the considered pathway model, a system of differential equation is created, the solution of which gives the dynamic labeling behavior of all involved metabolic pools for a given flux distribution. The considered approach avoids the simulation of the transmission of labeled carbon atoms through the intermediates of the Calvin-Benson cycle. Instead the unlabeled in-flux of the carboxylation and the oxygenation of RuBP to the pools of 3PGA and glycine is modeled separately. These input models act as inhomogeneities of the differential equation system. The labeled carbon atoms are assumed to be randomly distributed between all possible position within a RuBP molecule. The further dynamics of the unlabeled fractions is described by extended KFP. The system is then fitted to time-resolved experimental data by using a simulated annealing approach (Kirkpatrick et al., 1983), followed by quasi-Newton optimization. The effect of partially labeled glycine molecules resulting in unlabeled serine molecules is neglected as the observed partially labeled fraction of glycine is low.

Note the difference between the model as it is implemented and the model used for the analysis. For the analysis some reactions are restricted to be irreversible and the flux via 2PGA towards amino acid metabolism is constrained to zero.

Treatment of experimental data

The unlabeled fraction is calculated from mass-spectrometric experimental data. The unlabeled metabolite content $x^u(t)$ is quantified by the mono-isotopic peak $\hat{x}_0(t)$. The total content (or pool size) of a metabolic pool $x^T(t)$ is calculated by the sum of the measured isotopic peaks $\hat{x}_i(t)$, as follows:

$$x^u(t) = \hat{x}_0(t) \quad (58)$$

$$x^T(t) = \sum_i \hat{x}_i(t). \quad (59)$$

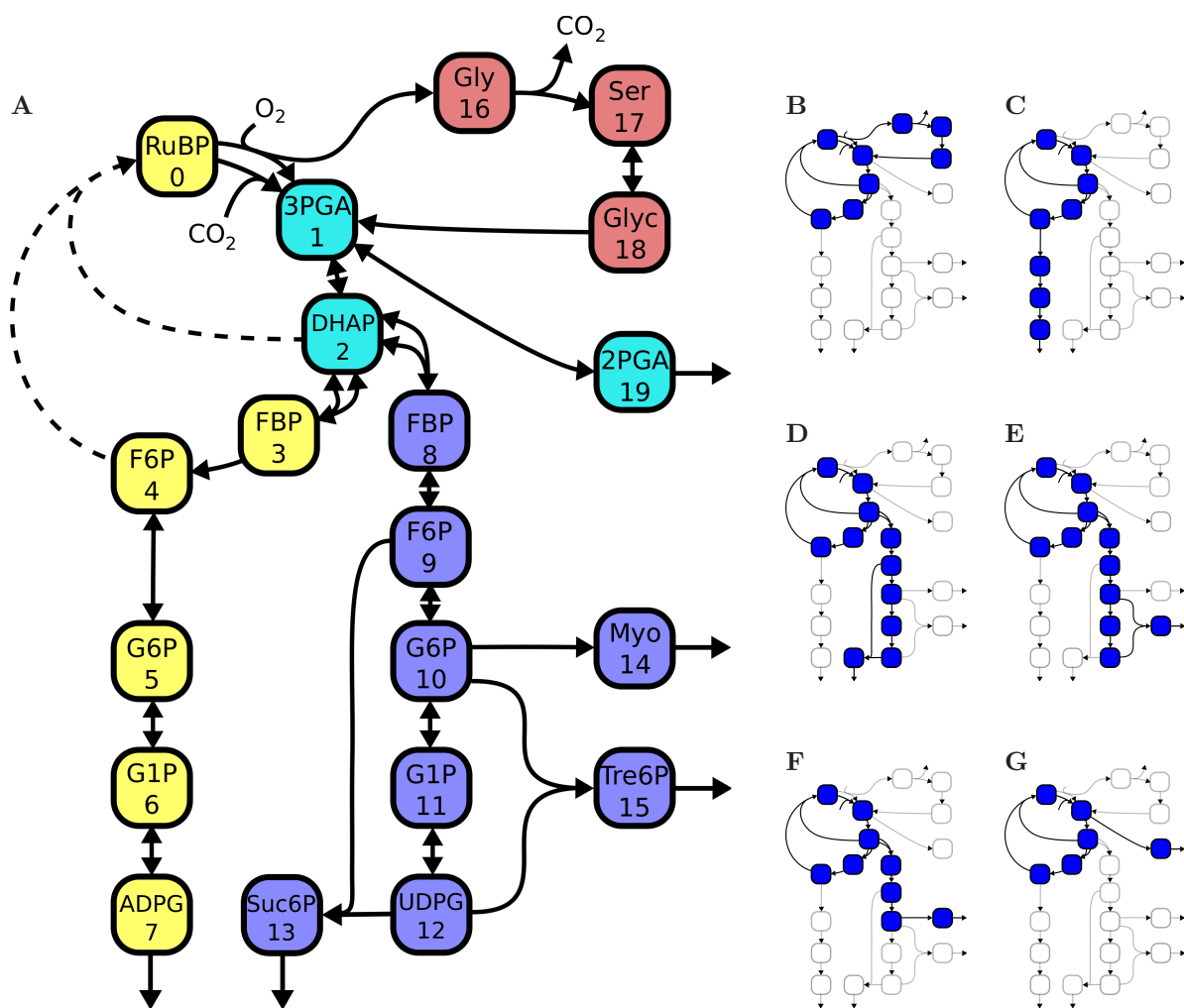
The unlabeled fraction \tilde{x} is then given by the ratio:

$$\tilde{x}(t) = \frac{x^u(t)}{x^T(t)} = \frac{\hat{x}_0(t)}{\sum_i \hat{x}_i(t)}. \quad (60)$$

In addition, the i -th mass-isotopic fraction can be calculated:

$$x^{(i)}(t) = \frac{x^{(i)}(t)}{x^T(t)} = \frac{\hat{x}_i(t)}{\sum_i \hat{x}_i(t)}. \quad (61)$$

The mass-spectrometric data are corrected for natural abundance of the isotopes (van Winden et al., 2002). Therefore, the metabolic pools are assumed to be completely unlabeled at the beginning of the experiment.



Supplemental Figure M2: Schematic representation of the pathway model and its modes (A) Pathway model with indices of metabolite (yellow - chloroplast, blue - cytosol, red - intermediates of photorespiration represented by one pool for each, gray - triosephosphates of chloroplast and cytosol in rapid equilibrium). (B-G) The 6 modes that generate the steady-state net flux distributions, (B) photorespiration, (C) starch, (D) sucrose, (E) trehalose, (F) myo-inositol, (G) amino acids. Each reversible reaction is additionally described by an exchange flux. Note, each metabolite is denoted by a number, which is used as index in the mathematical description of the model. In the actual implementation of the model, mode (G) is set to zero.

The phosphorylated hexoses, FBP, F6P, G6P, and G1P, are each modeled as two pools –one in the chloroplast, as components of the starch pathway, and the other one in the cytosol, as components of glycolysis. As only the sum of both pools can be measured via MS, non-aqueous-fractionation data is used to split the measured pool sizes of these metabolites into a total cytosolic and plastidic pool size. Non-aqueous-fractionation data, η , provide the proportion of a metabolites in the compartments. The pool sizes in the cytosol and plastid are calculated by the following:

$$x_{\text{pl.}}^T = \eta_{\text{pl.}}^X x^T, \text{ and} \quad (62)$$

$$x_{\text{cyt.}}^T = \eta_{\text{cyt.}}^X x^T. \quad (63)$$

The pathway model

The model includes some additional assumptions:

1. The intermediates of photorespiration glycine, serine, and glycerate are all modeled as one pool for each of them. Their compartmentalization is neglected.
2. The triosephosphates, 3PGA and DHAP, in cytosol and chloroplast are assumed to be in rapid equilibrium and are, therefore, also modeled as one pool for each of the two.
3. GAP is assumed to be in rapid equilibrium with DHAP and is of negligible content. As a result, it is not a part of the model, and its functions are approximated by those of DHAP (Stitt et al., 1983). The reactions:



are, therefore, lumped to:



Description of the steady-state flux distribution

All fluxes are constrained to metabolic steady state, given in Eq. (9). The distribution of net fluxes can be described by a positive linear combination of six independent modes, M^l , where:

$$\vec{F}^{\text{net}} = \sum_{l=1}^6 \phi_l \vec{M}^l. \quad (69)$$

Therefore, an individual net flux, $F_{i,j}^{\text{net}}$, between the pools of i and j is given by:

$$F_{i,j}^{\text{net}} = \sum_{l=1}^6 \phi_l M_{i,j}^l. \quad (70)$$

Each mode refers to one independent steady-state flux distribution, which satisfies the constraints of metabolic steady state. A mode can be understood as a possible route of a fixated carbon atom towards one of the out-flux of the system. Each mode comprises the Calvin-Benson cycle, including the carbon fixation by RuBisCo and the further pathway to one of the six out-fluxes of the system. The Calvin-Benson cycle has to be included to each mode, because part of the fixed carbon is used to regenerate RuBP to maintain the steady state. Therefore, 5 molecules of PGA are necessary to restore 3 molecules of RuBP for each molecule of 3PGA which effectively leaves the cycle.

The six modes are illustrated in **Supplemental Figure M2** and listed in **Supplemental Table M3**. They are denoted in units of carbon atoms participating in the corresponding reaction and are normalized in a way so that each out-flux from the system has a value of 1 carbon atom per second. In- and out-fluxes

are then given in terms of their fixed stoichiometric proportion to this flux. To use units of carbon atoms in the further description, all pool sizes need to also transformed to this unit. Therefore, all pool sizes in [mol molecules] are multiplied by the number of carbon atoms in the corresponding molecule.

For example: The mode M^1 describes the theoretical case that all fixated carbon atoms are lost via photorespiration. The oxidation of 2 molecules of RuBP (10 carbon atoms) results in 2 molecules of 3PGA (6 carbon atoms) and 2 molecules of glycine (4 carbon atoms). The corresponding flux $F_{(O_2,0),(1,16)}$ of the mode M^1 in **Supplemental Table M3**, therefore, has a value of 10. Both molecules of glycine form 1 molecule of serine (3 carbon atoms) and 1 molecules of CO_2 (1 carbon atom). As 4 carbon atoms are involved, $F_{16,(7,CO_2)}$ is 4. The flux to CO_2 has a value of 1 as posited. Serine reacts to glycerate, followed by a reaction to 2PGA. Altogether 3 molecules of 3PGA (9 carbon atoms) are formed. With an additional carboxylation of 1 molecule of RuBP (5 carbon atoms) and 1 molecule of CO_2 (1 carbon atom) to 2 molecules of 3PGA, 5 molecules of 3PGA (15 carbon atoms) can restore all 3 consumed molecules of RuBP. The flux of the carboxylation $F_{(CO_2,0),1}$ has a value of 6 carbon atoms. The out-flux of 3PGA $F_{1,2}$ is equal to its in-flux of 15 carbon atoms, coming from RuBP and glycerate. This flux of 15 carbon atoms then splits in a flux $F_{2,0}$ from DHAP to RuBP of 9 atoms and fluxes to RuBP via FBP and F6P of 6 atoms: $F_{2,3}$, $F_{3,4}$ and $F_{4,0}$.

If the model only comprises irreversible reaction, all possible flux distributions can be described by six parameters ϕ_l . Each additional exchange flux $F_{i,j}^{\text{ex}}$ introduces one more parameter. An exchange flux could also be understood as a mode \vec{M}^{ex} of its own, describing a futile cycle between metabolites, which does not contribute to a net flux or any other flux of the network. With the assumption that net fluxes are positive, forward fluxes, $F_{i,j}$, and backward fluxes, $F_{j,i}$, from metabolite i to metabolites j can be expressed as:

$$\begin{aligned} F_{i,j} &= F_{i,j}^{\text{net}} + F_{i,j}^{\text{ex}} \\ &= \sum_{l=1}^6 \phi_l M_{i,j}^l + F_{i,j}^{\text{ex}} \\ &= \sum_{l=1}^6 \phi_l M_{i,j}^l + \varphi_{i,j} M_{i,j}^{\text{ex}}, \end{aligned} \quad (71)$$

and

$$F_{j,i} = F_{i,j}^{\text{ex}} = \varphi_{i,j} M_{i,j}^{\text{ex}}. \quad (72)$$

To express all parameters in a consistent way, M^{ex} has a value of 1 [carbon atom per second] and $\varphi_{i,j}$, like ϕ^l , is unit-less.

In principle the consideration of reversible reaction can introduce additional futile cycle, which comprise more than one reaction. In this model such cycles do not occur.

In addition the parameter $\varphi_{i,j}$ can be hyperbolically transformed (Wiechert and De Graaf, 1997).

The input models

In the model, the unlabeled in-flux to the pools of 3PGA and glycine via the carboxylation and oxygenation of RuBP are assumed to be known and modeled independently. CO_2 is assumed to be completely labeled at $t = 0$ and described by:

$$\tilde{x}_{CO_2}(t) = 0, \text{ for } t > 0. \quad (73)$$

The unlabeled in-fluxes $f_{X,r}^{\text{in}}$ to the pools of X via reaction r is described by the product of the metabolic steady-state flux $F_{X,r}^{\text{in}}$ and its unlabeled fraction $h_{X,r}^{\text{in}}$:

$$f_{X,r}^{\text{in}}(t) = F_{X,r}^{\text{in}} h_{X,r}^{\text{in}}(t). \quad (74)$$

For a reaction with one product molecule the unlabeled fraction of the in-flux $h_{X,r}^{\text{in}}(t)$ is given in the extend KFP by the product of the unlabeled fraction of the substrates (see Eq.(14)). The unlabeled

	photores.	starch	sucrose	trehalose	myo-inositol	2PGA
flux	M^1	M^2	M^3	M^4	M^5	M^6
$F_{(0,CO_2),1}$	6	6	6	6	6	6
$F_{0,1}$	5	5	5	5	5	5
$F_{CO_2,1}$	1	1	1	1	1	1
$F_{(0,O_2),(1,16)}$	10	0	0	0	0	0
$F_{0,1}$	6	0	0	0	0	0
$F_{0,16}$	4	0	0	0	0	0
$F_{1,2}$	15	6	6	6	6	5
$F_{2,3}$	6	3	2	2	2	2
$F_{2,0}$	9	3	3	3	3	3
$F_{3,4}$	6	3	2	2	2	2
$F_{4,5}$	0	1	0	0	0	0
$F_{4,0}$	6	2	2	2	2	2
$F_{5,6}$	0	1	0	0	0	0
$F_{6,7}$	0	1	0	0	0	0
$F_{7,O}$	0	1	0	0	0	0
$F_{2,8}$	0	0	1	1	1	0
$F_{8,9}$	0	0	1	1	1	0
$F_{9,10}$	0	0	$\frac{1}{2}$	1	1	0
$F_{10,11}$	0	0	$\frac{1}{2}$	$\frac{1}{2}$	0	0
$F_{11,12}$	0	0	$\frac{1}{2}$	$\frac{1}{2}$	0	0
$F_{(9,12),13}$	0	0	1	0	0	0
$F_{9,13}$	0	0	$\frac{1}{2}$	0	0	0
$F_{12,13}$	0	0	$\frac{1}{2}$	0	0	0
$F_{13,O}$	0	0	1	0	0	0
$F_{10,14}$	0	0	0	0	1	0
$F_{14,O}$	0	0	0	0	1	0
$F_{(10,12),15}$	0	0	0	1	0	0
$F_{10,15}$	0	0	0	$\frac{1}{2}$	0	0
$F_{12,15}$	0	0	0	$\frac{1}{2}$	0	0
$F_{15,O}$	0	0	0	1	0	0
$F_{16,(17,CO_2)}$	4	0	0	0	0	0
$F_{16,O}$	1	0	0	0	0	0
$F_{16,17}$	3	0	0	0	0	0
$F_{17,18}$	3	0	0	0	0	0
$F_{18,1}$	3	0	0	0	0	0
$F_{1,19}$	0	0	0	0	0	1
$F_{19,O}$	0	0	0	0	0	1

Supplemental Table M3: Composition of elementary flux modes. The modes M^1 - M^6 are expressed in units of carbon atoms. See **Supplemental Figure M2** and **Supplemental Table M5** for definition of fluxes. Indented fluxes correspond to an in- or out-flux from of a pool of a multi-molecular reaction. The environment of the system is denoted by O , which appears as an index in the out-fluxes of the system.

in-fluxes to 3PGA and glycine via the carboxylation and oxygenation of RuBP:



do not exclusively depend on the unlabeled fraction of RuBP. Unlabeled product molecules can spawn from partially labeled RuBP molecules, thus the contribution of higher mass-isotopomers have to be taken into account. We assume a random distribution of label between all possible labeling positions for all relevant mass-isotopomers of RuBP at all times. Following this assumption, a proper input model for the unlabeled fraction of the in-fluxes $h_{X,r}^{\text{in}}(t)$ is chosen and its parameters are estimated from the available data. The assumption is driven by the high turn-over rate and the complexity of the Calvin-Benson cycle.

In the following the approach is illustrated for the unlabeled in-fluxes to 3PGA via the oxygenation of RuBP. In this reaction a molecule of RuBP (five C atoms) reacts with a molecule of O_2 to a molecule of 3PGA (three C atoms) and a molecule of glycine (two C atoms). Unlabeled RuBP molecules result in unlabeled products. RuBP molecules with one or two labeled carbon atoms result in an unlabeled 3PGA molecule, if the particular three carbon atoms, forming the 3PGA molecule, are unlabeled. Assuming a random distribution of the label with all possible labeling positions in RuBP, the fraction of resulting unlabeled product molecule can be calculated. They are given by the number of permutations of positional labeling pattern resulting in an unlabeled product to the number of all possible permutations in the substrate molecule. For example, if a RuBP molecule has one labeled carbon atom, there are five possible labeling positions. Three particular carbon atoms result in a 3PGA molecule. The probability that these three carbon atoms are unlabeled is given by 2 to 5. The unlabeled fraction of the in-flux to 3PGA and glycine via the RuBP-oxygenation can be expressed as:

$$h_{3\text{PGA},\text{oxy.}}^{\text{in}}(t) = \sum_{i=0}^5 \theta_{3\text{PGA},\text{oxy.}}^{(i)} \tilde{x}_{\text{RuBP}}^{(i)}(t), \quad (77)$$

$$h_{\text{gly},\text{oxy.}}^{\text{in}}(t) = \sum_{i=0}^5 \theta_{\text{gly},\text{oxy.}}^{(i)} \tilde{x}_{\text{RuBP}}^{(i)}(t). \quad (78)$$

The i -th mass-isotopic fraction of RuBP is denoted by $\tilde{x}_{\text{RuBP}}^{(i)}$. The corresponding fraction resulting in unlabeled products is expressed as $\theta^{(i)}$. Similar consideration lead to the expression for the fraction of the unlabeled in-flux to 3PGA via the RuBP carboxylation. Each of the two 3PGA molecules have to be treated separately. One of the 3PGA molecules is always labeled due to the assumption of fully labeled CO_2 . The fraction of the unlabeled in-flux via the second molecule is described by:

$$h_{3\text{PGA},\text{carb.}}^{\text{in}}(t) = \sum_{i=0}^5 \theta_{3\text{PGA},\text{carb.}}^{(i)} \tilde{x}_{\text{RuBP}}^{(i)}(t). \quad (79)$$

The values for all θ 's are listed in **Supplemental Table M4**.

h^{in}	$\theta^{(0)}$	$\theta^{(1)}$	$\theta^{(2)}$	$\theta^{(3)}$	$\theta^{(4)}$	$\theta^{(5)}$
$h_{3\text{PGA},\text{carb.}}^{\text{in}}$	1	0.4	0.1	0	0	0
$h_{3\text{PGA},\text{oxy.}}^{\text{in}}$	1	0.4	0.1	0	0	0
$h_{\text{gly},\text{oxy.}}^{\text{in}}$	1	0.6	0.3	0.1	0	0

Supplemental Table M4: Fractions θ . The table includes the fractions θ which generate unlabeled products from mass-isotopic fraction of RuBP.

The Eqs.(77)-(79) relate the unlabeled in-fluxes with experimental data. The fraction of the unlabeled in-fluxes is approximated by a linear combination of two exponential functions:

$$h^{\text{in}} \simeq h^{\text{input}} = Ae^{-at} + Be^{-bt} \text{ where } A + B = 1. \quad (80)$$

We refer to it as the input model for the corresponding in-flux. Each input model h^{input} is fitted to the experimental data of $h^{\text{in}}(t)$ using a quasi-Newton method to minimize to variance-weighted sum of

residual. Following this, the dynamic labeling behavior of the in-fluxes to 3PGA (via the carboxylase and oxygenase reactions) and glycine (via the oxygenase reaction) can be calculated.

Note, although intermediate of the Calvin-Benson cycle are not simulated in the system of differential equation, they still are consider for the steady-state flux distribution.

Implementation of the system of differential equations

The system of ordinary differential equations is shown in Eqs. (82) - (111). To simplify the notation, the substitution:

$$\tilde{x}_m = \frac{x_m^u}{x_m^T} \quad (81)$$

is used. The indices refer to special metabolites as shown in **Supplemental Figure M2**. The input models $h_{3\text{PGA},\text{oxy.}}^{\text{input}}$, $h_{3\text{PGA},\text{carb.}}^{\text{input}}$ and $h_{\text{gly},\text{oxy.}}^{\text{input}}$ are given in Eq. (80) and denoted as in the corresponding section. All fluxes are denoted in fluxes of carbon atoms participating in a reaction, what influences the factor in several equations.

$$\begin{aligned} 3\text{PGA} : \quad x_1^T \frac{d\tilde{x}_1}{dt} &= \frac{3}{5} F_{(O_2,0),(1,16)} h_{3\text{PGA},\text{oxy.}}^{\text{input}} + \frac{1}{2} F_{(CO_2,0),(1)} h_{3\text{PGA},\text{carb.}}^{\text{input}} \\ &\quad + F_{18,1} \tilde{x}_{18} + F_{2,1} \tilde{x}_2 + F_{19,1} \tilde{x}_9 \\ &\quad - (F_{1,2} + F_{1,19}) \tilde{x}_1 \end{aligned} \quad (82)$$

$$\text{DHAP} : x_2^T \frac{d\tilde{x}_2}{dt} = F_{1,2} \tilde{x}_1 + F_{3,2} \left(\tilde{x}_3 + \frac{1}{2} \tilde{x}_3^* \right) + F_{8,2} \left(\tilde{x}_8 + \frac{1}{2} \tilde{x}_8^* \right) \quad (83)$$

$$- (F_{2,3} + F_{2,8} + F_{2,0} + F_{2,1}) \tilde{x}_2 \quad (84)$$

$$\text{FBP}_{\text{pl.}} : x_3^T \frac{d\tilde{x}_3}{dt} = F_{2,3} (\tilde{x}_2)^2 - (F_{3,4} + F_{3,2}) \tilde{x}_2 \quad (85)$$

$$x_3^T \frac{d\tilde{x}_3^*}{dt} = 2F_{2,3} \tilde{x}_2 (1 - \tilde{x}_2) - (F_{3,4} + F_{3,2}) \tilde{x}_2^* \quad (86)$$

$$\text{F6P}_{\text{pl.}} : x_4^T \frac{d\tilde{x}_4}{dt} = F_{3,4} \tilde{x}_3 - (F_{4,5} + F_{4,0}) \tilde{x}_4 \quad (87)$$

$$\text{G6P}_{\text{pl.}} : x_5^T \frac{d\tilde{x}_5}{dt} = F_{4,5} \tilde{x}_4 + F_{6,5} \tilde{x}_6 - (F_{5,6} + F_{5,4}) \tilde{x}_5 \quad (88)$$

$$\text{G1P}_{\text{pl.}} : x_6^T \frac{d\tilde{x}_6}{dt} = F_{5,6} \tilde{x}_5 + F_{7,6} \tilde{x}_6 - (F_{6,7} + F_{6,5}) \tilde{x}_6 \quad (89)$$

$$\text{ADPG} : x_7^T \frac{d\tilde{x}_7}{dt} = F_{6,7} \tilde{x}_6 - (F_{7,0} + F_{7,6}) \tilde{x}_7 \quad (90)$$

$$\text{FBP}_{\text{cyt.}} : x_8^T \frac{d\tilde{x}_8}{dt} = F_{2,8} (\tilde{x}_2)^2 + F_{9,8} \tilde{x}_9 - (F_{8,9} + F_{8,2}) \tilde{x}_8 \quad (91)$$

$$x_8^T \frac{d\tilde{x}_8^*}{dt} = 2F_{2,8} \tilde{x}_2 (1 - \tilde{x}_2) + F_{9,8} \tilde{x}_9^* - (F_{8,9} + F_{8,2}) \tilde{x}_8^* \quad (92)$$

$$\text{F6P}_{\text{cyt.}} : x_9^T \frac{d\tilde{x}_9}{dt} = F_{8,9} \tilde{x}_8 + F_{10,9} \tilde{x}_{10} - (F_{9,10} + F_{9,13} + F_{9,8}) \tilde{x}_9 \quad (93)$$

$$x_9^T \frac{d\tilde{x}_9^*}{dt} = F_{8,9} \tilde{x}_8^* + F_{10,9} \tilde{x}_{10}^* - (F_{9,10} + F_{9,13} + F_{9,8}) \tilde{x}_9^* \quad (94)$$

$$\text{G6P}_{\text{cyt.}} : x_{10}^T \frac{d\tilde{x}_{10}}{dt} = F_{9,10} \tilde{x}_9 + F_{11,10} \tilde{x}_{11} \quad (95)$$

$$- (F_{10,11} + F_{10,14} + F_{10,9} + F_{10,15}) \tilde{x}_{10} \quad (96)$$

$$x_{10}^T \frac{d\tilde{x}_{10}^*}{dt} = F_{9,10} \tilde{x}_9^* + F_{11,10} \tilde{x}_{11}^* \quad (97)$$

$$- (F_{10,11} + F_{10,14} + F_{10,9} + F_{10,15}) \tilde{x}_{10}^* \quad (98)$$

$$\text{G1P}_{\text{cyt.}} : x_{11}^T \frac{d\tilde{x}_{11}}{dt} = F_{10,11} \tilde{x}_{10} + F_{12,11} \tilde{x}_{12} \quad (99)$$

$$- (F_{11,12} + F_{11,10}) \tilde{x}_{11} \quad (100)$$

$$x_{11}^T \frac{d\tilde{x}_{11}^*}{dt} = F_{10,11}\tilde{x}_{10}^* + F_{12,11}\tilde{x}_{12}^* \quad (101)$$

$$- (F_{11,12} + F_{11,10})\tilde{x}_{11}^* \quad (102)$$

$$\text{UDPG} : x_{12}^T \frac{d\tilde{x}_{12}}{dt} = F_{11,12}\tilde{x}_{11} - (F_{12,13} + F_{12,15} + F_{12,11})\tilde{x}_{11} \quad (103)$$

$$x_{12}^T \frac{d\tilde{x}_{12}^*}{dt} = F_{11,12}\tilde{x}_{11}^* - (F_{12,13} + F_{12,15} + F_{12,11})\tilde{x}_{11}^* \quad (104)$$

$$\text{Suc6P} : x_{13}^T \frac{d\tilde{x}_{13}}{dt} = F_{(9,12),13}\tilde{x}_9\tilde{x}_{12} - F_{13,0}\tilde{x}_{13} \quad (105)$$

$$\text{myo-Inositol} : x_{14}^T \frac{d\tilde{x}_{14}}{dt} = F_{10,14}\tilde{x}_{10} - F_{14,0}\tilde{x}_{14} \quad (106)$$

$$\text{Tre6P} : x_{15}^T \frac{d\tilde{x}_{15}}{dt} = F_{(10,12),15}\tilde{x}_{10}\tilde{x}_{12} - F_{15,0}\tilde{x}_{15} \quad (107)$$

$$\text{Glycine} : x_{16}^T \frac{d\tilde{x}_{16}}{dt} = \frac{2}{5}F_{(O_2,0),(1,16)}h_{\text{gly,oxy.}}^{\text{input}} - F_{16,(CO_2,17)}\tilde{x}_{16} \quad (108)$$

$$\text{Serine} : x_{17}^T \frac{d\tilde{x}_{17}}{dt} = \frac{3}{4}F_{16,(CO_2,17)}(\tilde{x}_{16})^2 + F_{18,17}\tilde{x}_{18} - F_{17,18}\tilde{x}_{17} \quad (109)$$

$$\text{Glycerate} : x_{18}^T \frac{d\tilde{x}_{18}}{dt} = F_{17,18}\tilde{x}_{17} - (F_{18,1} + F_{18,17})\tilde{x}_{18} \quad (110)$$

$$2\text{PGA} : x_{19}^T \frac{d\tilde{x}_{19}}{dt} = F_{1,19}\tilde{x}_1 - (F_{19,0} + F_{19,1})\tilde{x}_{19} \quad (111)$$

Some reactions are assumed to be irreversible. The corresponding backward fluxes are not included in the system of differential equations. The irreversibility of all reactions is listed in **Supplemental Table M5** and illustrated in **Supplemental Figure M3A**. In the following, additional explanations about the equation system are provided:

1. To treat the reversibility of the bi-molecular reaction:



in both compartments, partially labeled pools are included in the model. In this case a partially labeled molecule is created by the reaction of a labeled molecule of DHAP with an unlabeled molecule of DHAP. A partially labeled molecule of FBP, therefore, is defined as consisting of an unlabeled and labeled part. Via the reverse reaction, one unlabeled molecule of DHAP is then created from a partially labeled molecule of FBP. Such a partially labeled molecule of FBP can react further on downstream the pathway to UDPG. If all reactions in between were reversible, the partially labeled molecule could find its way back to the pool of FBP. Therefore, partially labeled pools are included for all successors of the bio-molecular reaction until an irreversible reaction is encountered. Partially labeled pools are included for $\text{FBP}_{\text{pl.}}$, $\text{FBP}_{\text{cyt.}}$, $\text{F6P}_{\text{cyt.}}$, $\text{G6P}_{\text{cyt.}}$, $\text{G1P}_{\text{cyt.}}$ and UDPG. They are denoted as \tilde{x}_m^* . Note that the partially labeled in-flux from DHAP to FBP is given by:

$$f_{2,w}^{\text{in}*} = 2F_{2,w}^{\text{in}}\tilde{x}_2(1 - \tilde{x}_2), \quad (113)$$

as $(1 - \tilde{x}_m)$ denotes the labeled fraction of m . The factor takes in consideration that either the first or the second molecule of DHAP is labeled and occurs in Eqs. (86) and (92). The corresponding reverse reaction from a partially labeled molecule of FBP to one of DHAP needs a factor of $\frac{1}{2}$ since both labeled and unlabeled DHAP molecules are formed (Eq. (83)).

2. In Eq. (82), for 3PGA, the flux of the RuBP oxygenation $F_{(O_2,0),(1,16)}$ has an factor of $\frac{3}{5}$, as only 3 carbon atoms react to 1 molecule of 3PGA. The remaining 2 carbon atoms appear in the in-flux to the glycine pool, in Eq. (108). The flux of the RuBP carboxylation $F_{(CO_2,0),(1)}$ has a factor of $\frac{1}{2}$, because CO_2 is assumed to always be completely labeled. Therefore, only one unlabeled molecule of 3PGA is produced, if an unlabeled molecule of RuBP reacts with an labeled molecule of CO_2 .

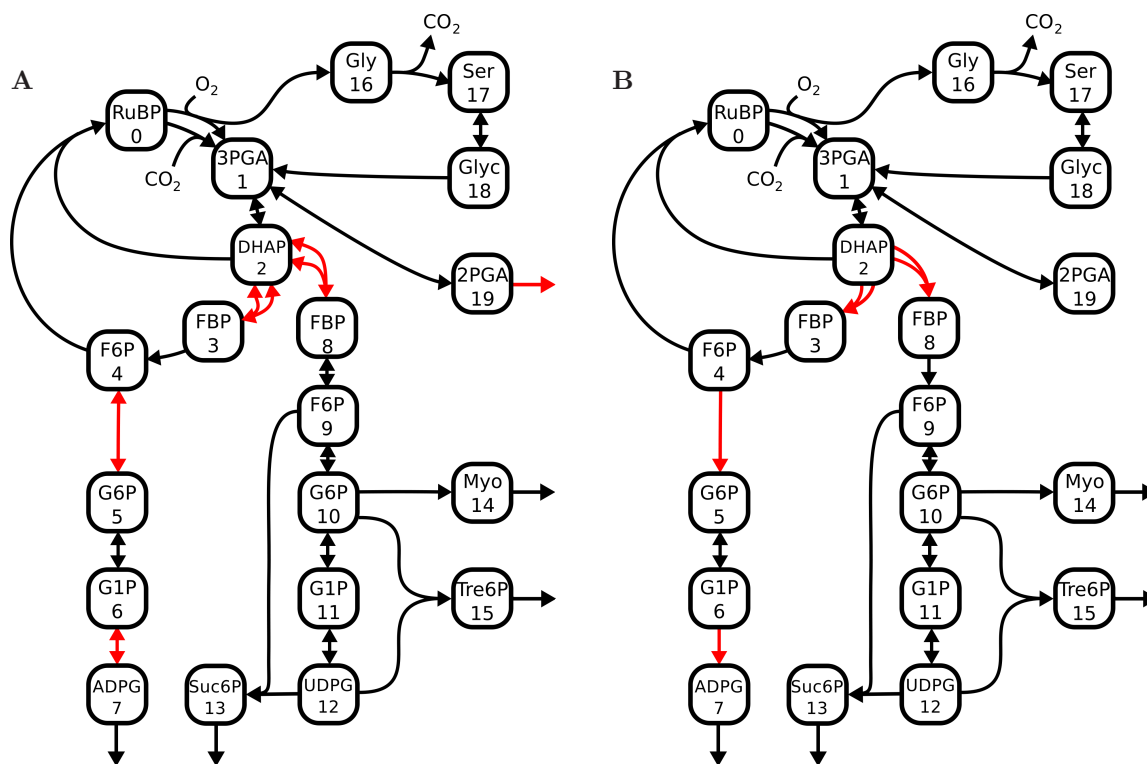
reaction			flux
⁵ RuBP	+ ¹ CO ₂	⁶ → 2 ³ 3PGA	$F_{(0,\text{CO}_2),(1)}$
⁵ RuBP	+ ⁰ O ₂	⁵ → ³ 3PGA	+ ² Glycine $F_{(0,\text{O}_2),(1,16)}$
³ 3PGA		³ ↔ ³ DHAP	$F_{1,2}$
2 ³ DHAP		⁶ ↔ ⁶ FBP _{pl.}	$F_{2,3}$
⁶ FBP _{pl.}		⁶ → ⁶ F6P _{pl.}	$F_{3,4}$
⁶ F6P _{pl.}		⁶ ↔ ⁶ G6P _{pl.}	$F_{4,5}$
⁶ G6P _{pl.}		⁶ ↔ ⁶ G1P _{pl.}	$F_{5,6}$
⁶ G1P _{pl.}		⁶ ↔ ⁶ ADPG	$F_{6,7}$
⁶ ADPG		⁶ → O	$F_{7,O}$
2 ³ DHAP		⁶ ↔ ⁶ FBP _{cyt.}	$F_{2,8}$
⁶ FBP _{cyt.}		⁶ ↔ ⁶ F6P _{cyt.}	$F_{8,9}$
⁶ F6P _{cyt.}		⁶ ↔ ⁶ G6P _{cyt.}	$F_{9,10}$
⁶ G6P _{cyt.}		⁶ ↔ ⁶ G1P _{cyt.}	$F_{10,11}$
⁶ G1P _{cyt.}		⁶ ↔ ⁶ UDPG	$F_{11,12}$
⁶ F6P _{cyt.}	+ ⁶ UDPG	¹² → ¹² Suc6P	$F_{(9,12),13}$
¹² Suc6P		¹² → O	$F_{13,O}$
⁶ G1P _{cyt.}		⁶ → ⁶ Myo	$F_{10,14}$
⁶ Myo		⁶ → O	$F_{14,O}$
⁶ G6P _{cyt.}	+ ⁶ UDPG	¹² → ¹² Tre6P	$F_{(10,12),15}$
¹² Tre6P		¹² → O	$F_{15,O}$
2 ² Glycine		⁴ → ³ Serine	+ ¹ CO ₂ $F_{16,(17,\text{CO}_2)}$
³ Serine		³ ↔ ³ Glycerate	$F_{17,18}$
³ Glycerate		³ → ³ 3PGA	$F_{18,1}$
³ 3PGA		³ ↔ ³ 2PGA	$F_{1,19}$
³ 2PGA		³ → O	$F_{19,O}$

Supplemental Table M5: Reactions in the model and notation of corresponding flux in carbon atoms participating in each modeled reaction as implemented. The number above a metabolite indicates the number of carbon atoms in the metabolite. The number above an arrow indicates the number of carbon atoms participating in the reaction. An out-flux of the system is denoted by O used as an index. The indices correspond to those appearing below the metabolite names in **Supplemental Figure M2**

3. The flux $F_{16,(CO_2,17)}$ of the reaction in which 2 molecules of glycine are transformed to 1 molecule of serine appears in Eq. (108) as an out-flux with factor 1 since 4 involved carbon atoms leave the glycine pool. This flux has a factor of $\frac{3}{4}$ in Eq. (109), because of the 4 carbon atoms in 2 glycine molecules that enter the glycine decarboxylase reaction, 1 carbon atom leaves the reaction as CO_2 , and 3 carbon atoms as a molecule of serine.

Exact model used for analysis

For the analysis of the mass-spectrometric data a simplification of the model is used. Some reactions are assumed to be irreversible (see **Supplemental Figure M3**). The elementary flux mode via 2PGA is constraint to zero. Therefore, only 12 independent parameter remain in the model. The net flux distribution is described by 5 parameters ϕ and the exchange fluxes by 7 parameters φ .



Supplemental Figure M3: Model representations. (A) The model from which the system of ordinary differential equations is established; (B) Schematic view of the model together with the assumptions used in the analysis. Irreversible reactions are shown with single-arrow lines, while reversible reactions are depicted by double-arrow lines. Differences are shown in red.

Supplemental References

- Antoniewicz, M. R., Stephanopoulos, G., and Kelleher, J. K. (2006). Evaluation of regression models in metabolic physiology: predicting fluxes from isotopic data without knowledge of the pathway. *Metabolomics*, 2(1):41–52.
- Arrivault, S., Guenther, M., Ivakov, A., Feil, R., Vosloh, D., van Dongen, J. T., Sulpice, R., and Stitt, M. (2009). Use of reverse-phase liquid chromatography, linked to tandem mass spectrometry, to profile the Calvin cycle and other metabolic intermediates in Arabidopsis rosettes at different carbon dioxide concentrations. *The Plant Journal*, 59(5):826–39.
- Bauwe, H., Hagemann, M., and Fernie, A. R. (2010). Photorespiration: players, partners and origin. *Trends in Plant Science*, 15(6):330–336.
- Bialeski, R. L. (1973). Phosphate Pools, Phosphate Transport, and Phosphate Availability. *Annual Review of Plant Physiology*, 24(1):225–252.
- Brockwell, P. J. and Davis, R. A. (2006). *Time Series: Theory and Methods*. Springer, New York, 2nd edition.
- Bronshtein, I. N., Semendyayev, K. A., and Musiol, G. (2007). *Handbook of Mathematics*. Springer.
- Byrd, R. H., Lu, P., Nocedal, J., and Zhu, C. (1995). A Limited Memory Algorithm for Bound Constrained Optimization. *SIAM Journal on Scientific Computing*, 16(5):1190.
- Cegelski, L. and Schaefer, J. (2005). Glycine Metabolism in Intact Leaves by in Vivo ^{13}C and ^{15}N Labeling. *Journal of Biological Chemistry*, 280(47):39238–39245.
- Chong, E. K. P. and Zak, S. H. (2008). *An Introduction to Optimization*. John Wiley & Sons, Inc., New Jersey, 3rd edition.
- Cournac, L., Peltier, G., and Havaux, M. (2002). Cyclic Electron Flow around Photosystem I in C₃ Plants. In Vivo Control by the Redox State of Chloroplasts and Involvement of the NADH-Dehydrogenase Complex. *Plant Physiology*, 128:760–769.
- Ernst, E. and Gerhard, W. (1996). *Solving ordinary differential equations II: Stiff and differential-algebraic problems*. Springer, Berlin, 2nd edition.
- Fischer, E., Zamboni, N., and Sauer, U. (2004). High-throughput metabolic flux analysis based on gas chromatography – mass spectrometry derived ^{13}C constraints. *Analytical Biochemistry*, 325:308–316.
- Fliege, R., Flüge, U. I., Werdan, K., and Heldt, H. W. (1978). Specific transport of inorganic phosphate, 3-phosphoglycerate and triosephosphates across the inner membrane of the envelope in spinach chloroplasts. *Biochimica et Biophysica Acta*, 502(2):232–247.
- Gerhardt, R. and Heldt, H. W. (1984). Measurement of Subcellular Metabolite Levels in Leaves by Fractionation of Freeze-Stopped Material in Nonaqueous Media. *Plant Physiology*, 75(3):542–547.
- Gerhardt, R., Stitt, M., and Heldt, H. W. (1987). Subcellular Metabolite Levels in Spinach Leaves. *Plant Physiology*, 83(2):399–407.
- Heinrich, R. and Schuster, S. (1996). *The regulation of cellular systems*. Chapman & Hall, New York, 1st edition.
- Hindmarsh, A. C. (1983). ODEPACK, A systematized collection of ODE solvers. *Scientific Computing*, 1:55–64.
- Katz, J. and Wood, G. (1960). The Use of Glucose- ^{14}C for the Evaluation Pathways of Glucose Metabolism. *The Journal of Biological Chemistry*, 235(8):2165–2177.
- Kirkpatrick, S., Gelatt, C. D., and Vecchi, M. P. (1983). Optimization by simulated annealing. *Science*, 220(4598):671–680.

- Mason, G. F. and Rothman, D. L. (2004). Basic principles of metabolic modeling of NMR ^{13}C isotopic turnover to determine rates of brain metabolism in vivo. *Metabolic Engineering*, 6:75–84.
- Maxwell, P. C. and Biggins, J. (1976). Role of cyclic electron transport in photosynthesis as measured by the photoinduced turnover of P700 in vivo. *Biochemistry*, 15(18):3975–3981.
- Mu, F., Williams, R. F., Unkefer, C. J., Unkefer, P. J., Faeder, J. R., and Hlavacek, W. S. (2007). Carbon-fate maps for metabolic reactions. *Bioinformatics*, 23(23):3193–9.
- Papin, J. A., Stelling, J., Price, N. D., Klamt, S., Schuster, S., and Palsson, B. O. (2004). Comparison of network-based pathway analysis methods. *Trends in Biotechnology*, 22(8):400–5.
- Petzold, L. (1983). Automatic Selection of Methods for Solving Stiff and Nonstiff Systems of Ordinary Differential Equations. *SIAM Journal on Scientific and Statistical Computing*, 4(1):136–148.
- Press, W. H., Teukolsky, S. A., Vetterling, W. T., and Flannery, B. P. (2007). Numerical Recipes. The Art of Scientific Computing. chapter 15. Cambridge Press, 3rd edition.
- Ravikirthi, P., Suthers, P. F., and Maranas, C. D. (2011). Construction of an E. Coli Genome-Scale Atom Mapping Model for MFA Calculations. *Biotechnology and Bioengineering*, 108(6):1372–1382.
- Sauer, U. (2006). Metabolic networks in motion: ^{13}C -based flux analysis. *Molecular Systems Biology*, 2:62.
- Schilling, C. H., Letscher, D., and Palsson, B. O. (2000). Theory for the systemic definition of metabolic pathways and their use in interpreting metabolic function from a pathway-oriented perspective. *Journal of Theoretical Biology*, 203(3):229–48.
- Schmidt, K., Carlson, M., Nielson, J., and Villadsen, J. (1997). Modeling isotopomer distributions in biochemical networks using isotopomer mapping matrices. *Biotechnology and Bioengineering*, 55(6):831–840.
- Schuster, S., Dandekar, T., and Fell, D. A. (1999). Detection of elementary flux modes in biochemical networks: a promising tool for pathway analysis and metabolic engineering. *Trends in Biotechnology*, 17(2):53–60.
- Selivanov, V. a., Sukhomlin, T., Centelles, J. J., Lee, P. W. N., and Cascante, M. (2006). Integration of enzyme kinetic models and isotopomer distribution analysis for studies of in situ cell operation. *BMC Neuroscience*, 7 Suppl 1:S7.
- Stitt, M. (1987). Fructose 2,6-Bisphosphate and Plant Carbohydrate Metabolism. *Plant Physiology*, 84(2):201–204.
- Stitt, M., Lunn, J., and Usadel, B. (2010). Arabidopsis and primary photosynthetic metabolism - more than the icing on the cake. *The Plant Journal*, 61(6):1067–91.
- Stitt, M., McLilley, R., Gerhardt, R., and Heldt, H. W. (1989). Metabolite levels in specific cells and subcellular compartments of plant leaves. *Methods in Enzymology*, 174:518–550.
- Stitt, M., Wirtz, W., and Heldt, H. (1980). Metabolite levels during induction in the chloroplast and extra chloroplast compartments of spinach protoplasts. *Biochimica et Biophysica Acta*, 593:85–102.
- Stitt, M., Wirtz, W., and Heldt, H. W. (1983). Regulation of Sucrose Synthesis by Cytoplasmic Fructose-bisphosphatase and Sucrose Phosphate Synthase during Photosynthesis in Varying Light and Carbon Dioxide. *Plant Physiology*, 72(3):767–774.
- van Winden, W. A., Wittmann, C., Heinzle, E., and Heijnen, J. J. (2002). Correcting mass isotopomer distributions for naturally occurring isotopes. *Biotechnology and Bioengineering*, 80(4):477–479.
- Wahl, S. A., Nöh, K., and Wiechert, W. (2008). ^{13}C labeling experiments at metabolic nonstationary conditions: an exploratory study. *BMC Bioinformatics*, 9:152.

- Wiechert, W. and De Graaf, A. A. (1997). Bidirectional reaction steps in metabolic networks: I. Modeling and simulation of carbon isotope labeling experiments. *Biotechnology and Bioengineering*, 55(1):101–117.
- Wiechert, W., Möllney, M., Isermann, N., Wurzel, M., and de Graaf, a. a. (1999). Bidirectional reaction steps in metabolic networks: III. Explicit solution and analysis of isotopomer labeling systems. *Biotechnology and Bioengineering*, 66(2):69–85.
- Young, J. D., Shastri, A. a., Stephanopoulos, G., and Morgan, J. a. (2011). Mapping photoautotrophic metabolism with isotopically nonstationary (13)C flux analysis. *Metabolic Engineering*, 13(6):656–665.
- Young, J. D., Walther, J. L., Antoniewicz, M. R., and Yoo, H. (2008). An Elementary Metabolite Unit (EMU) Based Method of Isotopically Nonstationary Flux Analysis. *Biotechnology*, 99(3):686–699.
- Yuan, J., Bennett, B. D., and Rabinowitz, J. D. (2008). Kinetic flux profiling for quantitation of cellular metabolic fluxes. *Nature Protocols*, 3(8):1328–1340.
- Yuan, J., Fowler, W. U., Kimball, E., Lu, W., and Rabinowitz, J. D. (2006). Kinetic flux profiling of nitrogen assimilation in Escherichia coli. *Nature Chemical Biology*, 2(10):529–530.
- Zeeman, S. C., Smith, S. M., and Smith, A. M. (2007). The diurnal metabolism of leaf starch. *Biochemical Journal*, 401(1):13–28.
- Zhu, C., Byrd, R. H., Lu, P., and Nocedal, J. (1997). Algorithm 778: L-BFGS-B: Fortran subroutines for large-scale bound-constrained optimization. *ACM Transactions on Mathematical Software*, 23(4):550–560.